POLITECNICO DI MILANO

Facoltà di Ingegneria Industriale

Corso di Laurea in Ingegneria Aeronautica

Numerical and Experimental Investigation of Friction Stir Welding

Supervisor :   Prof. Giuseppe Sala
Advisor: Dipl.-Ing. Bernhard Selk

Alberto Merlin   770593

Academic Year 2011-2012

To my family

Acknowledgments

First, I want to thank Prof. Giuseppe Sala, Ms. Alida Berto of Ruecker-Aerospace and Dipl.-Ing. Robert Becker of RUAG Aerospace Structures, without whom this very interesting opportunity would not have been possible.

A special thanks goes to my advisor at RUAG Dipl.-Ing. Bernhard Selk for his great mentoring throughout this whole work. I also want to express my gratitude to Dipl.-Ing. Becker for his good advices. For the very nice atmosphere at RUAG Aerospace Structures, I thank my colleagues in the engineering.

For the really good time spent together during these past years, I thank all my friends.

A special thanks goes to my housemates and very good friends Alessandro and Luigi, for their constant support and true friendship.

I would also like to express my gratitude to Beatrice for her understanding, her support and her many sacrifices during these past months.

Abstract

Aim of this work is to gain a good understanding of the *DeltaN* friction stir welding process of Al2024. Three different test campaigns were held, during which small coupon samples were joined. Temperatures were measured through the use of type K thermocouples and acting forces through load cells. Deformations were also recorded for the 1st test campaign through photogrammetry. The process was simulated with MSC Marc software. The test structure has been idealized with different contact bodies and different meshes, depending on their purpose. The analyses were thermo-structural fully coupled with non-linear material behaviour: Different stress-strain curves depending on temperature for the different microstructural zones were applied. The power input is modeled through a heat source, thus no material flow has been modeled. Process parameters and their influence on temperature distribution have been also investigated (through both experimentation and numerical simulations) and the energies involved were defined and when possible also quantified. Finally, the numerical results were correlated to experimental results.

   Key words: Friction Stir Welding; *DeltaN*; thermo-structural coupled analysis; temperature distribution; distortions; energies

Sommario

Lo scopo principale di questo lavoro è comprendere il processo di giunzione, mediante la tecnologia *DeltaN* friction stir welding. A tal fine sono state effettuate tre diverse campagne sperimentali, durante le quali sono stati giuntati provini in lega di alluminio 2024. La distribuzione di temperatura sugli stessi è stata misurata tramite termocoppie di tipo K, mentre le forze di processo agenti tramite celle di carico. Le deformazioni dei provini sono state acquisite attraverso fotogrammetria, nella prima campagna sperimentale. Il processo è stato simulato utilizzando il software MSC Marc, per correlare i risultati con quelli sperimentali e comprendere i parametri e le grandezze in gioco. La struttura sperimentale è stata modellata con più corpi di contatto e diverse discretizzazioni. Sono state effettuate analisi termo-meccaniche, con comportamento non lineare del materiale. In particolare, sono state usate curve sforzi-deformazioni dipendenti dalla temperatura, a seconda delle zone microstrutturali dei provini. La potenza fornita durante il processo è stata modellata con una fonte di calore, nel modello non è dunque presente un flusso di materiale. I parametri di processo e la loro influenza sulla distribuzione di temperatura sono stati ampiamente valutati, sia dal punto di vista numerico, sia sperimentale. L'energia richiesta ed i suoi diversi flussi sono stati individuati e, ove possibile, quantificati. Infine i risultati numerici sono stati correlati a quelli sperimentali, tramite un'opportuna scelta dei parametri investigati.

Parole chiave: Friction Stir Welding; Friction Stir Welding; *DeltaN*; analisi termomeccanica; distribuzione di temperatura; deformazioni; energie di processo

Contents

List of Tables

List of Figures

Foreword

This thesis is part of a much bigger research and development project, founded by a pool of businesses, universities and the German Ministery of Economy and Technology (BMWi, Bundesministerium für Wirtschaft und Technologie). The project is named LuFo (Deutsches Luftfahrtforschungsprogramm) which stands for German Aeronautical Research Program. It is aimed at optimizing costs and weight in fuselage structures through the deployment of new materials and new joining processes such as friction stir welding and laser beam welding, along with the creation of new production processes, new automation concepts, quality assurance, and assembly concepts as well as a cost analysis.

RUAG Aerospace Structures took part in the LuFo IV program with its project called ASSYMET(assembly of metallic fuselages) with the aim to reduce weight, costs and time in assembly of metallic fuselages. The goal is to substitute, in a near future, riveted longitudinal joints and window frame joints with friction stir welded joints.

In September 2012, ASSYMET ended and the NEWTECH project started, also in scope of LuFo IV and BMWi. The latter aims to further develop the technological know how of ASSYMET, so that a technology readiness level of 5 or 6 (TRL5/6) is achieved by the beginning of 2015.

Many studies concerning friction stir welding have been done in these projects. A crucial aspect of this application is the quality assurance, which currently is under investigation by RUAG's quality department as well as by external institutions such as the Technical University of Munich (TUM).

A technological feasibility study is also ongoing, looking for a robot suitable for this work and the fixture needed for the welding process. The latter is a big challenge, due to the huge forces required for welding simple coupons, which can absolutely not be applied to larger structures if cost efficiency and ease of production are considered. This risks making all efforts to date irrelevant, if required clamping forces can not be reduced.

The first applications of FSW joints produced by RUAG were made for two demonstrators: figure 0.1 represents a simple scaled fuselage, made of 4 shells jointed through longitudinal welds. Figure 0.2 instead is a demonstrator of a A320's section 15 fuselage part, in which friction stir welds were used on window frames and panel-to-panel joints.
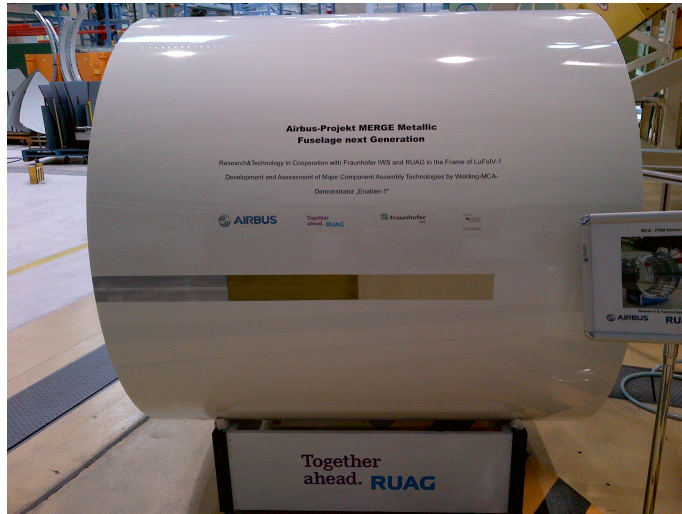
Figure 0.1: Fuselage demonstrator at RUAG's facility in Oberpfaffenhofen (D)
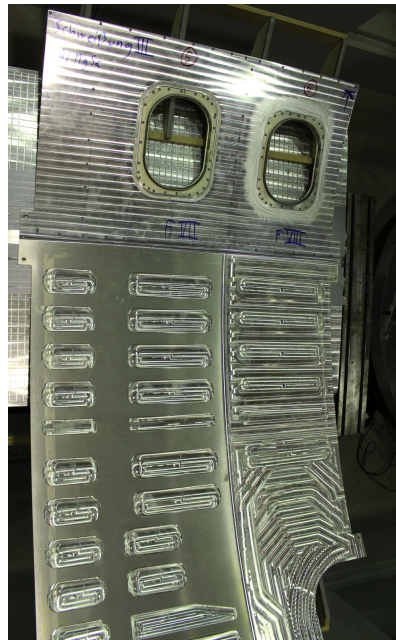
Figure 0.2: Section 15 FSW-Demonstrator: window frames and panel-to-panel friction stir welded joints. Weight reduction pockets are present. Scale 1:1

The first application of friction stir welded joints, produced by RUAG, is expected to be in the non-pressurized section 19.1, of the A320 airplanes series.

Section 19.1 is the last section of the airplane, containing the auxiliary power unit (APU), as can be seen in fig. 0.3.
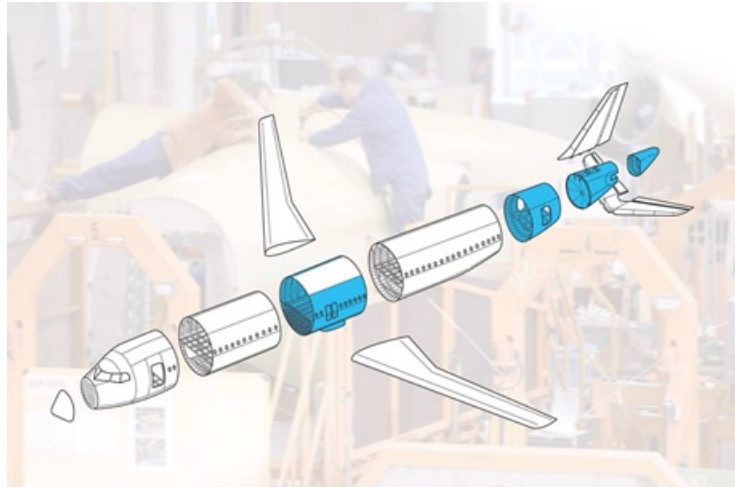
Figure 0.3: A320 sections produced by RUAG: Central fuselage (Section 15), Rear of pressurized cabin (Section 18), not-pressurized rear fuselage (Sections 19 & 19.1)

This thesis represents the work-package "Simulation of Distortions" of the project NEWTECH and is aimed at simulating the temperature distribution and the distortions due to friction stir welding of aluminum alloy 2024-T3 coupons.

1 Introduction

1.1 Friction stir welding

1.1.1 General

Friction stir welding is a solid phase welding technology, invented in 1991 by The Welding Institute (TWI) in the UK [1].

Its principle of work consists of a rotating tool that is pressed against contacting surfaces of two rigidly clamped plates[1]. Through friction between the rotating tool and the parts to be joined, heat is generated. This leads to softening of the material, which is stirred and transported from one side of the weld line to the other. Maximum recorded temperatures range between 80% and 90% of the material's solidus temperature [2, 3].

The tool is made of a probe (pin), that has different shapes and sizes, based on the materials to be joined and their thickness, that protrudes from a shoulder. A typical condition during friction stir welding, sees the workpiece placed on a rigid backing plate.

Figure 1.1: *DeltaN* generation II tool

The joining process starts by bringing the tool to the desired angular velocity and then sinking the rotating probe into the material to the desired depth, which is always slightly less than the thickness of the pieces to join, because in case of complete penetration the tool would stir into the backing plate, joining the workpiece to the backing. The shoulder typically presses against the joining

---

[1] process for butt-joints is described

line's upper surface and is inclined backwards to the welding line with an angle that varies from 2° to 4°. As the tool reaches the desired depth, and as the material begins to soften, the tool is moved forward, preferably at a constant speed. During this whole process, the shoulder must be continuously in contact with the workpiece. Heat is being created by friction between the rotating tool and the workpiece. The contact between shoulder and workpiece accounts for most of the heat generated. Actually, many investigations have been done in order to understand how much heat is generated by the shoulder and how much by the probe. Schmidt [4] found that the shoulder accounts for generating 82% of the total heat, while the probe generates the remaining 18%. Of the latter, 15% of total heat is generated by the probe-side and 3% by the probe-tip. Russell and Shercliff [5] state that the probe contributes only 3% of the total heat input, while Colegrove et al. [6] found this fraction to be 20%. It has been shown that the rotation of the pin is cause of heat as well, but to a lesser extent, while the high normal pressure and the shearing action of the shoulder account for most of the heat generation.

The generated heat softens the material in the volume around the tool, which will then be stirred by the probe. The softened material in front of the tool will be heavily deformed, transferred to the region behind it and compacted to form a joint. During the process, the shoulder constrains the material, not allowing it to escape. When the joint end point is reached, the shoulder returns perpendicular to the workpiece and retracts itself, leaving an end-hole (fig. 1.2).
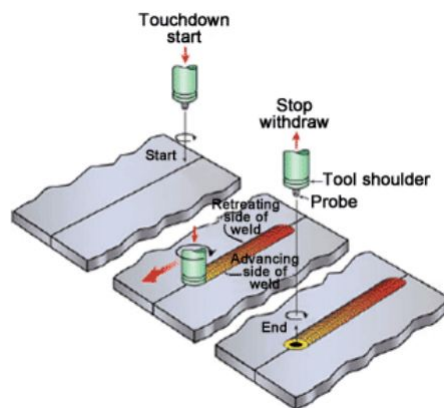
Figure 1.2: Schematic procedure of FSW process [7]

A unique feature of this process is that heat transfer not only takes place

via thermal conduction, but also via the extrusion of the workpiece's material adjacent to the tool. In general, both the heat and the mass transfers depend on material properties, tool geometry and parameters of the process.

Friction stir welding can be thought of as a process of constrained extrusion under the action of the tool [7] and its peculiarity is that it allows joining difficult-to-weld materials such as 2xxx, 7xxx and 8xxx aluminium alloys, as well as dissimilar alloys [8, 9]. For this reason, as well as the very good joint line characteristics (very high joint efficiencies in terms of ultimate static strength compared to the base material) commercial application have been reported across many different industries. It has been discovered that joint efficiencies exceed 90% for 7xxx alloys [7], while efficiencies can reach up to 82% for 2017-T351 [10].

Table 1.1: Joint efficiencies, in terms of ultimate static strength, for different aluminium alloys [8]

Alloy (thickness)	Base metal UTS (MPa)	Friction stir weld UTS (MPa)	Joint efficiency (%)
AFC458-T8	544.7	362.0	66
2014-T651 (6mm)	479-483	326-338	68-70
2024-T351 (5mm)	483-493	410-434	83-90
2219-T87	475.8	310.3	65
2195-T8	593.0	406.8	69
5083-O (6-15mm)	285-298	271-344	95-119
6061-T6 (5mm)	319-324	217-252	67-79
7050-T7451 (6mm)	545-558	427-441	77-81
7075-T7351	472.3	455.1	96
7075-T651 (6.4mm)	622	468	75
6056-T78 (6mm)	332	247	74
5005-H14 (3mm)	158	118	75
7020-T6 (5mm)	385	325	84
6063-T5 (4mm)	216	155	72
2024-T3 (4mm)	478	425-441	89-90
7475-T76	505	465	92
6013-T6 (4mm)	394-398	295-322	75-81
6013-T4 (4mm)	344	323	94
2519-T87 (25.4mm)	480	379	79

1.1.2 Existing Applications

As reported by TWI [7], 200 licenses for the use of friction stir welding have been issued from 1991 until the end of 2007, more than 1900 patent applications have been filed relating to FSW, and these numbers are expected to rise substantially

due to the growing interest in this joining technology by manufacture industries.

In general, FSW is particularly indicated for aluminium components and for other difficult-to-weld metals. Because of the very little change in material properties, FSW is often used on large pieces which cannot be easily heat treated after welding to recover their temper characteristics.

A few of the most significant examples of applications will be presented [7]. Due to the continuous development of friction stir welding and its expanding applications, it is not possible to present all of them.

Use of this technology in the marine industry, for example, has been used to join 6xxx series alloy extrusions for production of fish freezing plants for fishing vessels, for incorporations in bulkheads and decks for aluminium high speed vessels, as well as for large cruise ships, which started adopting lightweight aluminium structures. Extensive use of friction stir welding for aluminium superstructures was made in the construction of the ' Seven Seas Navigator' and the Japanese fast ferry 'Ogasawara'.

In the space industry, the most popular applications are in joints of the Detla IV rockets and Space Shuttle fuel tanks.

In the aeronautical industry, all major airframe manufacturers are currently investigating and evaluating friction stir welding to replace riveted joints. A good example of the use of FSW in aircraft manufacturing is the Eclipse 500 business jet. It makes extensive use of FSW for its longitudinal fuselage joints. In fact, more than 7300 fasteners have been replaced by FSW welds, with a significant reduction in manufacturing costs and weight of the structure [11].

Other applications of FSW are present in the rail industry in the production of the Shinkansen, the Japanese high speed train, and in the automotive industry for various parts.

In airframe manufacturing, it has been estimated that this welding process, allows savings of up to 20% of weight and 30% of cost, compared to the traditional rivet joining technique [12]. ([13] states 15% of weight and 20% of costs). For window frame reinforcements 10% in weight and 30% in costs was saved due to butt, instead of lap-joints, and shorter manufacturing time [14]. To give the reader a better idea, for a single Ecplise 500 Business Jet more than $200,000 has been saved during production of the fuselage.

Pacchione et al. [15] calculated that on A350 XWB fuselages considerable weight can be saved by applying FSW joining techniques. For example, on a stringer-to-panel joint, $0.18 \frac{kg}{m}$ can be saved, while on panel-to-panel joints up to 0.8 kg per meter of weld can be saved. Considering all the joints on a fuselage of

the A350, it is immediately understandable how important this new technology could become.

For these reasons, RUAG, together with Airbus and its strategic partners, considers replacing the riveted longitudinal joints of the A320 series planes with longitudinal friction stir welded joints. In fig. 0.1 the demonstrator created by RUAG in collaboration with Airbus and the Fraunhofer Institute is shown. A detailed image of the end hole is displayed in figure 1.3. It should be noted that in the final demonstrator, the initially extruding part, containing the end-hole has been cut, thus avoiding all end-hole problems.
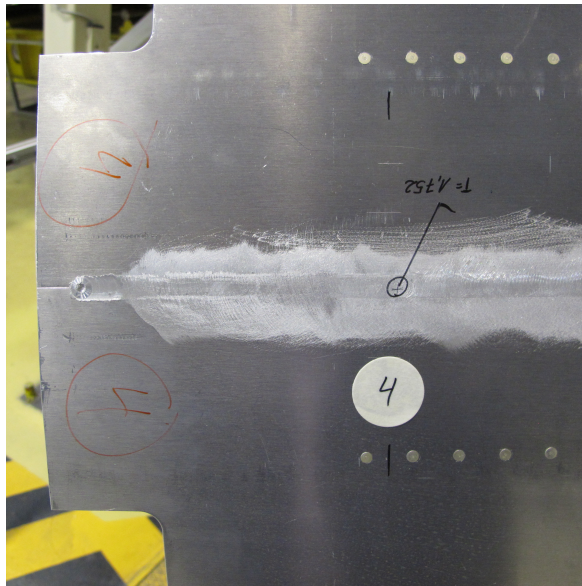
Figure 1.3: Detail of the end hole of the fuselage's demonstrator. The part with the end hole will be cut. The weld line has been treated to obtain a better final surface finishment

1.1.3 Process Parameters

The main FSW process parameters that affect both weld quality and process efficiency are:

- rotational and transverse velocity of the tool;

- down force;

- tool plunge depth

- pin's penetration depth

- tool tilt angle;

- tool design and material.

- clamping forces

In general rotational and transverse velocity influence the temperature field and a delicate balance of these two quantities is needed. Many tests and investigations have been performed in order to define optimal parameter windows for the different materials and thicknesses.

Tool plunge depth, defined as the depth of the shoulder's lowest point below the surface of the welded plate, has to be set correctly. Typically, insufficient plunge depth results in low quality welds, due to inadequate forging of the material at the rear of the tool, while excessive tool plunge depth leads to undermatching of the weld thickness compared to the base material thickness.

Tool tilting rearward by 2°-4° has been found to be beneficial since it enhances the effect of the forging process.

The tool's design, comprised of both probe and shoulder, is very important for this process and many resources have been committed to research it. Since the pin directly influences the material flow, its design is of fundamental importance and depends on the workpiece material and its thickness. Typically, probes contain threads or helical flutes to force the material adjacent to the pin to flow away. In addition to probe design, many different shoulders have been created for various applications. Tool design has extensively researched by Fuller [16] and by Dubourg et al. [17].

1.1.4   Asymmetry of Weld and Welding Zones

Taking a closer look at the FSW process, an asymmetry in heat transfer, material flow and weld microstructures properties can be seen. This is basically due to the rotation of the tool itself: the velocity of the tool, in different points at its surfaces, has very different orientations, depending on the position considered. The side on which the circumferential velocity of the rotating tool is oriented as the transverse velocity, is defined as the advancing side of the weld, while the tool's opposite side is defined as the retreating side of the weld, because the

circumferential velocity is contrary to the translational movement of the tool. This characteristic behaviour gives rise to the asymmetry of the process.

As pointed out in the introduction, friction stir welding is a very complex process, which involves thermo-mechanical processes such as friction-energy dissipation, plastic deformation and the associated heat dissipation, material transport and flow, dynamic recrystallization, local cooling etc. [7].

A metallographic examination of the FSW joints typically reveals the existence of different welding zones. A first attempt at classifying the microstructures in Friction Stir Welding was made by Threadgrill [18]. His work primarily dealt with aluminium alloys. Subsequently, many investigations on the microstructure of friction stir welded materials followed until the definitions presented here were commonly accepted and adopted by the American Welding Society Standard D17.3M:

- the unaffected zone (or parent material): it is enough far away from the weld so that material micro-structural and mechanical properties are not altered by the joining process, although it may have been exposed to a thermal cycle from the welding process. The micro-structure and properties remain those of the initial parent material.

- preferably heat affected zone (HAZ) or thermally affected zone (TAZ): micro-structural and material properties are influenced only by thermal effects present in the FSW process. It is closer to the weld line, but no apparent plastic deformation occurred. Changes in micro-structure depend primarily on the type of alloy considered: work hardened alloys, suffer from recovery of dislocation networks, causing a low angle cell boundaries to form. Precipitation hardened alloys instead suffer from coarsening of precipitates and possible dissolution at higher temperatures.

- the thermo-mechanically affected zone (TMAZ) which is subdivided in the deformed TMAZ and the dynamically recrystallized TMAZ. In the deformed zone both material micro-structure and properties are affected by thermal and mechanical aspects of FSW. Typically the original grains, although they have been severely deformed, are retained in this zone. The micro-structure is given by deformed sub-grains, divided by low angle grain boundaries. The dynamically recrystallized zone is commonly known as "nugget zone" or "weld nugget": it is the innermost zone of a FSW joint. This region contains the so-called onion ring feature, due to the stirring

of material from in front of the tool to its back. The material constituting the nugget has undergone the most severe plastic deformation and has been exposed to the highest temperatures of the process. Consequently, the nugget contains a very fine dynamically recrystallized and equiaxed grain micro-structure. As stated in [7] it is most likely that before recrystallization, an extensive recovery of dislocations occurs.

(a) Changed Micro-structural Zones   (b) Detail [7]
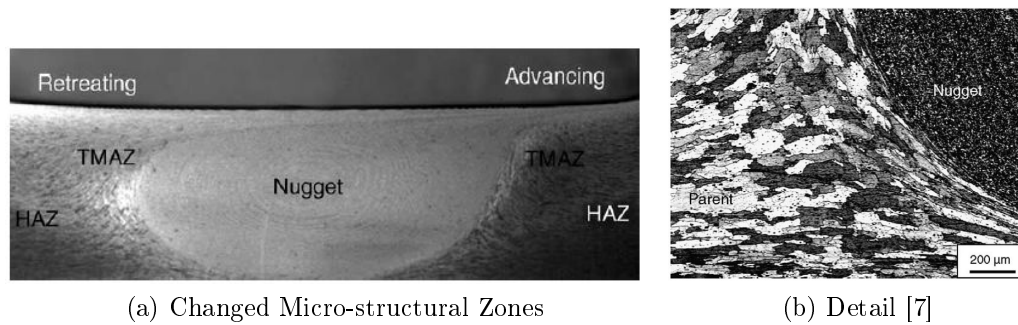
Figure 1.4: FSW Micro-structures of Al7075 [8]
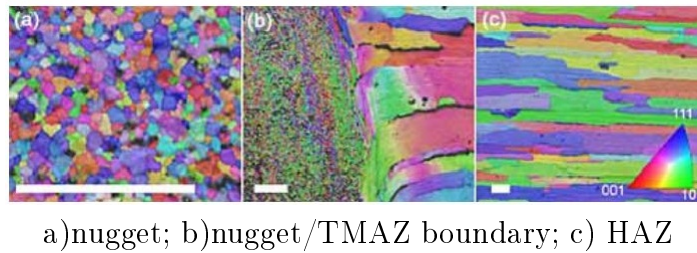
a)nugget; b)nugget/TMAZ boundary; c) HAZ

Figure 1.5: Micro-structure of 2199 alloy (The scale bar corresponds to $50\mu m$) [7]

1.1.5 Advantages and Disadvantages of FSW

In comparison to traditional fusion welding techniques, FSW offers a number of different advantages, as well as some disadvantages.

Major advantages are:

- good mechanical property in the as-welded condition.

- improved safety due to the absence of toxic fumes or the spatter of molten material.

- no requirements for consumables such as a filler material or gas shield.

- ease of process automation.

- ability to operate in all positions (horizontal,vertical, overhead, orbital, etc.) as there is no weld pool.

- minimal thickness under/overmatching, which reduces the need for expensive post-weld machining.

- low environmental impact

However, some major disadvantages of this technological process are:

- an exit hole is left after the tool is withdrawn from the workpiece.

- relatively large tool press-down and plate-clamping forces are required.

- lower-flexibility of the process with respect to variable-thickness and non-linear welds.

- often lower welding rates than conventional fusion-welding techniques, although this shortcoming is somewhat reduced since fewer welding passes are required.

- the, already cited, asymmetry of the weld.

- Root and surface flaws, tunnel and lack of penetration

1.1.6 Heat Generation

The distinctive characteristic of friction stir welding is that this process makes no use of external heat sources. The heat is generated during and throughout the process itself. Therefore the process parameters and the tool's shape are of fundamental importance.

1.1.7 Flaws in Friction Stir Welding

During all material working processes flaws can arise. The definition of flaws and defects provided by [7] is accepted: "The usual distinction is that a flaw or imperfection is a feature that one would prefer not to be in the weld, but it may or may not compromise the integrity of the weld. If after evaluation, the flaw is deemed unacceptable, then it becomes a defect. If it does not compromise the integrity, then it is a tolerable flaw."
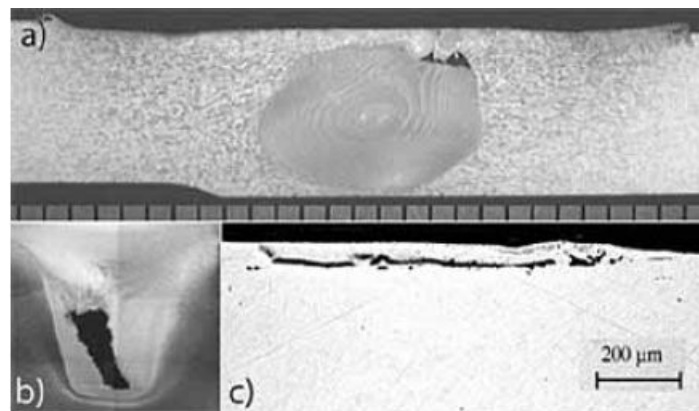
Figure 1.6: Typical flaws in friction stir welds: a) volumetric flaw in Al2014; b) tunnel (wormhole) in Al7449; c) surface defect located under shoulder in 2014 aluminium alloy [7]

Flaws in friction stir welding have been thoroughly investigated and understood. Typical flaws in friction stir welding are voids, worm holes, tunnels, root and surface flaws. Many of these have been avoided or significantly reduced by changing tool and welding parameters. For example, to eliminate forming of tunnels, a tool tilt angle has been introduced or a new design of the tool has been chosen, while for void formations, parameters like welding speed, both

rotational as well as traverse, pressure and control of the joint gap have been found to be of primary importance.

Joint line features, like oxide particles, are always present in FSW joints, but they constitute no problem, if good stirring occurs. Other flaws like "kissing bonds" (lack of continuity of the bond between the material from each side of the weld resulting in a light contact of the parts) and lack of penetration, caused by insufficient pin's penetration depth, are very rare and can be avoided by selecting the right tool and joining parameters. Finally the creation of flash is caused by excessive tool plunge depth and can also be easily solved by setting the correct parameters, i.e. the downward force. In general, this can be post-treated with a surface treatment.

Flaws in FSW are, in general, quite different from the ones present in standard welding processes. Typically, friction stir welds do not present a high number of flaws and, if not absolutely necessary, not all welds do undergo complete nondestructive inspection. Since traditional nondestructive inspection techniques have been developed for standard welding, they do not work well with FSW, but the continuously growing application of FSW demands new tools for investigating flaws.[7]
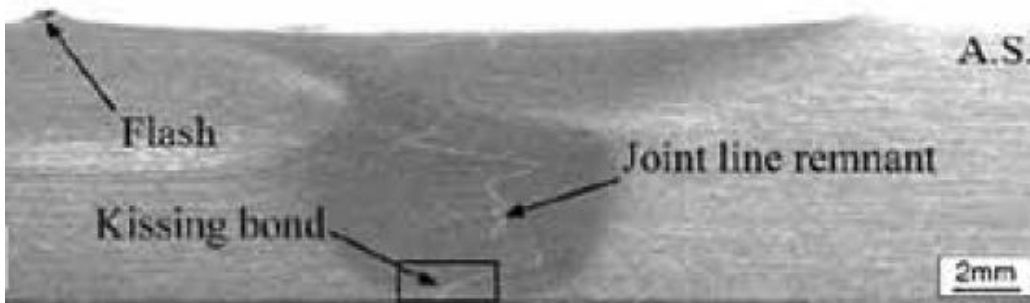
Figure 1.7: Detail of common flaws and defects

By defining "optimal" process parameter windows, the creation of flaws has been considerably reduced.
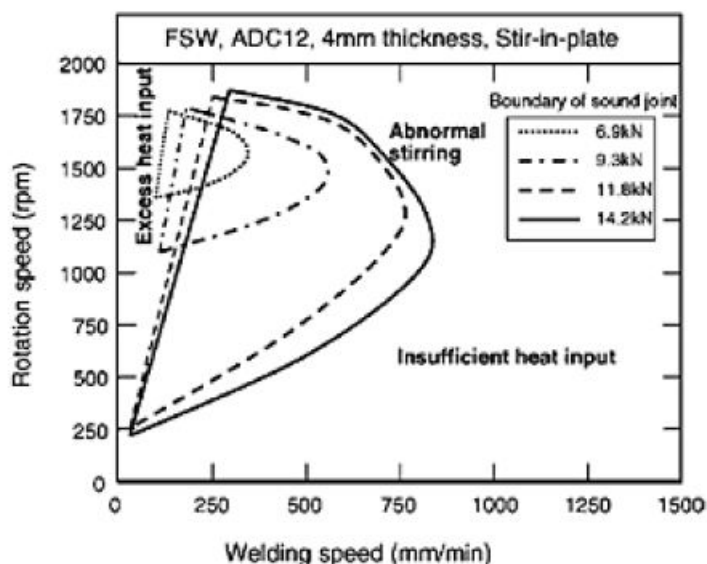
Figure 1.8: Range of optimum FSW conditions for various down forces for 4 mm thick ADC12 Al-Si casting alloy welded using 15 mm shoulder, 5 mm diameter, 3.9 mm long threaded pin [7]

1.1.8 Residual Stresses

In friction stir welding, residual stresses arise from the accumulation of misfits between the weld region and the remaining plate, particularly during cooling of the workpiece. Different techniques to reduce residual stresses exist (thermal tensioning, mechanical tensioning and/or subsequent processing treatments [7]). Nevertheless residual stresses are always present in as-welded components.

The very rigid clamping of the plates doesn't allow the weld zone to contract itself after the welding process, thus causing both longitudinal and transverse stresses. The presence of high residual stresses in the welded workpiece causes a considerable effect on the workpiece's mechanical properties, with an important influence on fatigue behaviour of the workpiece. This leads to the necessity of studying residual stresses in friction stir welded plates.

Dalle Donne et al. [19] measured residual stresses for Al2024-T3 plates through different methods: cut compliance technique, X-ray diffraction, neutron diffraction and high-energy synchrotron radiation. They measured that longitudinal (parallel to welding direction) residual stresses are between 40 and 60 MPa, while traverse stresses (normal to the welding direction) reach values

of 20-40 MPa. With these results it was possible to state that longitudinal residual stresses are higher than traverse stresses. Another important finding is that if residual stresses are plotted across the weld, both longitudinal and traverse present an "M-like" trend (fig. 1.9). Highest longitudinal stresses are reported towards the end of the weld and peak values for longitudinal stresses were measured at a distance of about 10mm from the weldline, which coincides with the HAZ. Residual stresses across the weld were reported to be similar at the top and bottom sides. Maximum longitudinal stresses were reported to be in between 20% and 50% of the base material's yield stress [19].
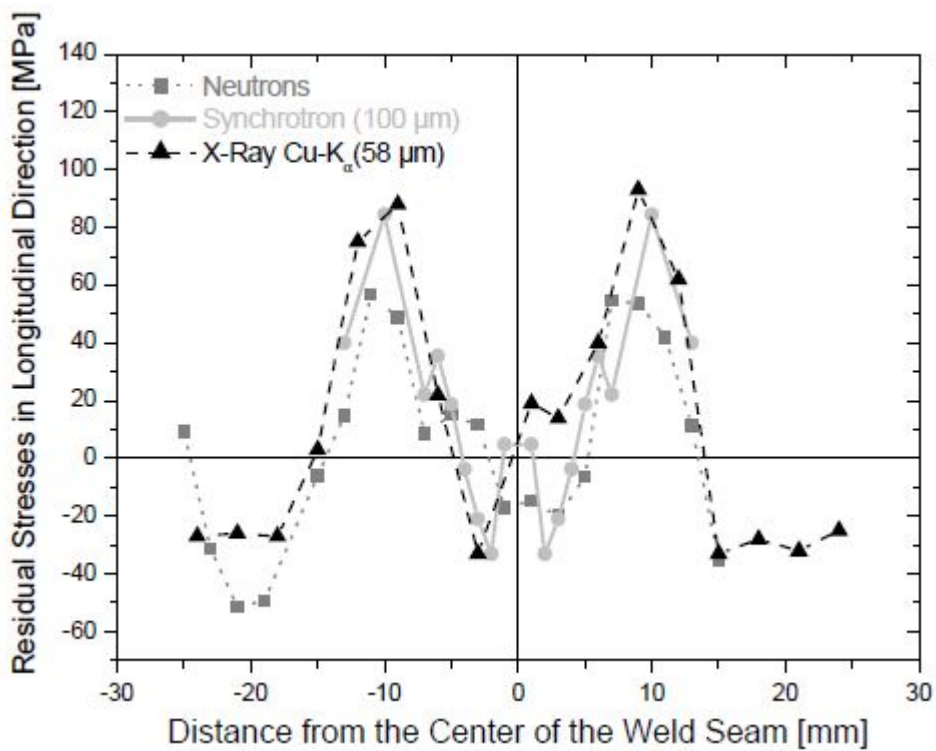
Figure 1.9: Typical trend of residual stresses for friction stir welded plates. Residual stresses were measured with 3 different methods for a 6013-T4 sheet [19]

Mahoney et al [20] found that residual stresses are much higher at the transition between the fully recrystallized and partially recrystallized regions. Looking at fig. 1.9, it can be noticed that residual stresses in the nugget and parent material are compressive, while those in the HAZ are tensile stresses. Residual

16

stresses need to be in equilibrium, therefore tension and compression need to equilibrate themselves.

It has been clearly shown that residual stresses in friction stir welded plates are significantly lower than the base material's yield stress and lower than those in fusion welding, which usually approach the yield stress of the material. This is primarily due to the reduced heat input of FSW, compared to conventional fusion welding.

These outcomes clearly lead to less distortion of FSW components and better fatigue properties.

1.1.9 Distortions

In general, FSW of aluminium leads to low distortions compared to other fusion welding techniques such as arc welding. However, significant distortion can occur in thin friction stir welded plates, where the design imparts an asymmetry in restraints or heat sink.

It has been found that previously mentioned techniques, like mechanical and thermal tensioning, used to lower residual stresses, are also effective for lowering of distortions.

1.1.10 Fatigue

It is usually accepted that all welded structures go into service with flaws ranging from volume defects like porosity, and non-metallic inclusions to different planar defects like cracks induced by hydrogen or hot tearing [8]. There are standards for acceptability of the welds pertaining to different inspection codes. The non-acceptable flaws, namely the defects, must be repaired before the welded component is put into service. Most existing codes cater toward weldments made by conventional welding techniques. FSW is generally found to produce defect-free welds. However, no established code exists so far for FSW.

It should be pointed out that no detailed microstructure property correlation has been established so far for the fracture toughness of FSW welds. Since microstructures are changed significantly during FSW, it is important to understand the influence of microstructural characteristics on the fracture toughness of friction stir welds.

1.2   Static Shoulder Friction Stir Welding

Static shoulder FSW is a particular version of friction stir welding. It is also called *DeltaN* (or Δn) friction stir welding by EADS and their partners. *DeltaN* stands for the difference in terms of rotational velocity between probe and shoulder. Since this is a static shoulder welding process, the shoulder has only traverse speed and n represents the probe's rotational speed.

The main difference between standard friction stir welding and *DeltaN* FSW is in the heat generation: in *DeltaN* friction stir welding, almost no heat is created by the shoulder; the only heat source is the friction on the probe-workpiece interface.

Temperatures required for softening of the material during the welding process are the same, thus making it indispensable to define a new combination of traverse and rotational velocities. The use of *DeltaN* tool requires raising the probe's rotational speed.

Advantages of *DeltaN* technology, compared to conventional FSW, are many: for example, using the same probe, all 4 macroscopic welding zones are much smaller and the heating through thickness is much more uniform. Also the microstructural properties and residual stress distribution are much more symmetrical for the *DeltaN* tool, because there is not such a big difference in heat generation between the advancing and retreating side. The *DeltaN* tool generates a consistent linear heat input throughout the weld cross-section. This is particularly indicated for welding of low conductivity materials and leads to better weld quality and ease of weld production [21]. A significant difference in surface refinement on both top and bottom surfaces can be also noticed; the *DeltaN* tool leaves a much smoother surface, because weld flash is no longer created during the welding process, thus requiring less post-weld treatments and reducing time and cost of good quality welds. Another very important factor is that a joint efficiency of nearly 100% can be obtained [21]. In *DeltaN* FSW the effect of the shoulder is limited to a very thin surface layer.

A comparison between the conventional FSW process and the *DeltaN* process shows that *DeltaN*-FSW seems to be better than the conventional technology.

In reference to [12], for an AlMg5 alloy cast of 15mm thickness, the following comparison between conventional FSW and *DeltaN* tool can be displayed:

Table 1.2: comparison between conventional FSW and *DeltaN* tool

parameter	FSW	*DeltaN* tool
n (rpm)	250	500
v (mm/min)	80	80
F(kN)	24	15

The provided data shows that the theoretical potentials of the *DeltaN* tool concept are confirmed [12]:

- reduction of the welding distortion by factor of 8

- reduction in vertical down-force by factor 2

- simple (Δn gen.4) and therefore robust design

Another important aspect of static shoulder FSW is that higher rotational velocity, on the same feed velocities, leads to longer lifetime of the pin, thus reducing costs and making the process more reliable, because the tool is less likely to break during welding. This reduces "quality" issues and leads again to a more reliable process and significant cost and time reduction.
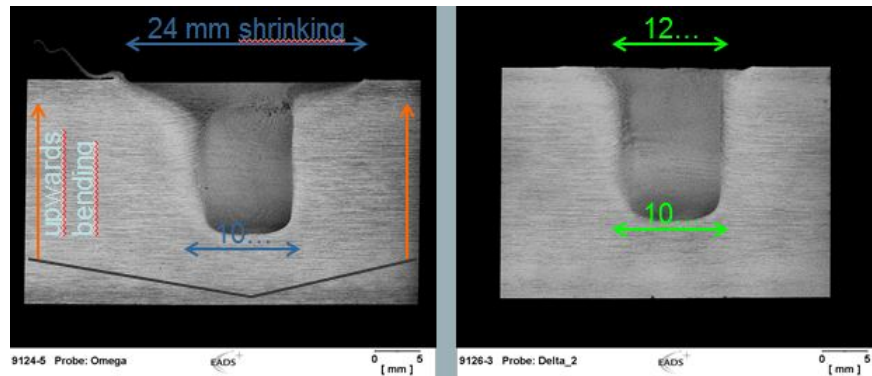
Figure 1.10: Comparison between weld zones of conventional Vs. DeltaN gen II tool

As described by Widener [22], a quenching effect of the fixed shoulder could be enhanced by the addition of a cooling lines tool to maintain a large temperature differential. Since it is well known that 2024 and 7075 alloys are very

quench-rate sensitive, with higher strengths for higher quench rates, this inno-
vation may provide a new way to enhance the mechanical properties of friction
stir welds in 2xxx and 7xxx alloys. This tool could appreciably improve the
fatigue life of the as-welded material, since the stress concentrations of the weld
track could be eliminated by the use of a fixed shoulder. A detailed description
of results, in terms of surface quality and microstructure, for SS-FSW at low
and high rotational speeds can be found in his work.

DeltaN tools have undergone an evolutionary process, as did conventional
FSW tools. The generation I tools were just like conventional FSW tools, but
they've been developed to optimize the welding process, until reaching genera-
tion IV design.

Figure 1.11: *DeltaN* generation IV tool used during the testing campaigns

1.3 Self Reacting Tool

The self reacting tool (or bobbin tool) is especially designed to avoid root flaws
caused primarily by single-sided tools [23]. It has two shoulders and brings some
benefits compared to the standard FSW tool. Some of these are the absence
of weld roots or root defects and low downward forces which lead to significant
cost reduction in machine and fixture. Obviously, no backing plate is required.
Bobbin friction stir welding (BFSW) tool leads to low distortion of the workpiece
due to uniform heating. It is also simple to control and very tolerant of thickness
variation.

The major problem is that with this tool no closed weld path can be done.
Bobbin FSW requires open start and open ending positions, thus making it
impossible to use for welding of window-frames.
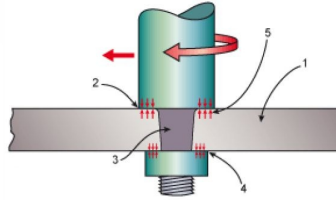
Figure 1.12: Bobbin Friction Stir Welding (BFSW) tool [23] 1 workpiece, 2 top shoulder, 3 probe(pin), 4 bottom shoulder, 5 reactive forces

1.4 Comparison of FSW with other Joining Techniques: Rivets & Glue

Friction Stir Welding requires a certain amount of heat input, thus causing distortions in the original workpiece. As already shown, this is the major disadvantage of this relatively new joining technique compared to riveting or gluing. In order to respect tolerances during production, a very good understanding of this process is required.

New techniques of non-destructive controlling and testing will be needed. Also fatigue behaviour such as crack initiation and growth need to be further investigated. Crack stopping techniques need to be thought of and developed for FSW joints. In riveted joints, the joint itself acts as a crack stopper. Of course, in FSW this characteristic is not present.

In FSW there is no need for overlapping joints, due to the butt-joining, nor for rivets. This allows to save the weight of the overlapped parts and the rivets, resulting in considerable weight reduction. In addition, the tensile strength of friction stir welded joints is higher than that of rivetted joints.

For glued joints, the overlap needs to be at least equal, or even bigger, than for riveting, because larger areas are needed to glue the parts together. The total weight would increase. Special surface treatments are also required, raising both production time and costs.

FSW joints can be considered as a valid alternative to the standard rivet joining technique, with major savings in weight and production costs, as previously reported, and without reduction of joint quality characteristics. Therefore FSW is currently being investigated for different applications in aeronautical structures.

2 Experimentation

2.1 First Campaign (September 2012)

During the first test campaign, held in mid september 2012 at EADS Innovation Works in Ottobrunn, Munich, many different tests were performed, with the goal to investigate all quantities associated with the fixture, as well as process parameters. For some tests temperature measurements were performed, to gain a first experience with thermocouples and to gain an idea of temperature distribution in the workpiece. Both thermocouples, and infrared camera were used to record temperatures. However, the infrared camera did not return good results, due to the high reflection on the shoulder. Measurements of distortions were also performed through photogrammetry. A short overview of the performed tests is available in the appendix in tab. 5.2.

Results of traction, as well as bending tests after AITM1-0064 standard, are also reported in the appendix.

Clamping Pressure

During this first testing campaign, pressure exerted by the clamps has been evaluated through the use of pressure measurement films placed between the clamping fixture and the workpiece. Through the changing of colour and a careful evaluation (considering both temperature and humidity), the correlation between tightening torque and applied pressure was found (tab. 2.1).

Table 2.1: Correlation between tightening torque applied to screws and clamping pressure on the workpiece [24]

Tightening torque [Nm]	p [MPa]
30	4.17
25	3.47
20	2.78
15	2.08

2.2 Testing Devices

2.2.1 Thermocouples Selection

Thermocouples are devices for temperature measurements [25, 26]. They are made of two different metal wires, called thermoelements. These thermoelements are joined together to form two junctions. One is connected to the body on which the temperature is to be measured (hot or measuring junction), while the other junction is connected to a body of known temperature (cold or reference junction). Whenever a difference in temperature between the two junctions exists, a difference in voltage is produced between the wires (Peltier effect). This difference is then measured at the reference end of the thermoelements and provides the information required to calculate the temperature at the measuring end. Thus, the thermocouple enables measuring the unknown temperature of the body with reference to the known temperature of the other body, which is in general the measuring device itself. The thermocouple is basically a temperature-voltage transducer, with the following relationship:

$$Emf = \int_{T_1}^{T_2} (S_1 - S_2)\, dT \tag{2.1}$$

where Emf stands for Electro-Motive Force or Voltage produced by the thermocouple at the tail end, T_1 and T_2 respresent the temperatures respectively at the tail and at the measuring end and S_1 and S_2 are the Seebeck coefficient of the thermoelements. This coefficient depends on the thermoelement's material and on the temperature itself.

The relationship between voltage and temperature is mostly non-linear and it can be approximated by the following polynomial:

$$\Delta T = \sum_{n=0}^{N} a_n v^n \tag{2.2}$$

where a_n represents the polynomial's coefficients and v the output voltage. Typically the coefficients a_n are given for n from 0 to between 5 and 13, depending upon the thermoelements' material. For the used thermocouples (type K) $n = 9$.

Table 2.2: Polynomial coefficients for type K. $0° - 500°C$ range [25]

n	a_n
1	25.08355
2	$7.860106 \cdot 10^{-2}$
3	$-2.503131 \cdot 10^{-1}$
4	$8.315270 \cdot 10^{-2}$
5	$-1.228034 \cdot 10^{-2}$
6	$9.804036 \cdot 10^{-4}$
7	$-4.413030 \cdot 10^{-5}$
8	$1.057734 \cdot 10^{-6}$
9	$-1.052755 \cdot 10^{-8}$

Different types of thermocouples are available on the market and its selection depends upon parameters such as melting temperature, chemical properties, stability and output, as well as other factors like cost, availability and convenience.

For the here required application, many different thermocouple types are well suited, in terms of temperature range and error. Type K thermocouples, with $0.5\,\text{mm}$ thick wires, were chosen based on the availability. Type K thermocouple is the most common general purpose thermocouple and its positive thermoelement is made of chromel (90% nichel and 10% chrome), while the negative thermoelement is made of alumel (95% nichel, 2% manganese, 2% aluminum and 1% silicon). Its sensitivity is approximately 41 $\frac{\mu V}{°C}$ and its measuring range goes from 0°C to 1100°C for continuous exposure, while for a short period it could measure between -180°C and 1300°C [25].

2.2.2   Data Acquisition

To measure the voltage at the tail end some device is needed. If a single thermocouple is employed, a standard voltmeter would be enough. Since multiple thermocouples are used and since the measurements need to be recorded, an acquisition module is necessary. For this purpose, the USB Data Acquisition Model OMB-DAQ-2416 is used. Up to 16 differential voltages can be measured with this device, which corresponds to the use of 16 thermocouples. Through a USB connection to a notebook all the data can be viewed in real time with a specific software and saved to the notebook's hard drive. In order to get reliable results, prior to any testing, the aquisition device needs to be connected to the electrical system and warm up for at least 45 minutes.

It has been noticed that the sampling frequency of this device changes with the number of channels in use: if all channels are used, the maximum sampling frequency is 3 Hz, while it could sample up to 4 Hz if the channels used are less. The sampling frequency is saved to the same file, containing the recorded results [27].

2.3 Test: How to Apply TC

Prior to further experimentation, it became necessary to acquire more experience with this temperature measuring technique. Therefore, three different application methodologies for thermocouples were tested to understand which one was best suited for the upcoming tests. Adhesion strength, detachibility and quickness of response were the criterions to choose the application method.

For the purpose of testing, two different solutions of thermocouples were used, as reported in tab. 2.3.

Table 2.3: TC solutions

	Solution A	Solution B
Type	K	K
diameter of wire	0.05 mm	0.7 mm
length	1000 mm	1000 mm
isolation	fiber glass	fiber glass
measuring end	open	screwed

Two small Al2024-T3 coupons (100 x 94 x 3 mm) were fitted with 3 thermocouples each, as displayed in fig. 2.1. The welded tip of the K1 thermocouple was brought in contact with the coupon's surface and glued via the high temperature air set cement Omegabond 400 (OB400) from Omega Engineering. The K2 thermocouple kept in place onto the surface with an M3 screw. The tip of the K3 thermocouple was bent and then inserted in a small hole (diameter of 1.5mm), previously drilled into the coupon. Again, a drop of OB400 paste has been used to fix the thermocouple. The two samples were left still for 24h to let the cement dry out completely.

The testing began with setting up a pot containing boiling water and preparing all measuring equipment (DAS and notebook).

The coupons were first partially submerged into the pot containing boiling water (about 100°C) and after a nearly steady state had been reached, they

were partially submerged into icy water (about 0°C). During both operations, attention has been paid to avoid contact between water and the thermocouples' wires.

The obtained trends are shown in fig. 2.3. Looking at the figure, it is clear that the glued and the "drilled" thermocouple had almost the same temperatures over time, while the heating and cooling curve of the screwed thermocouple is quite different, due to a slower response. All three thermocouples reach approximately the same temperature over time, but since the temperature measurement during friction stir welding will be a fast and transient process, the screwed thermocouple application method is excluded.

After a careful evaluation of the best contacting properties, the drilled application method has been chosen. In fact, besides presenting better resistance to torque and traction, it also interferes less with the shoulder close to the welding line.

During testing, the advantage of the drilled solution became quite clear: less thermocouples were detached during transporting and clamping, and thermocouples close to the welding line interfered less with the passing-by tool's shoulder, resulting in less detached thermocouples than in the first tests.
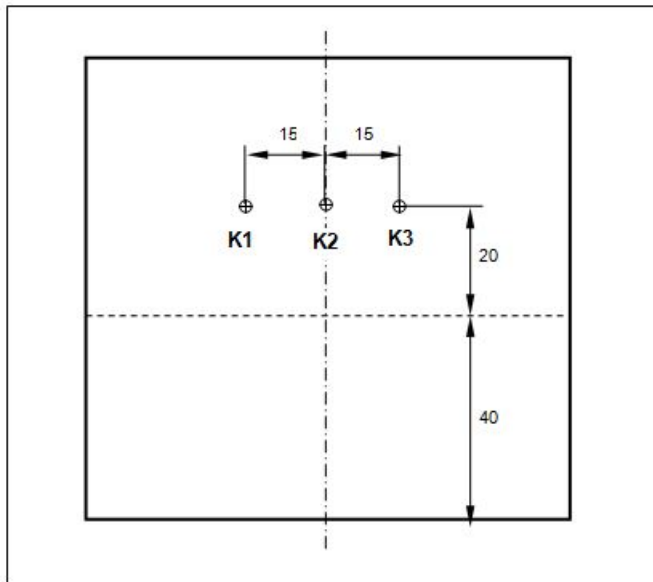
Figure 2.1: Disposition of thermocouples: K1 = glued on surface; K2 = screwed; K3 = glued in previously drilled hole

(a)   (b) Detail
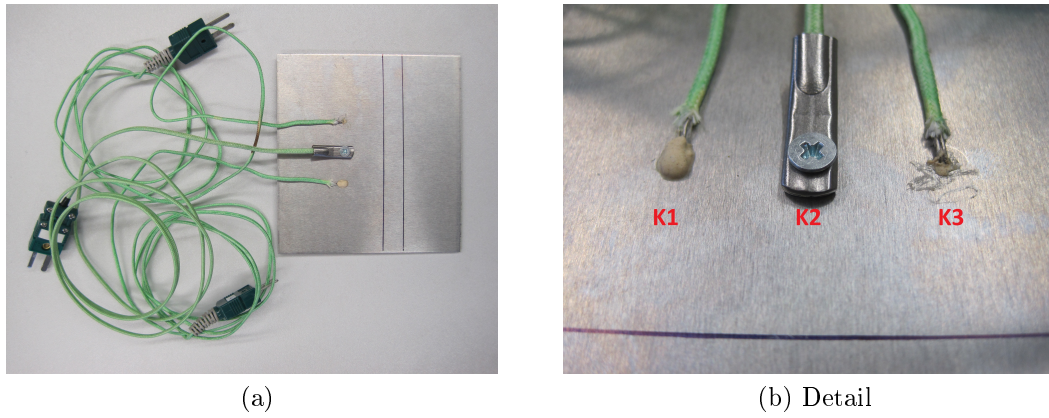
Figure 2.2: Thermocouple test setup
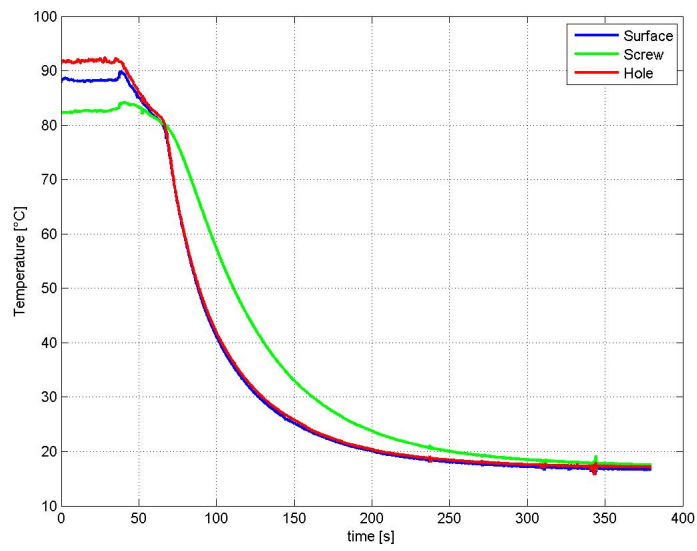
Figure 2.3: Comparison between Thermocouple application methods

2.4   Second Campaign (November 2012)

The second test campaign, held in mid November 2012, proved to be very valuable for this work and led to the arise of important questions. All tests were performed at EADS Innovation Works *DeltaN*-Friction Stir Welding Laboratory in Ottobrunn, Munich.

For these tests, the starting parameters were taken from the previous investigation. The values are reported in tab. 2.4:

Table 2.4: "Optimal" parameters for welding

Parameter	Value
diameter of shoulder	12 mm
angle of shoulder	2°
Diameter of probe	5 mm
probe length	3.4 mm
protrusion of probe	2.9 mm
forward speed	200 $\frac{mm}{min}$
rotational speed	1200 rpm
axial force applied	6000 N
gap between coupon halves	0.2 mm

The main scope of this campaign, was to obtain the temperature distribution for different positions during the welding process, as well as to investigate a possible reduction of clamping forces and the welding parameters, such as a reduction in axial force and the changing of traverse and rotational velocities. For a better overview of the performed tests and the parameters changed see tab. 5.3 in Appendix.

All coupons used, consisted of two rectangular $50 \cdot 100$ mm^2 Al2024-T3, 3 mm thick sheets, which were butt-jointed along their longest side.

The force controlled robot used for the welding process is the KUKA 500MT (fig. 2.4), instrumented with a 15 mm diameter generation IV *DeltaN* shoulder and a threaded probe of 5 mm in diameter.
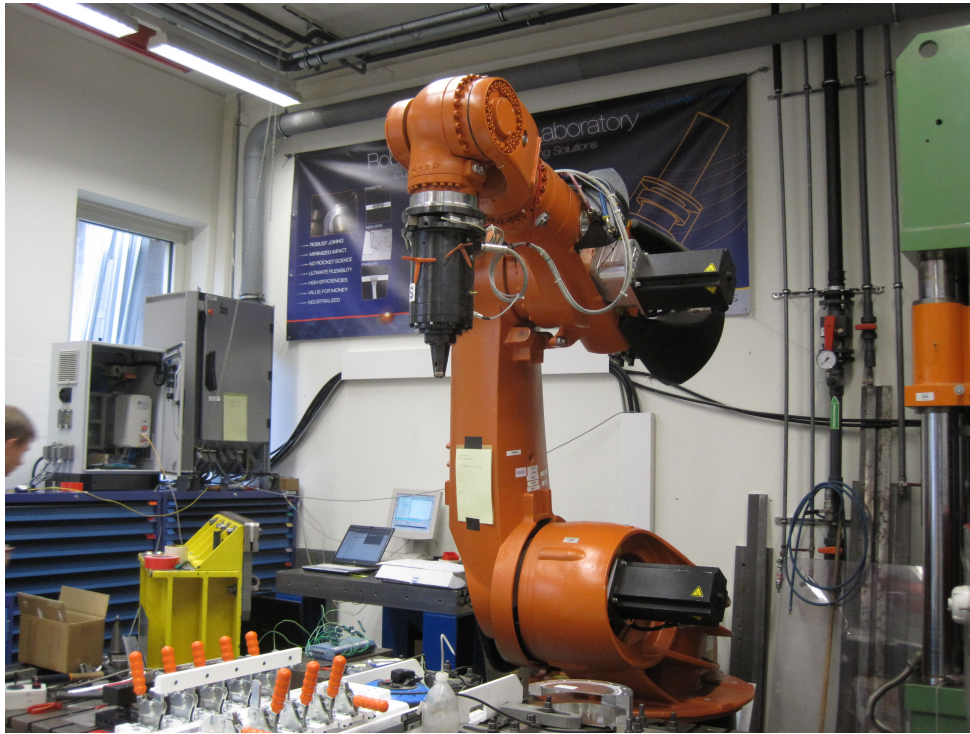
Figure 2.4: Force controlled robot K500MT used for testing at the *DeltaN*-FSW Laboratory in Ottobrunn

During the 1st and 2nd testing campaigns, both performed at EADS Innovation Works in Ottobrunn, Munich, the backing plate was provided by the *DeltaN* Laboratory, where tests were conducted. This backing plate consisted of a 42 mm thick S235 steel plate, with a width of 260 mm and length of 620 mm. It was provided with M30 screw holes for positioning of the fixture bars, on both sides, parallel to the weld line. The backing plate was then placed on a clamping table and fixed to it. Once this has been done, the workpiece made of two separate aluminium plates and eventually the small "interstitial" plate were placed on top of the steel backing. Later, one steel distanciation piece was layed on top of each workpiece half, on a previously chosen and marked distance from the weldline. Subsequently, the two workpiece halves were placed in the correct position with a gap of ideally 0.2 mm. In order to reproduce this small gap, two 0.2 mm thin lamellae were placed between the two halves and removed after clamping.

A steel bar, with 2 external M30 screw holes and 9 internal M12 screw holes,

was layed on top of every distanciation piece and fixed to the backing plate via the two M30 screws. Due to the difference in length between the bars and the workpiece, only 7 screws were used to apply the desired downward force on the distanciation piece. The tightening torque was set through a torque wrench. All this setup, was very time-consuming and brought to the extension of the testing campaign to a third day.

The testing began with the set-up of the correct weld path for the robot, followed by 3 coupon samples aimed at the reduction of clamping forces: The torque on the screws was lowered from the initial 30 Nm to 10 Nm, than 5 Nm and finally 2.5 Nm. For the latter, the weld surface was clearly not good. This brought to the interruption of the investigation and to the decision to maintain 5 Nm of torque for each screw as the lower limit for clamping forces.

Three more welds followed, with the intent to lower the axial downward force provided by the robot. The usually used force of 6 kN was lowered to 5 kN for the first weld, than to 4 kN. This resulted in a bad weld. The last weld in this test was performed again with 4 kN of axial force, but this time with no gap between the plates to joint. Again, no good weld was obtained and the tests aborted.

Another important aspect of this test campaign was to try to reduce clamping forces through the employment of FRIMA F4039 friction material, placed between the work piece and the steel backing plate. Of course, a not yet defined optimal parameter window needed to be found. After the bad experiences (plastification due to heat and mechanical load led to the release of toxic fumes) during the first test campaign, the idea to place a Ti-6Al-4V strip came up, as can be seen in fig. 2.5. This allowed to weld upon the friction material, maintaining a good weld quality and without generating too many toxic fumes, even if a slight odor was still perceptible. The FRIMA insert also has the task to isolate thermally the workpiece from the steel backing plate. In fact, the 3 performed welds seemed to be good, even with a significantly lower power input. The optimal rotational velocity of 1200rpm for Ti-6Al-4V backing was reduced to 800rpm for the 1st weld with friction material, then to 600 and finally raised to 700. The traverse speed was always kept constant at 200 $\frac{mm}{min}$.

Further investigation reguarded the reduction of clamping forces until the workpiece slided laterally during the welding process. This has been done with the friction material as backing insert. The first two tests were performed with the tool's rotational speed set to 700 rpm and an applied clamping torque of 5 Nm first and 4 Nm for the second weld. Later, 3 more tests were done with a

rotational speed of 1200 rpm and the screws fixed with torques of 30 Nm, 5 Nm and 7.5N m. In the first three tests with the friction material insert, temperature measurements were conducted, using only 3 thermocouples each, because all other thermocouples were already assigned to other tests.
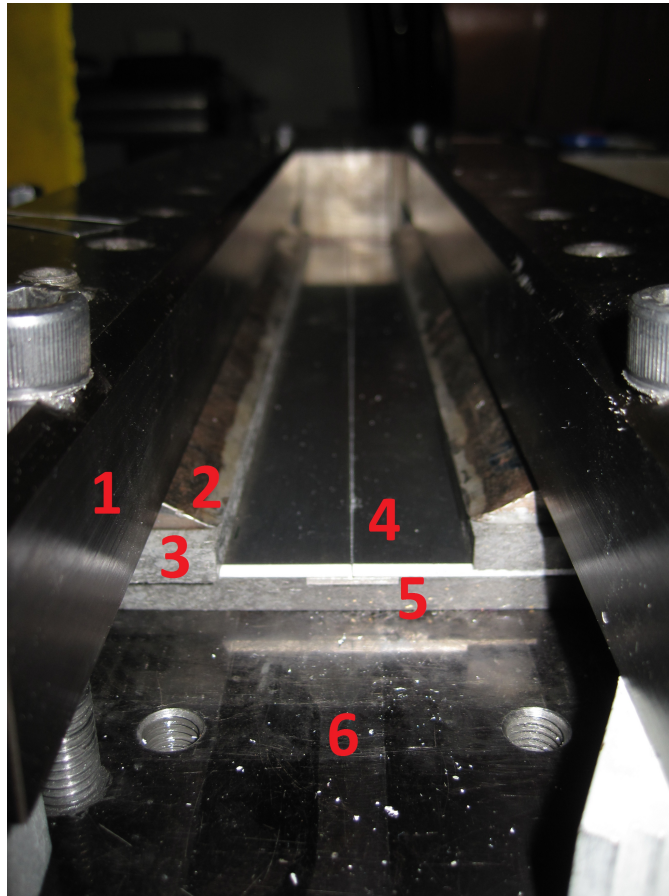
Figure 2.5: Example of assembled test structure: 1-clamping bar with M30 screws on its outer holes and M8 screws in the inner holes. 2-steel block to distribute pressure on coupon halves. 3-friction material to reduce heat loss to steel block and clamping bars (only used for tests with friction material as interstitial plate). 4-test sample halves, 5- interstitial material: in this case, the friction material with a Ti-6Al-4V strip to reduce smoke and avoid melting and stirring into the weld of caoutschouc, contained in the friction material itself, is displayed. Otherwise the 2mm thick Ti-6Al-4V plate takes its place. 5-steel backing
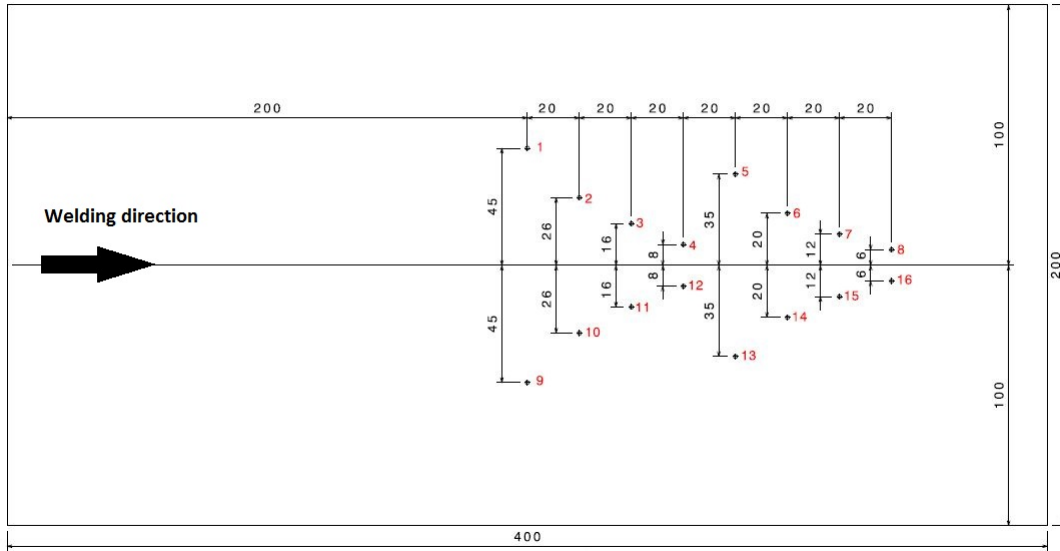
Figure 2.6: Measuring stations for thermocouples. In tests 2 and 3 all positions were occupied (symmetrical measurements). In the other, only the first 8 were used.

The most important tests for this work followed with a series of 6 probes. The coupon halves were fitted with type K thermocouples and applied as already described in section 2.3. From fig. 2.6 it should be noted that all thermocouples were placed in the second half of the coupons. This was done, to guarantee that a stationary process was reached before the thermocouples' positions. The goal was to obtain better measurements of the temperature's distribution. All of these welds were conducted with the "optimal" parameters reported in tab. 2.4, keeping the setup as constant as possible between one test and the other.

During these tests, an additional effort was made to measure the tool's temperature. In the 1st temperature measurement test, thermocouples were fixed on the tool's shoulder via heat-resistant tape, but the high temperatures during welding made the tape come off and at the end of the process the contact was not guaranteed any more, resulting in unreliable acquired data. For the following 3 temperature measurements tests, an estimation of temperature in the shoulder was made through the use of self-sticking 6 Levels TMC THERMAX indicator strips. These initially white/grey indicator strips are peeled off their protection

foil and applied to the shoulder[2]. Once the temperature in a certain level is reached , the strip blackens. This of course is an irreversible temperature measurement method. Nevertheless, it allowed to estimate the maximum reached temperature on the shoulder's surface.

(a)   (b)
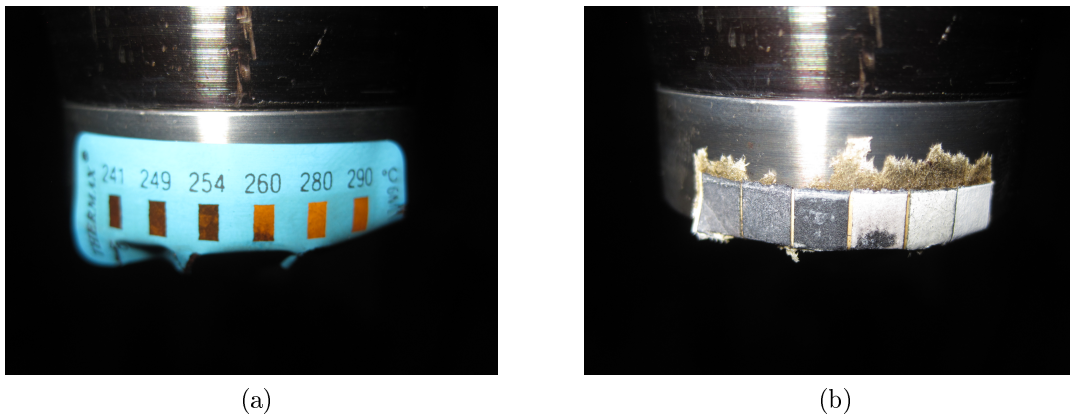
Figure 2.7: Blackened indicator strip applied to the tool's shoulder after the welding process for TM3 test in position 2

The vertical position of these strips was varied in order to capture the thermal gradient in the shoulder, while the horizontal position was kept constant throughout all tests. The positions of the maximum reached temperatures were measured with a 0.5 mm scaled ruler. Tab. 2.5 reports the maximum temperatures recorded during the various thermal tests.

---

[2]the shoulder's surface has been cleaned with ethanol prior to application of the strips to remove dust and any residual of grease
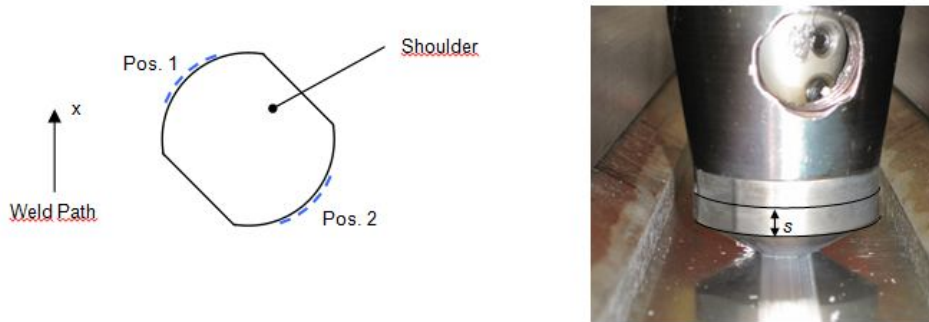
Figure 2.8: Shoulder used and position of application for TMC THERMAX thermal indicator strips

Table 2.5: Maximum temperatures recorded with thermal indicator strips, depending on distance s from the shoulder's edge between vertical and conical part

TEST	Pos.	Tmax [°C]	Distance s [mm]
TM2	1	249	4.5-5
TM2	1	241	6
TM3	1	224	8
TM3	1	216	9
TM3	1	210	>10
TM3	2	260	0.5-1
TM3	2	254	>3
TM4	1	260	1.5-2
TM4	1	254	5
TM4	1	249	6

A final test was conducted, trying to measure the temperature in the weld. Two thermocouples were placed between the coupon halves to weld (fig. 2.9) and one was placed underneath. As expected, all thermocouples were stirred into the nugget. Unfortunately, the acquired signal resulted useless, since the thermocouples ceased working properly, before they could register the real maximum temperatures. Therefore the maximum temperature of the process is still assumed being in between 400°C and 450°C (80%-90% of solidus temperature for Al2024 which is 502°C).
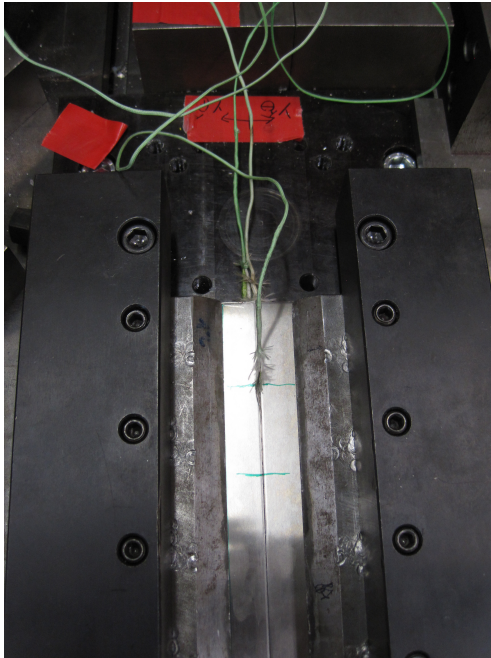
(a) Detail of temperature measurements in the weld line. The green lines represent the position of the TCs' measuring tips
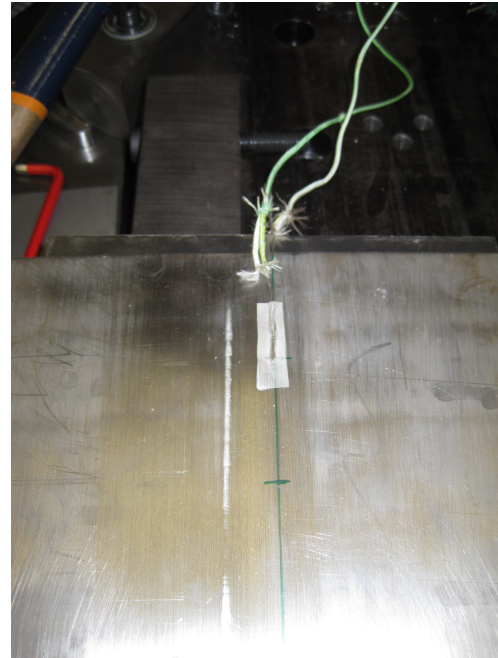
(b) Detail of temperature measurement between work piece and Ti-6Al-4V interstitial plate. The green lines represent the position of TCs' measuring tips in the work piece

Figure 2.9: TM7 test setup

2.4.1 Results and Discussion

The graphs, presented in fig. 2.10 through 2.15, were generated from the original data acquired during the performed thermal tests (TM1 through TM6). From these graphs, it can be seen that the time at which the maximum temperature is reached in a certain position, does not correspond to the time at which the shoulder is at the same y-coordinate. Therefore, there is a certain delay in time, e.g. for position 3 in fig. 2.10 the maximum peak is registered when the shoulder is at $y = 255\,\mathrm{mm}$, while the actual y coordinate of position 3 is at $240\,\mathrm{mm}$ ($15\,\mathrm{mm}$ of delay correspond to $4.5\,\mathrm{s}$ with the prescribed traverse velocity of $200\ \frac{mm}{min}$). This is attributed to different factors: the heat generated by the tool needs a certain amount of time to reach the TC's position; the further away from the measuring position, the more time it takes to reach the maximum value. A small portion of delay can be attributed to the measuring device, but its influence is neglectable, since it is applied to all measuring stations in the same manner.

In the following graphs, the position of the tool has been calculated by multiplying the sampling time by the tool's velocity. All curves have been translated by an initial starting offset (20 mm), corresponding to the beginning of the weld line.
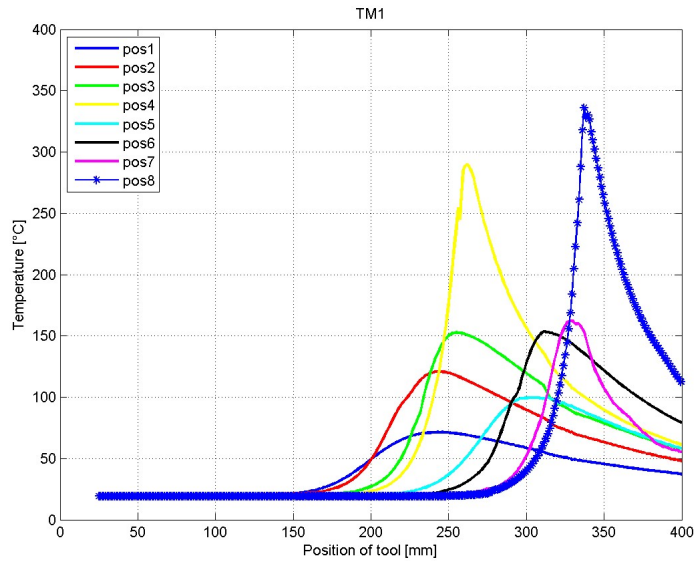
Figure 2.10: Correlation by position TM1
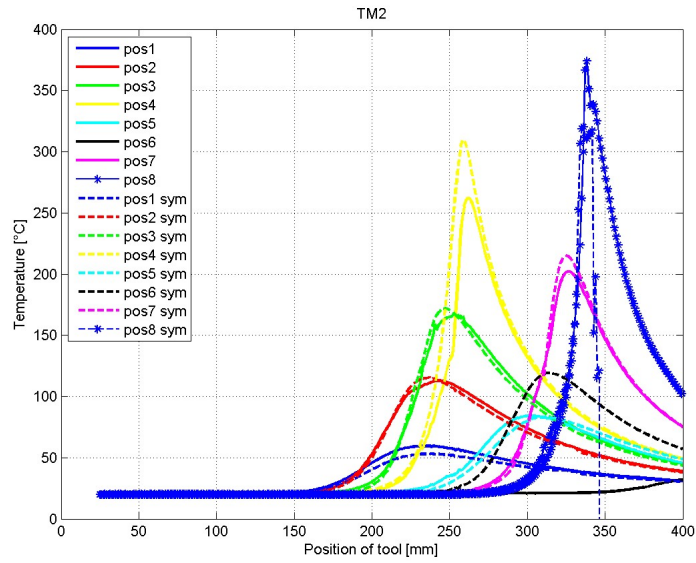
Figure 2.11: Correlation by position TM2
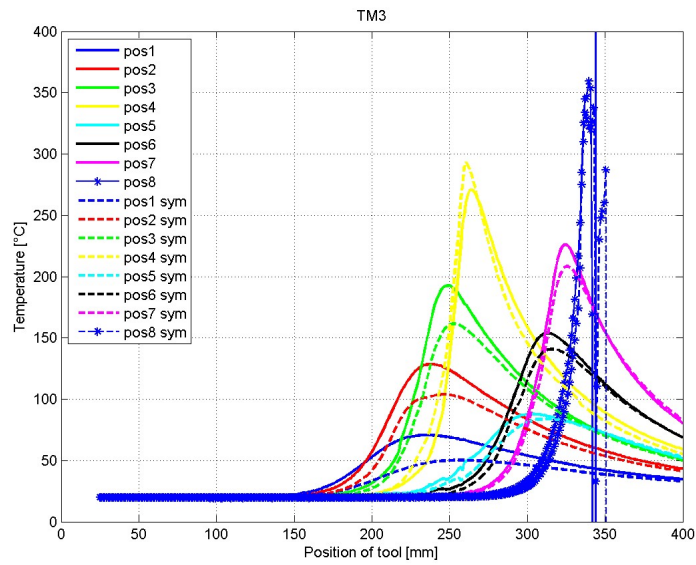
Figure 2.12: Correlation by position TM3
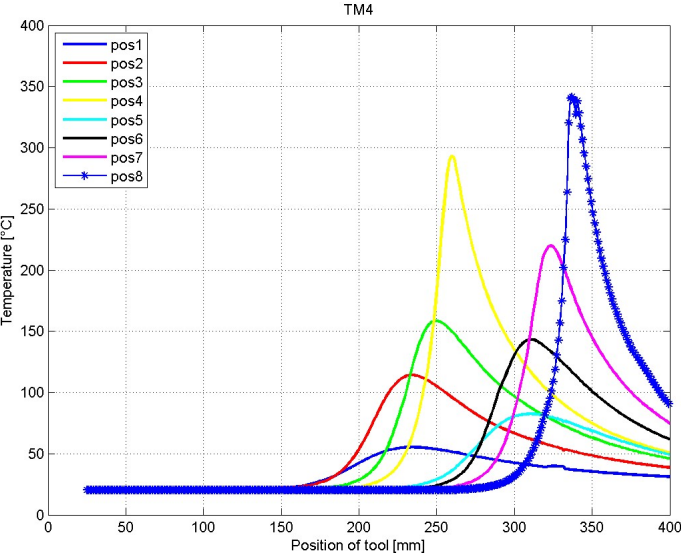
Figure 2.13: Correlation by position TM4
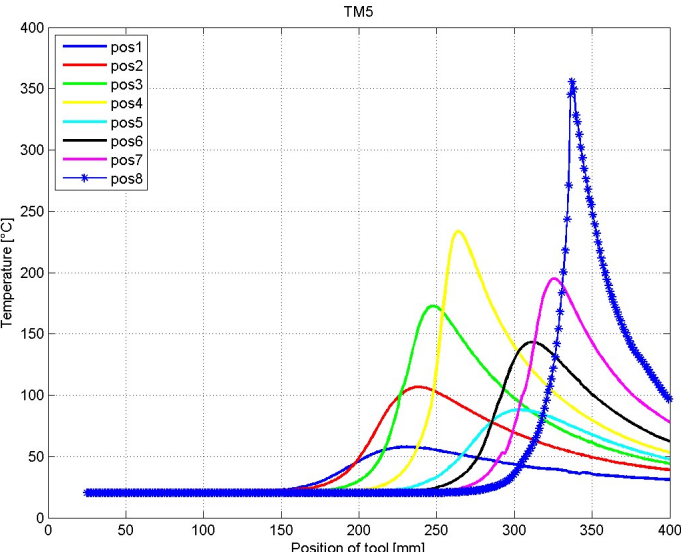
Figure 2.14: Correlation by position TM5
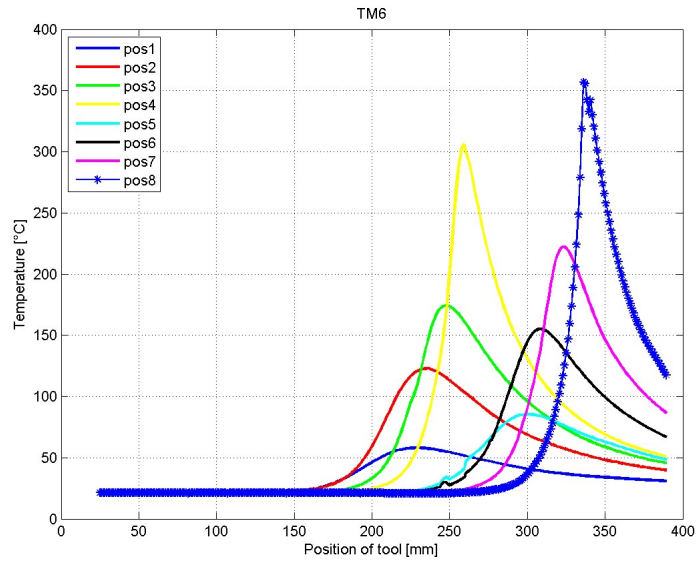
Figure 2.15: Correlation by position TM6

Data Manipulation

In order to get a better overview of the measurements obtained, it was necessary to group the different measurements for each position in one single graph. This required to manipulate the acquired data, since all measurements had different acquisition times. In fact, it was decided to consider only a range around the maximum temperature peak for each position (80 points in front of the maximum temperature and 47 after it). The x-axis has been shifted to obtain all peaks at the same instant.

The quality of measurements has been evaluated by looking at the graphs. Unfortunately, not all of them presented good trends. Possible sources of error were identified as:

- bad contact between thermocouples and workpiece

- deviation of the thermocouple's tip position from the theoretical position

- mechanical influence, e.g. interference during welding of the tool's shoulder with the thermocouples closest to the weld line

The latter was easily recognizible during the welding process, as well as visible in the acquired measurements through jumping of temperatures from one value to another and unrealistic trends (e.g. pos1 & pos1 sym in fig.2.12).

Detachment of thermocouples prior to the welding, are also, in part, identified as a source of error. These have been repositioned and fixed in their original position with a heat resistant tape; some of them presented anyway unrealistic temperature values.

Not all measured data seems to have sense and therefore not all curves can be used to calculate the average value. Tab. 2.6 reports the excluded curves for each position.

The averaged temperature curves are here presented for each measuring position, along with the maximum and minimum values of the considered data.

The temperature trend over the sample's width is given in fig. 2.24.

Table 2.6: X=excluded during calculation of mean value; * contact-loss before welding; ** contact-loss during welding process;

Position	TM1	TM2	TM3	TM4	TM5	TM6	TM2_S	TM3_S
1	*							
2	X	X						X
3	X*	X		*				
4		X			X			
5								
6		X					X	
7	X*							
8			X**				X	X
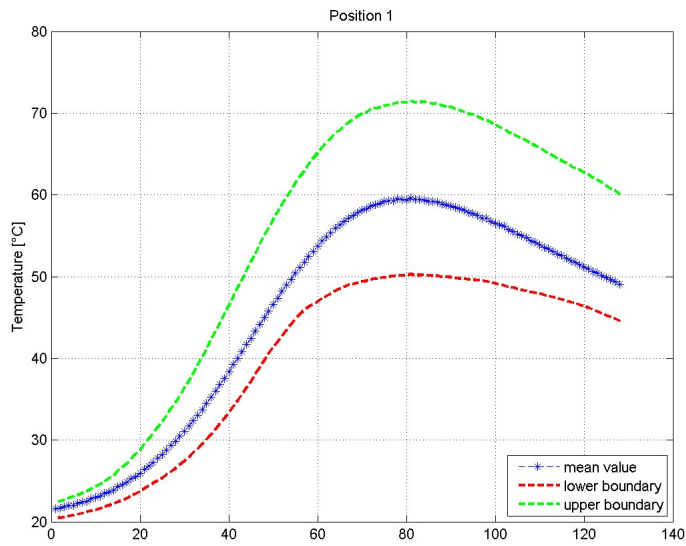
Figure 2.16: Average, max. and min. temperature for position 1
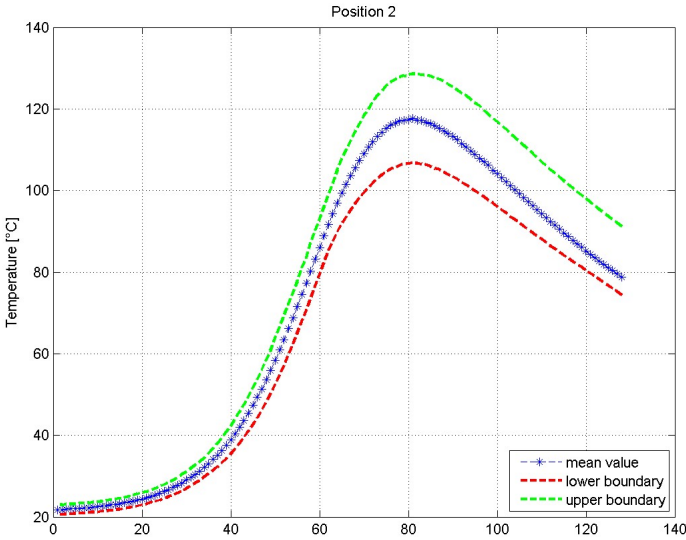
Figure 2.17: Average, max. and min. temperature for position 2
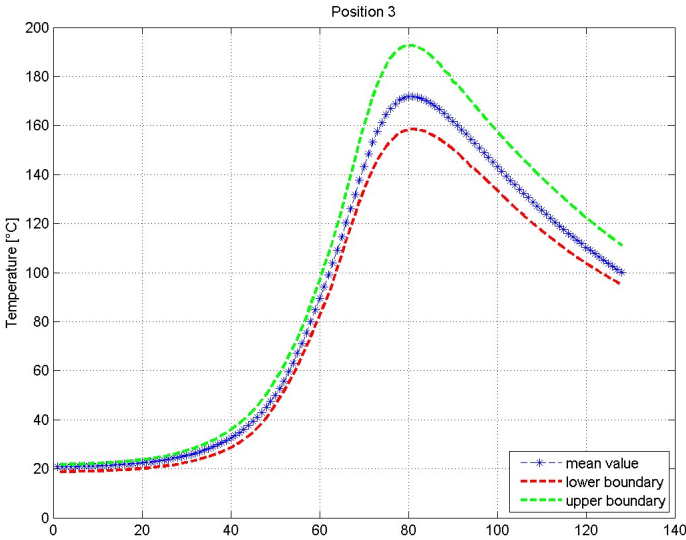
Figure 2.18: Average, max. and min. temperature for position 3
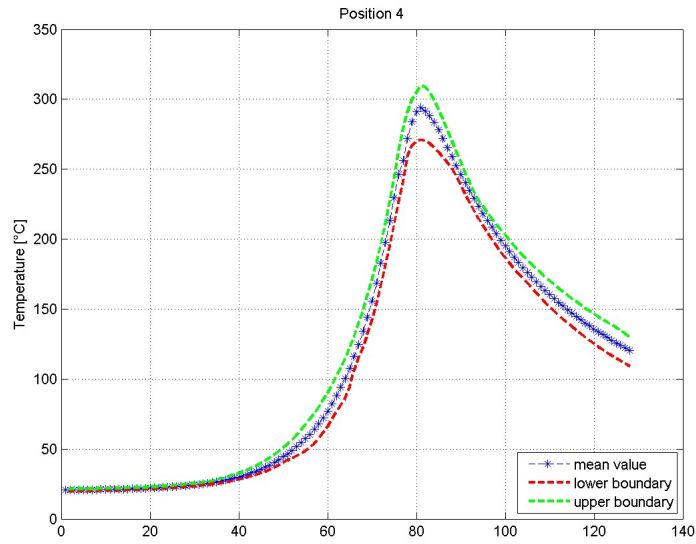
Figure 2.19: Average, max. and min. temperature for position 4
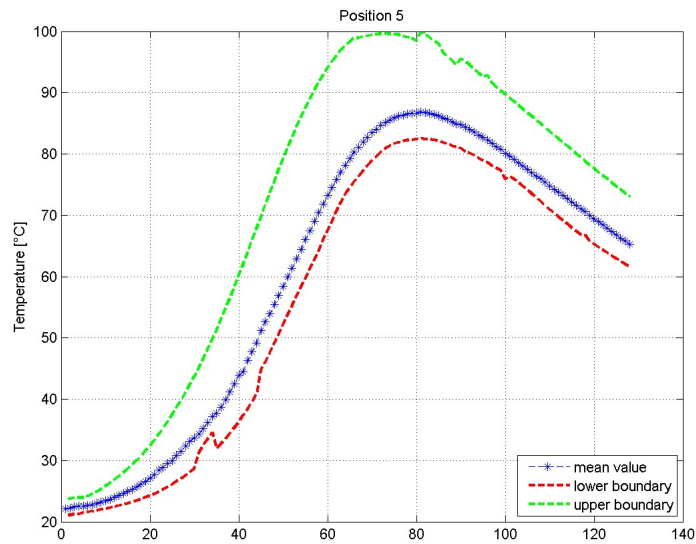
Figure 2.20: Average, max. and min. temperature for position 5
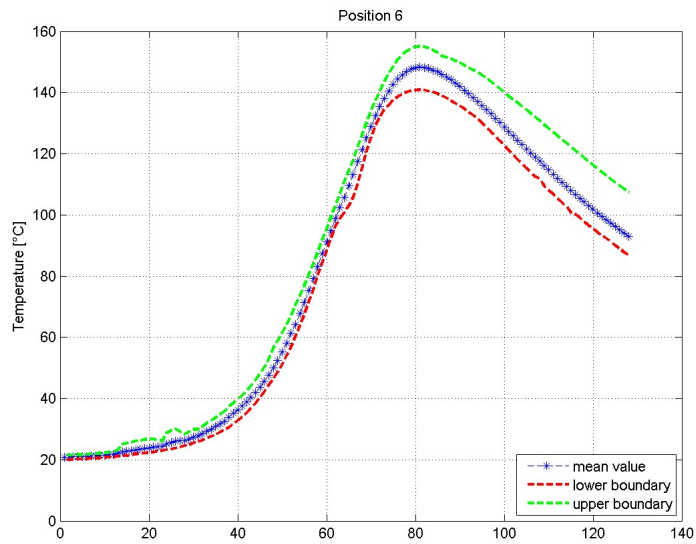
Figure 2.21: Average, max. and min. temperature for position 6
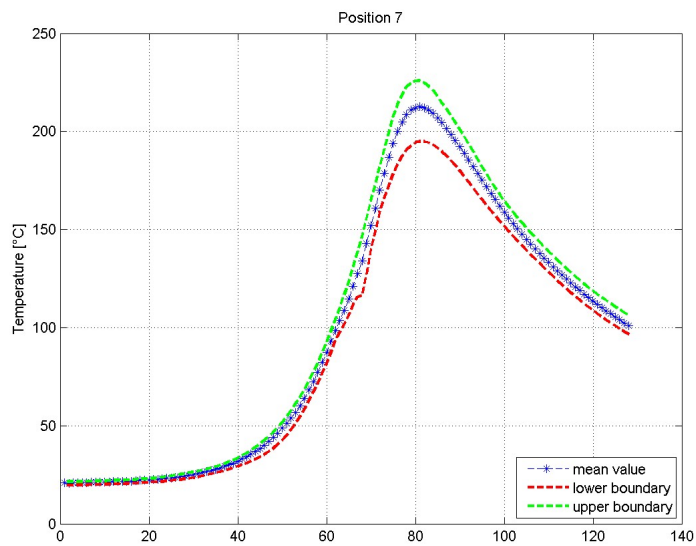
Figure 2.22: Average, max. and min. temperature for position 7
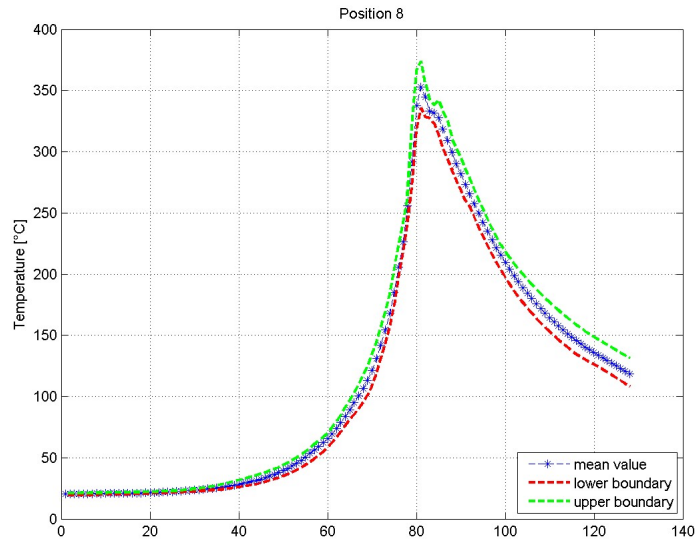
Figure 2.23: Average, max. and min. temperature for position 8
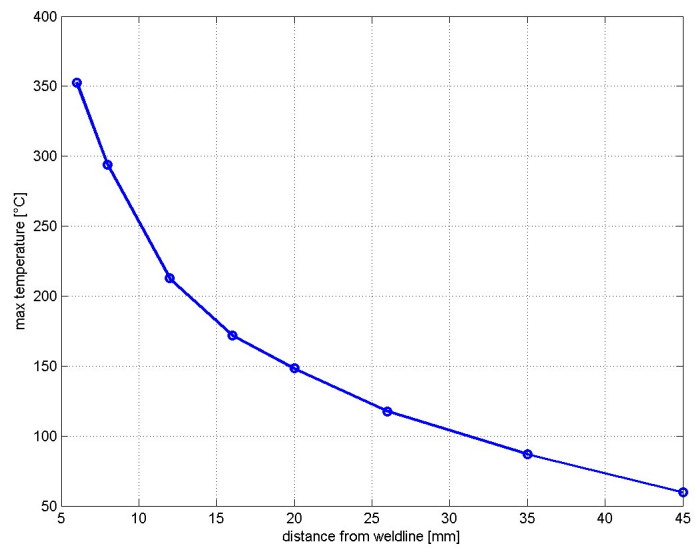
Figure 2.24: maximum of averaged temperatures plotted over the distance from the weld path.
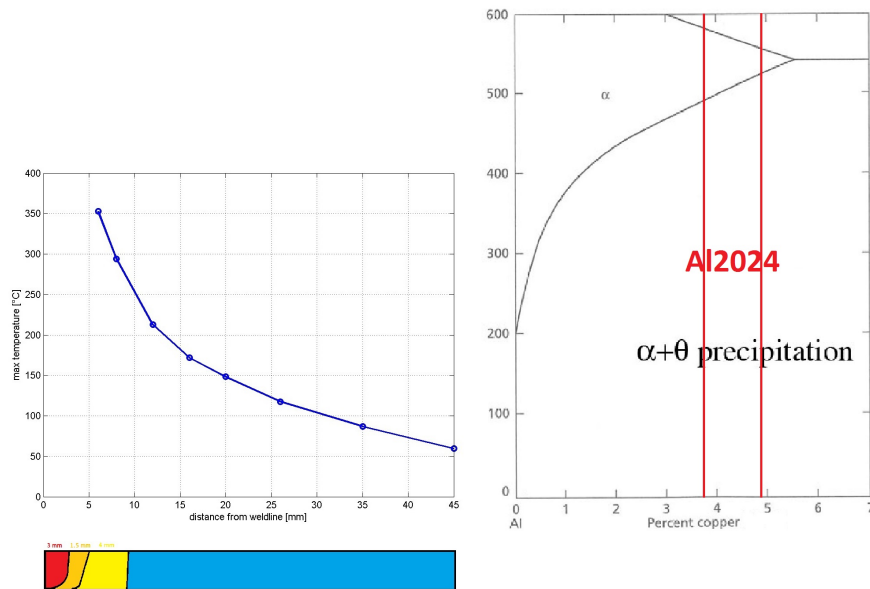
Figure 2.25: maximum of averaged temperatures plotted over the distance from the weld path, phase diagram for Al, schematisation of microstructure of coupon (red=nugget, orange=TMAZ, yellow=HAZ and blue=base material)

2.5 3rd campaign (January 2013)

Goals of this campaign are to lower uncertainities in terms of mechanical power input and global energy balance. The necessity of estimating the real power input (for simulation purposes), brought to conceiving a new clamping fixture, which should allow to measure the torque transmitted to the workpiece and the temperature in the backing plate.
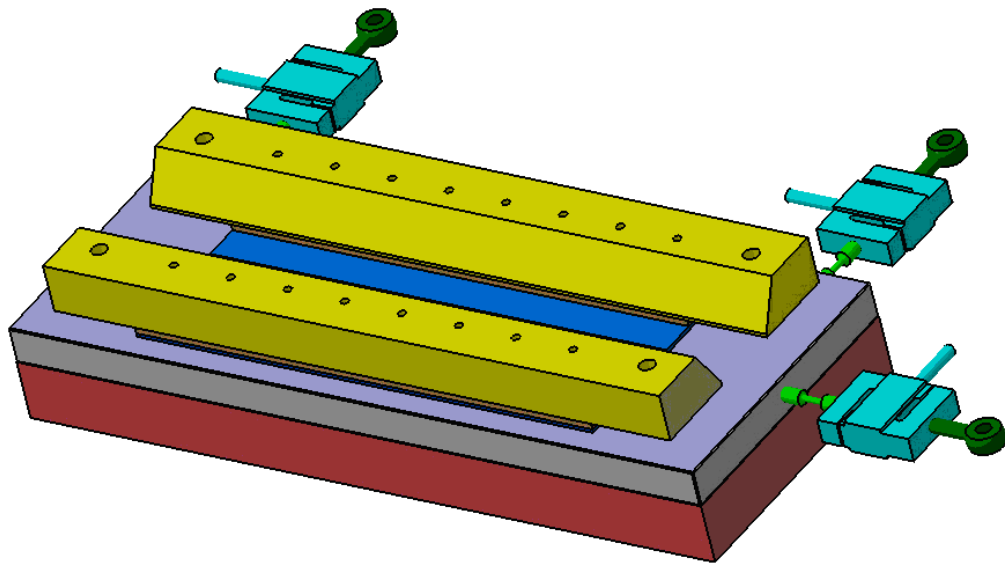
Figure 2.26: Design of the new clamping fixture: new backing plate, new clamping bars and load cells [28]

2.5.1 Temperature

The quantity of heat which flows into the backing plate is unknown, since apparently it has not been investigated by FSW-experts. In order to measure it, a temperature increase of about 5°C for the backing plate would be a good condition, due to the measuring imprecision of the available thermocouples.

Using the following expression:

$$Q = \sum_i \rho_i c_i V_i \cdot \Delta T \tag{2.3}$$

where i stands for the different materials involved, ρ is the density, c the specific heat, V the volume, ΔT the difference between initial and final temperature, and expressing it for V_{St} eq. (2.4) is obtained:

$$V_{St} = (\frac{Q}{\Delta T} - \rho_{Al} * c_{Al} * V_{Al} - \rho_{Ti} * c_{Ti} * V_{Ti})/(\rho_{St} * c_{St}) \tag{2.4}$$

With a very simple calculation, neglecting convection, and estimating the power through the numerical simulation in $600\,W$, it is calculated that the steel backing should not have more than $0.0037\,\mathrm{m}^3$ of volume. Considering a backing plate a bit larger and wider than the workpiece, for example $600\,\mathrm{mm} \cdot 240\,\mathrm{mm}$, this leads to a thickness of $25.9\,\mathrm{mm}$. This backing plate could not withstand the loads occurring during the clamping and the workening. From here on it was necessary to find a compromise between the possibility of measuring the temperature in the backing plate and the desired stiffness of the whole fixture. Calculations have been performed by Kraus and by Merlin and can be found in [28].

Results indicate that for this steel backing plate a minimum thickness of $30\,\mathrm{mm}$ is required. This thickness has been found to be sufficiently small to obtain an increase in temperature, which is measurable with the available thermocouples.

Therefore, the new backing plate has been fitted with 9 thermocouples. These were placed into $15\,\mathrm{mm}$ deep drilled holes in different positions, as can be seen in fig. 2.27. Temperatures were measured only on one side of the backing plate, because the process is considered fully symmetrical.
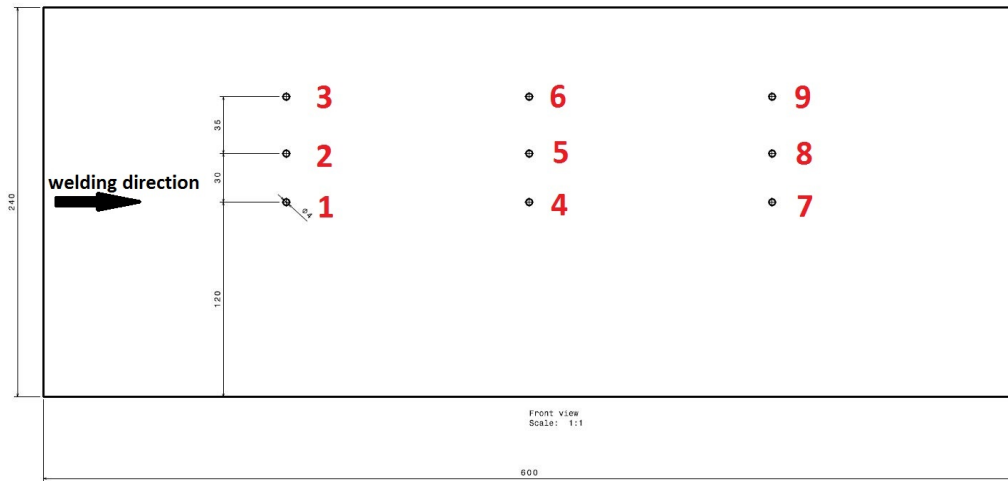
Figure 2.27: Positions of thermocouples on the new backing plate

To get an idea of the total thermal energy introduced into the test assembly, different options were evaluated: Ideally, if the whole test structure is perfectly thermally isolated from the environment, and after waiting an infinite time, the whole structure will have the same temperature everywhere. In this ideal case, it becomes very simple to calculate the total thermal energy input through eq. (2.3).

Since the temperature is ideally uniform throughout the whole structure, the temperature can be measured at any point.

In reality it is not possible to isolate the assembly from the rest. The robot has to access the workpiece and no perfect thermal insulation exists: heat is lost primarly through conduction, but also through convection and radiation, which is here considered neglectable.

To reduce the loss of heat through conduction a polystyrene layer is placed under the steel backing. Conduction loss through the tool and therefore the robot is unavoidable during the welding process. After the weld is performed, and the robot retracts its arm from the workpiece, the whole assembly could be closed into a thermally isolated box. Unfortunately, the available insulation materials and the need of waiting a long time until the temperature is nearly uniform, makes it impossible to preserve the total heat in the structure.

A first idea, was to place the whole backing, prior to welding, into an open box and leave the structure at least for one night in the laboratory, so that it could reach its environment's temperature. As soon as the robot arm retracts

itself, a lid would be placed on top of the box to prevent heat loss through convection and a precise amount of water, at environmental temperature, would flood the structure. This would significantly lower the waiting time, thus making it easier to better estimate an approximated (because thermal energy will be lost through conduction, convection and radiation during the welding process and the box will have a certain thermal resistance, but will not be a perfect insulation) heat input.

With the designed structure, estimating the water needed in 5 liters, without considering any heat loss to the environment and using the through simulation estimated heat input, a uniform final temperature increase inside the box of 1.2°C is expected. Due to the very low temperature increase and the connected uncertainities, this method seems to be completely ineffective in estimating the total heat input.

In order to understand how much heat is lost through convection, and if a complete wrap-around thermal insulation is really necessary, thermal simulations have been used: the complete model was first run with a natural convection coefficient of $5 \frac{W}{m^2 K}$ and a second thermal simulation was run without the convection. The difference in total thermal energy in the model with convection, compared with the model without convection, represents the heat loss through convection. For details, refer to section 3.10 Energy Loss Investigation on p. 92.

Estimation of Torque and Thermal Insulation:
The material used as thermal insulation during testing is polystyrene for house building insulations. A 50 mm thick insulation was applied to shield thermally the backing plate, in order to reduce the heat transfer from backing plate to the work table. Unfortunately, the whole cannot be screened completely, because of the connection to the force transducers. However, specially designed screws, with a reduced midlength cross section, reduce the heat conduction. On the lateral sides of the backing, the same insulation has been used, while an emergency blanked placed on its top prevented convection from above, during the cooling phase.

Figure 2.28: Particular of screws with a reduced midlength cross section
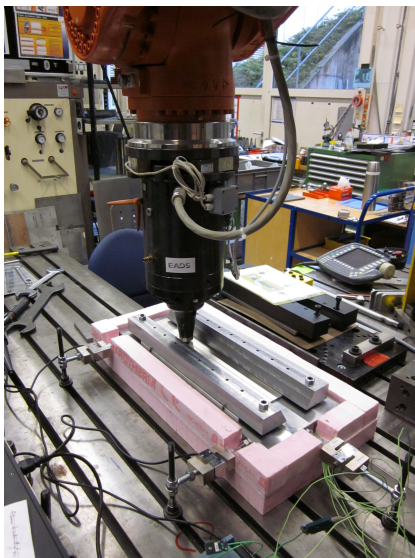
(a) welding phase of coupons: no effort is done to prevent loss through convection or through conduction via shoulder and body of robot.

(b) in the emergency blanked packed structure to prevent heat loss through convection (cooling phase)

Figure 2.29: Test setup
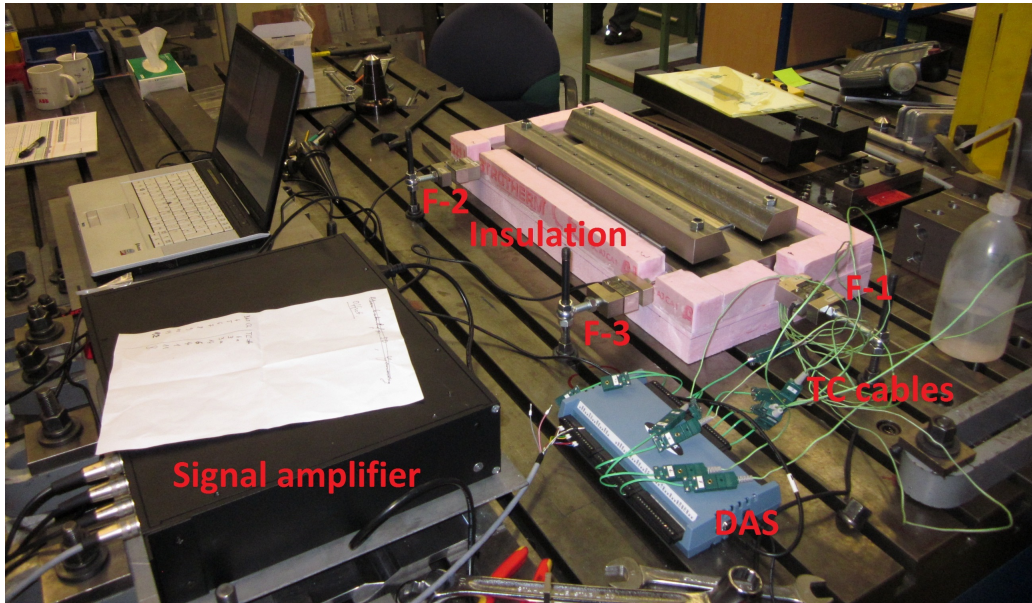
Figure 2.30: Test setup: Along with the already used Data Acquisition System (DAS) and the notebook, the force transducers (F-1 through F-3) and the signal amplifier are here shown. The pink-coloured polystyrene is clearly visible.

2.5.2 Forces

The primary goal of this new backing plate is to allow the measurement of forces provided by the robot, which act onto the workpiece. Measurements were performed via 3 S-type load cells, more precisely the Bosche S20S-G3-1000 load cell. The 3 load cells were connected, through a signal amplifier, to the DAS, as can be seen in fig. 2.30.

Several cuts, creating longitudinal slots for every 10 mm of insulation and slots every 40 mm perpendicular to the welding direction, were made to reduce the polystyrene insulation's stiffness. This should allow to acquire correctly the applied forces during the welding process and later to calculate the moments deriving from the tool's rotation.

2.5.3 Handling

Taking it a step further, the necessity of reducing set-up time and of having a better distribution of clamping forces, makes it indispensable to strive for a new clamping device (fig. 2.31). A good concept is to use a constructed hydraulic

clamp, as described in [24] and developed in [28]. The idea is to use the latter backing, with the displayed clamping bars. These will have only two screws on their ends to keep the bars in place. Inside these hollow bars, a rubber tube will be filled with oil (green part). By raising pressure inside this hosepipe, clamping forces will be generated (the red metal parts are pressed against the workpiece). Once the provided clamping force is measured over the desired oil pressure, it will be very easy and quick to set the correct, and always the same, clamping forces by simply looking at a manometer.

Due to the lack of time before the 3rd test camapaign and the necessity of designing and producing the new clamping fixture, this has not yet been used.
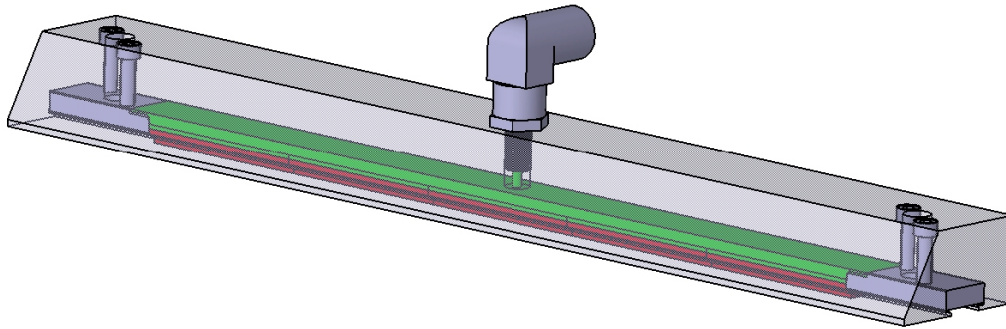
Figure 2.31: Concept of new fixture [28]

2.5.4 Results and Discussion

Prior to testing, all the set-up with thermocouples and force transducers was tested in the offices at RUAG Aerospace Structures and both thermocouples and force transducers were working properly. However, on testing day, one major problem emerged: the thermocouples' signals were disturbed by some sort of interference: the output signals were totally absurd. The load cell's signals, instead, did not oscillate and had an ouput signal of about 0V in an unloaded condition.

The first source of error thought of, was that the instruments were grounded with different mass lines. However, once they were connected all to the same mass, nothing changed. A second step was to unplug force transducers from the DAS, but this again did not bring any advantages. The only thing, which led to a drastic reduction of interference, was to switch the signal amplifier off.

It then became clear that only 4, out of the original 9, thermocouples were providing reasonable results, even though a disturbing signal was still present. The first reasons for these signals to think of, could be either detachment or breakage of the thermocouples. However, experience acquired during the second test campaign, allowed to prove these as wrong, since for broken thermocouples the output temperature jumps to $-10000°C$, while detached thermocouples still provide a clean signal, even though the temperature value is completely wrong.

In fig. 2.32, for example, two types of problems can be seen: 5 thermocouples have a very low initial temperature, which absolutely does not correspond to the backing's temperature, coupled with a very noisy signal. The other thermocouples present a decent trend, even if some noise is present.

A possible source of error for the not properly working termocouples could be that air humidity contained in the hole condensed on the TC's measuring tip during the night prior to testing. This would lead to a malfunction of the thermocouples. For the noise, the most plausible explanation is an electromagnetic interference.

Since no other source of error could be found at the moment, and since testing time was limited, it has been decided to procede with testing anyway.

The sampling frequency during all testing was 4 Hz. Trying to reduce the interference, the temperature measurements were subsequently filtered numerically at 1Hz. Still, the senseless trend of 5 TC made it impossible to consider these measurements for use (see tab. 2.7).

Table 2.7: Thermocouples in backing

thermocouple	working
pos1	NO
pos2	NO
pos3	NO
pos4	NO
pos5	YES
pos6	NO
pos7	YES
pos8	YES
pos9	YES
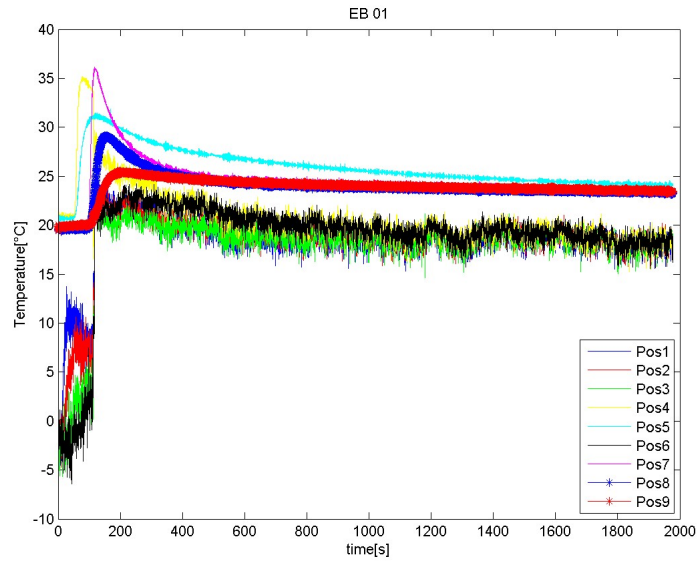
Figure 2.32: Example of non filtered temperature acquisition from EB 01 test
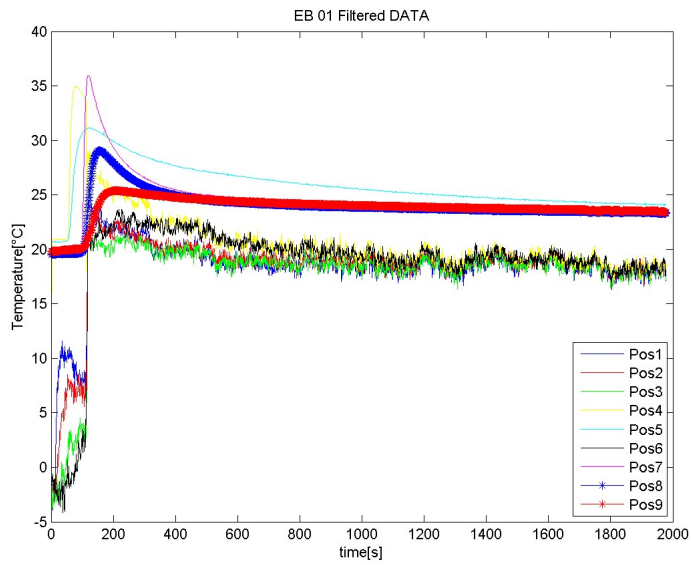
Figure 2.33: Example of filtered temperature acquisition from EB 01 test
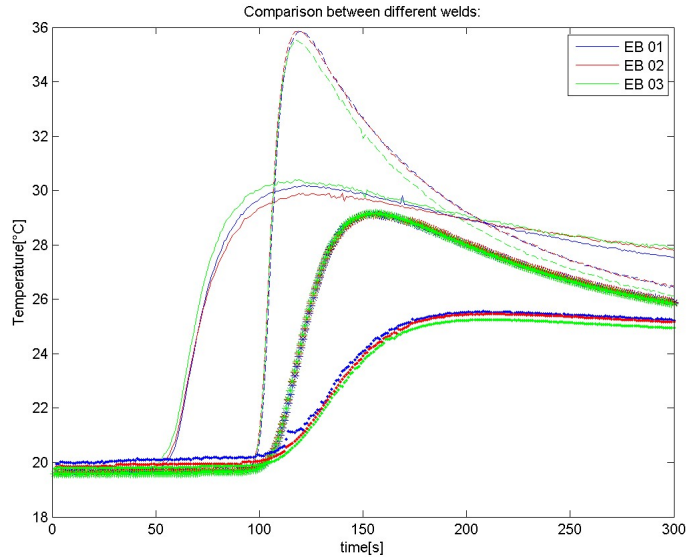
Figure 2.34: Comparison between the 3 different tests performed: only reasonable thermocouples data is displayed. Pos5=continuous line; Pos7=dashed line; Pos8=stars; Pos9=circles

Total Thermal Energy

A rough estimation of the total thermal energy in the structure, resulted possible through the evaluation of the last test results. Especially the temperature in the backing over a relatively long time, while separated from the environment through the insulation on its bottom and sides, and through the emergency blanket on top, provided very important information. To calculate the total thermal energy, a basic assumption of considering only the backing plate, the intersitital Ti plate and the workpiece is made. The bars are neglected, since they were still cold after removing the emergency blanket, while the rest was perceptibly warm.

Looking at the temperatures for positions 7 through 9, a $\Delta T \approx 4$°C between the initial and final temperatures can be seen: the initial temperature oscillates between 19.49°C and 19.79°C, while the temperatures after half an hour of cooling time ($t_{tot} = 1920$ s) oscillate in a wider range between 23.19°C and 24.78°C. However, most of the curves are in between 23.45°C and 23.69°C, thus leading to a temperature increase of about 4°C.

Using eq. (2.3) for the mentioned parts, a thermal energy of $Q = 66145$ J

56

is estimated, and considering a welding time of $108s$ (which corresponds to the time required to weld 360 mm with a traverse speed of $200\,\frac{mm}{min}$), a power input of 612.5 W is calculated.
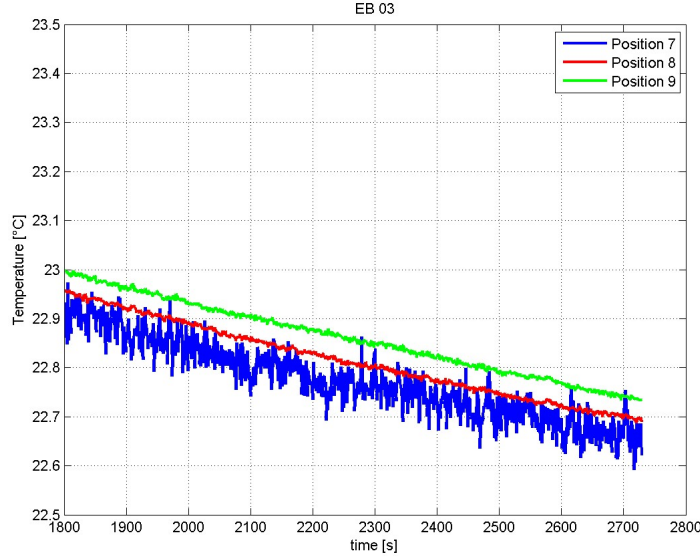
Figure 2.35: Detail of EB_03 test. Data used for calculation of lost energy

Calculation of lost energy during cooling inside the insulation and estimation of a corresponding heat convection coefficient

After 30 min from the beginning of the welding process, the temperature is uniformly distributed in the test structure. This can be easily verified in 2.8: the temperatures at position 7, 8 and 9 are almost the same at $t = 1800$ s. The temperatures at this instant ($t = 1800$ s), and at the last acquisition time have been subtracted and the lost energy estimated again through eq. (2.3). Assuming a mean temperature decrease of $\Delta T = 0.2567°C$ (from fig. 2.35), the following thermal energy is obtained:

$$Q = 4245\,\text{J}$$

The lost power is given by:

$$P_{lost} = \frac{Q}{\Delta t} = \frac{4245\ \text{J}}{929\ \text{s}} = 4.569\ \text{W}$$

57

Considering an external surface of 0.3384 m^2 (which corresponds to the whole surface of the backing plate) and with an environment temperature of 19°C, the following corresponding heat convection coefficient is calculated:

$$h_{conv} = 3 \, \frac{W}{m^2 K}$$

This coefficient represents the heat loss through conduction into insulation and then through convection, but for simulation purposes, it can be set as a single film coefficient with the reported value.

Table 2.8: Temperatures recorded in the backing plate in position 7 through 9 when a uniform temperature had been reached, and at the last recorded instant

Position	time [s]	recorded temperature [$°C$]
7	1800	22.93
	2729	22.69
8	1800	22.95
	2729	22.69
9	1800	23
	2729	22.73

Forces Measured, Calculation of Torque and Estimation of Total Power Input

Forces were measured in 6 tests, following the temperature acquisition. During these tests, the force applied by the robot to the testing structure was immediately visible on the signal amplifiers displays. The analog ouput of the signal amplifier has been set to $0 - 5\,\text{V}$. The data was acquired through the DAS, where the voltage has been measured.

To be able to calculate the forces, a correlation between force and voltage needs to be done. This has been carried out, after the testing day, due to the limited time before. To be able to relate the voltage with the actual forces, all three load cells were tested separately at RUAG's facility. The load cells were loaded, once at a time, with known weights. The same measuring chain as during weld tests (signal amplifier + DAS) has been used. Through comparison of the loads applied and the voltage output, a linear relation between these two quantities has been obtained, through the coefficient reported in 2.5. This allowed to well approximate the values of the forces measured through the

acquisition system[3].

$$c_F = 2002.4 \frac{\text{N}}{\text{V}} \tag{2.5}$$

Once the forces were unequivocally determined, it became clear that something went wrong during testing. In fact, the compressive forces were much lower as expected. Taking a better look at the signal amplifier's manual [29], it became clear that with the settings used, a problem of compression force voltage cut-off was present. In fact, the analog output range had been set to $0 - 5$ V. The transmitter effective range is between -0.150 V and 5.500 V and it considers the zero laod condition at 0 V. Therefore, the compressive forces were recorded for forces corresponding up to -0.150 V. Compressive forces above, were simply cut off. It has been found that in order to measure well both compressive and tensioning loads, a measuring range from -5 V to 5 V should've been chosen. To do this, two jumpers need to be soldered (fig. 2.36), creating a short-circuit.
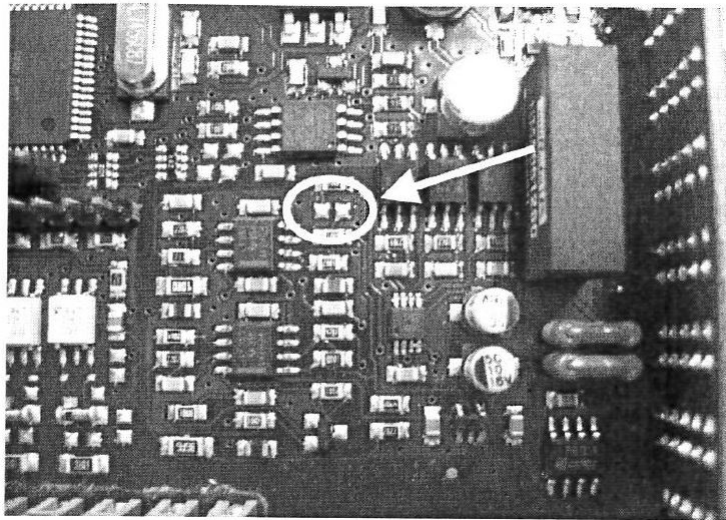
Figure 2.36: Image of WTB transmitter's circuit board. The two highlighted jumpers need to be shortcircuited in order to obtain a symmetrical measuring range

It has been chosen to proceed anyway with the calculation of the torque, because of the expected small influence of this problem on the data retrieved

---

[3]The coefficient has been found to be equal for all three load cells.

from load cells F-2 and F-3. (fig. 2.30). During the welding process, the lever arms keep changing due to the travelling velocity of the tool. Considering this, the calculated torques are displayed in fig. 2.37. In the two following figures a cubic spline has been used to interpolate the test data.
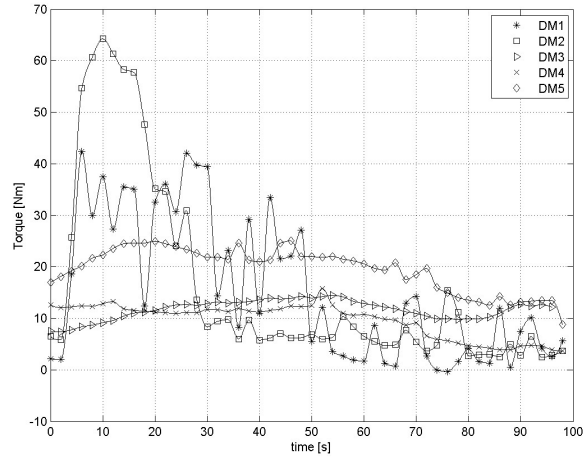
Figure 2.37: Calculated torque for the various tests; forces are filtered at 0.5Hz
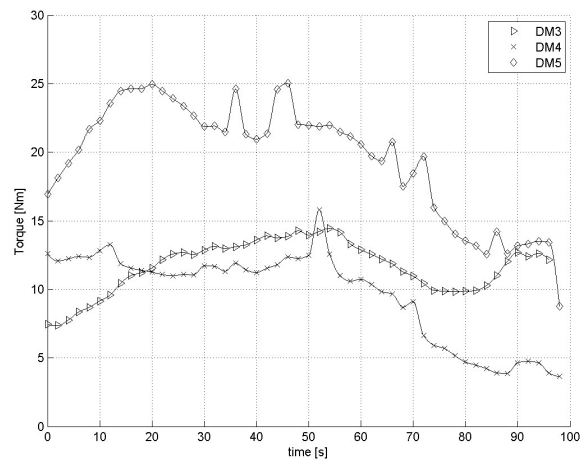
Figure 2.38: Torques calculated from tests DM3, DM4 and DM5. Tests DM1 & DM2 are not considered, due to the too high oscillation of the curves

The calculated torques present very different values for each weld test. From the obtained values, it is very difficult to estimate the power input.

Through eq. (2.6) the power input can be estimated. However, due to the very scattered data, it results very difficult to obtain a single value.

$$P = \omega \cdot T \tag{2.6}$$

where ω represents the rotational velocity in $\frac{rad}{s}$ and T the torque.

The average values of the torques measured for the each test (tab. 2.9), clearly show the huge variation of calculated power input.

Table 2.9: Average of calculated torque for each test

Test	Average Torque [Nm]
DM 01	15.4427
DM 02	15.9542
DM 03	11.6751
DM 04	9.6454
DM 05	19.5613

Using eq. (2.6) power inputs between 1212 W for test DM 04 and 2458 W for DM 05 are obtained. Both values seem to be exaggeratedly high, considering that part of the torque is lost to friction between the polystyrene support and the work table.

In general, this testing campaign did not lead to the expected discoveries. The torque measurements, did not bring useful information: the calculated power input is an order of magnitude higher than for the other estimations. The calculated mechanical power input seems to be influenced more than expected by the already discussed voltage cut-off problem. Therefore, the data cannot be treated as very reliable. However, important information on the total thermal energies was collected: the here estimated thermal power input is close to the one estimated through simulations.

3 Numerical Model

3.1 General

All numerical simulations were performed using the MSC Marc 2012 solver software, while the pre-and post-processing has been done through MSC Mentat, the pre- and post-processor specifically developed for Marc by the same software house. MSC Marc is especially advised for non-linear and thermal problems. The simulations to be run, were non-linear fully coupled thermo-structural analyses in which the welding process needed to be reproduced. Since the welding feature is present in Marc, and for its capability in running coupled analyses, Marc is suitable (and available).

All simulations were run using the updated lagrangian solver, with the Full-Newton-Raphson iterative procedure and the large strain option.

The aim of numerical simulation is to reproduce the temperature distribution in the workpiece obtained during testing and to obtain distortions, comparable to those of the welded workpieces. During the development of this work it became clear that the numerical results were mostly used to support the understanding of the FSW process and validate the test results.

The whole testing structure needed to be idealized for simulation purposes. In fact, the numerical model reproduces correctly the whole test assembly, except for the clamping bars and their screws: these have not been modeled. They are needed only for fixing purposes, reproduced through displacement constraints in the model. The clamping bars, do not warm up, since their contact to the whole assembly is only through the screws. For all simulations a finer mesh has been chosen for the zone around the weld line, while coarser meshes have been used for the Ti-plate, the backing plate and the distanciation pieces. These parts are only needed to act as heat sinks and, since no deformation is expected, a larger mesh is acceptable with the advantage of computational cost reduction. All meshes are made of Hex8 elements and reported in tab. 3.1, except for the the shoulder which was discretized through Tet10 elements due to its geometry.

For this work it was necessary to understand how to perform the thermal analysis, which cards and parameters were to set and to find the most important parameters through research in the existing literature, along with correcting and updating the model continously.
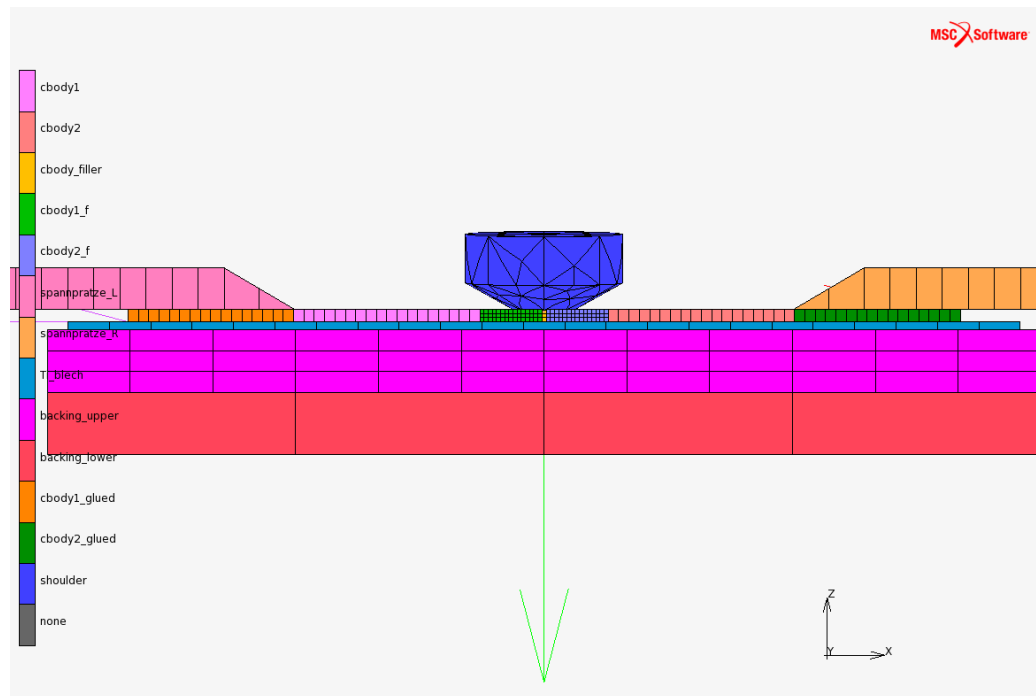
Figure 3.1: Final model

3.1.1 Backing and Fixture

For the first simulations, only the workpiece has been modeled. Over time, the model has been constantly developed and the steel backing, the interstitial Ti-6Al-4V plate and the so-named distanciation pieces have been introduced. The meshes of these parts have been constantly developed, trying to obtain a perfect balance between computational costs and reliability of results. After the 3rd testing campaign of January 2013, the model of the backing has been updated with the new geometry. All these parts have been modeled with their true geometry and meshed with Hex-8 elements. The steel backing has been divided into two different meshes: a finer mesh on the upper half, while a more coarse mesh has been used for the bottom part. This was done to reduce the number of elements, thus the computational cost.

3.1.2 Shoulder

The shoulder has been modelled with the actual outer geometry (dimensions from confidential drawings). The hollow parts have not been modelled. This does not correspond to reality. However, it has been chosen to keep this design. In reality the heat flows from the shoulder to the spindle and then into the robot's arm. In simulations, these parts were not modelled. By raising the shoulder's mass, the amount of energy lost through the shoulder is better approximated as with a hollow shoulder. Therefore, this approximation is here considered acceptable.

The shoulder has been modelled as a rigid solid with heat transfer capability and meshed with 255 tetrahedral 10-nodes elements.

In reality the robot's arm is force controlled, to guarantee the shoulder's correct plunge depth. In the model, no external forces are acting on the shoulder: the correct plunge depth is simply set through the shoulder's position and inclination. The only degree of freedom left is the translation in longitudinal direction (parallel to the weld line). This allows to set the correct tool's forward velocity and to coordinate its movement with the travelling heat source.

Table 3.1: Mesh of the final model

Piece	Contact body and mesh size (x,y,z) [mm]	Number of elements
Workpiece	filler elements 1x1x1	1080
	cbody_f 1x1x1	18000x2
	cbody 2.5x2x3	3600x2
	cbody_glued 2.5x2x3	3200x2
Ti-plate	10x10x2\	920
Backing	upper 20x20x5	1080
	lower 60x60x15	40
Distanciation pieces	6.3x10x10	480x2
Shoulder	Tet10 mesh	255

3.2 Numerical Aspects of Welding Tools in Marc/Mentat

3.2.1 Weld Filler Elements

MSC Mentat is provided with a specific toolbox for welding processes, where the weld filler and the weld path need to be assigned. Weld fillers are the volume, which during conventional welding processes is added between the materials to join. The software requires to define all elements which need to be treated as

filler. These elements represent the volume added over time during the welding process.

Once that the filler characteristic has been assigned, different options are available. Filler elements can be defined either as deactivated elements or as quiet elements [30]. The fundamental difference consists in the dynamic creation of these filler elements. For the quiet element method, the elements are already present in the model with scaled down properties: the coefficient of thermal expansion α is set to zero, while all other properties, except yield stress, specific heat and thermal mass density, are typically scaled down with a default factor of 10^{-5}. This coefficient can be changed by the user.

The second way to define the filler elements is the deactivated method: the filler elements are not initially present in the model, but they are created as the heat source moves on.

In order to know when the elements need to be created, a filler bounding box is defined. All elements in the box, at any given increment, will be either created or activated, based on the method chosen. This box can be either defined by the user, or set to default. In the case of default box, it is defined by $X_b = 1.5$ times the weld pool width, $Y_b = 2$ times the weld pool width and Z_b by the weld pool length. These quantities are better described in section 3.3.2.

Both methods allow to define the temperature that the elements have when they are created (melt point temperature) and a temperature activation time, which is the time delay of activation of the filler's mechanical properties after the thermal properties activation. For the simulations run, none of these features has been used. This means that during simulation, the elements are created with a temperature of 20°C (respecting the initial condition). These are then heated up through the thermal power provided by the torch. The mechanical properties of the created elements are immediately activated (no delay time is set).

Friction stir welding, as described previously, is not a conventional welding technique, thus no filler is needed. Nevertheless, in order to simulate the process, it was necessary to define filler elements along the joining line. These consist of 1080 1·1·1 mm^3 deactivated elements, placed between the two coupon halves. No melt point temperature is defined, because all heat input is defined through the heat source. The bounding box is set to default. The size of these filler elements was defined by numerical problems. Ideally, filler elements should have a width of 0.2 mm to reproduce correctly the gap between the coupon's halves. However, this brought to continuous crashing of the analysis due to too large deformation

of these elements. A solution has been found through the definition of bigger elements, with a contact interference closure (contact offset) which allows to reproduce the correct gap of 0.2 mm.

3.2.2 Weld Path

The other option required by MSC Marc for simulation of welding, is the weld path or weld line. First, the geometrical entity needs to be created, which has been done through a straight curve. Then, the weld path properties need to be assigned, e.g. the weld torch orientation. Different options are available to define the orientation of the weld path coordinate system, e.g. curves, vectors or Euler's angles. For this application, the definition through a vector ($[0, 0, -1]$) seemed to be the best way. As can be seen in fig. 3.2 the blue arrow (z direction) needs to be pointed towards the weld path, while the green arrow (y direction) represents the weld orientation. The x vector is automatically obtained.

(a) Local coordinate system for moving source obtained by translation and rotation of global coordinate system

(b) Correct set up of the moving source
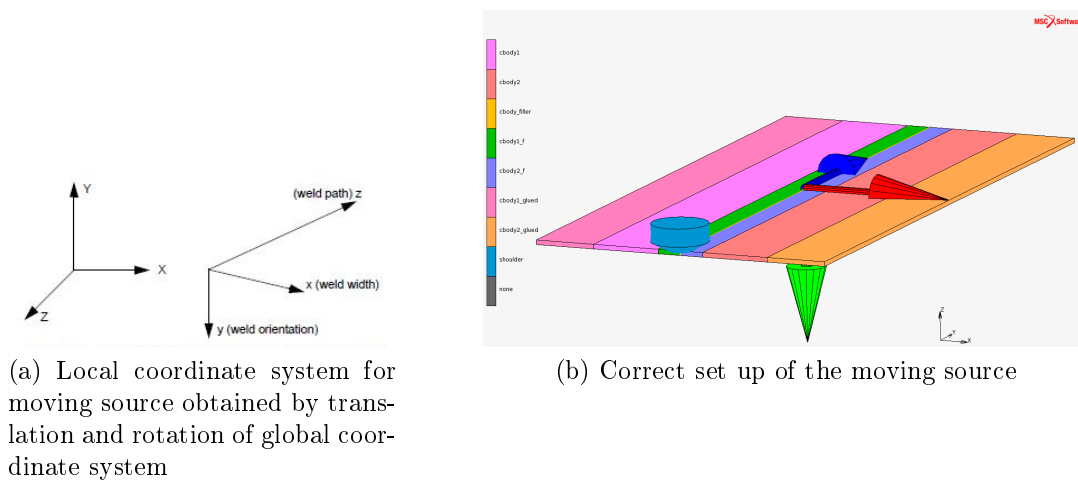
Figure 3.2: Moving heat source coordinate system

3.3 Initial and Boundary Conditions

3.3.1 Initial Temperature

An initial temperature of 20°C (room temperature) has been chosen and applied to the whole model. This has been done by selecting all model's nodes and applying the initial temperature condition.

3.3.2 Heat Source

The heat source is defined as a boundary condition in Mentat. Different types of heat sources are already available in the preprocessing software and others can be implemented through a user subroutine. Referring to [31], MSC implemented the described heat sources, precisely Pavelic's disc shaped heat source and Goldak's double ellipsoidal shaped weld heat source [30]. A closer look to the latter is taken, due to its utilization in this work.

Goldak et al. [31], first defined the so-called Ellipsoidal Power Density Distribution:

As described in their paper, the Gaussian distribution of power density in an ellipsoid with center at the origin and semi axes a,b,c parallel to coordinate axes x, y, ξ can be written as:

$$q(x, y, \xi) = q(0)e^{-Ax^2}e^{-By^2}e^{-C\xi^2} \tag{3.1}$$

where q(0) is the maximum value of the power density at the center of the ellipsoid, and A, B and C are constants that will be defined later.

Evaluating the equation of energy conservation, eq. (3.2) and (3.3) are obtained.

$$2Q = \frac{q(0)\pi\sqrt{\pi}}{\sqrt{ABC}} \tag{3.2}$$

$$q(0) = \frac{2Q\sqrt{ABC}}{\pi\sqrt{\pi}} \tag{3.3}$$

where Q is the applied power.

To define the constants A, B and C, the semi axes of the ellipsoid a, b, and c in the direction x, y, ξ are chosen such that the power density falls to 0.05q(0) at the surface of the ellipsoid.

Therefore in the x-direction:

$$q(a, 0, 0) = q(0)e^{-Aa^2} = 0.05q(0) \tag{3.4}$$

From eq. (3.4) , it is immediate to find the value for A:

$$A = \frac{ln(20)}{a^2} \approx \frac{3}{a^2} \tag{3.5}$$

In analogy with the above procedure, the values for constants B and C are obtained:

$$B \approx \frac{3}{b^2} \tag{3.6}$$

$$C \approx \frac{3}{c^2} \tag{3.7}$$

Combining eqs. (3.5), (3.6), (3.7), (3.3) and substituting them into eq.(3.1) the ellipsoidal heat source is obtained:

$$q(x, y, \xi) = \frac{6\sqrt{3}Q}{abc\pi\sqrt{\pi}} e^{-\frac{3x^2}{a^2}} e^{-\frac{3y^2}{b^2}} e^{-\frac{3\xi^2}{c^2}} \tag{3.8}$$

Although this definition could seem a relatively good approximation of what happens in reality, it has been proven that it contains some errors. In fact, the temperature gradients in front of the heat source is not as steep as in reality, while the gradient in the rear is steeper than in experimental experience made by Goldak [31]. This brought to the definition of the double ellipsoidal heat source, which allowed to better reproduce experimental observations. This one simply consists of 2 ellipsoids, where the front half of the source is the quadrant of one ellipsoid and the rear part is the quadrant of the other.

Marc uses Goldak's double ellipsoidal heat source with the following equations:

for the front half of the source:

$$q_f(x, y, \xi) = \frac{6\sqrt{3}f_f Q}{abc_f\pi\sqrt{\pi}} e^{-\frac{3x^2}{a^2}} e^{-\frac{3y^2}{b^2}} e^{-\frac{3\xi^2}{c^2}} \tag{3.9}$$

and for the rear:

$$q_r(x, y, \xi) = \frac{6\sqrt{3}f_r Q}{abc_r\pi\sqrt{\pi}} e^{-\frac{3x^2}{a^2}} e^{-\frac{3y^2}{b^2}} e^{-\frac{3\xi^2}{c^2}} \tag{3.10}$$

where f_f and f_r are dimensionless factors that represent the fractions of heat deposited in front and rear quadrants of the source, and are defined as:

$$f_f = \frac{2}{(1 + \frac{c_r}{c_f})} \tag{3.11}$$

$$f_r = \frac{2}{(1 + \frac{c_f}{c_r})} \tag{3.12}$$

where c_f and c_r are the forward and rear weld pool lengths in the weld path direction z;

The sum of eq. (3.11) and (3.12) is always equal to 2.
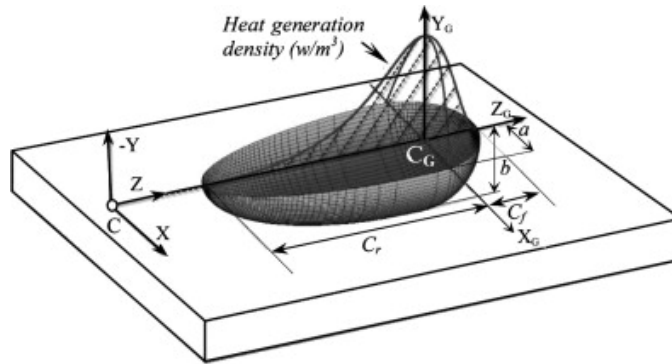
Figure 3.3: Double ellipsoid heat source according to Goldak

The volume weld flux card in Mentat contains different subparts. In the first, the definition of flux parameters is requested, and more specifically the power of the heat source and its efficiency. In all simulations performed, an efficiency of 1 is always assumed. More details on this issue are discussed in section 3.2 Energy balance.

The second part of the card, contains the dimensions of the weld flux, which are obtained through the probe's dimensions[4] and are reported in table (3.2).

Other important parameters like the initial weld position and velocity of the heat source can be set. In this work the initial position is defined by the first point of the weld path curve, hence making it senseless to redefine a new welding initial position, while the forward velocity of the heat source is set to $0.003333333\,\frac{m}{s}$ ($200\,\frac{mm}{min}$)

In this card, it is necessary to refer to the previously defined weld filler element and weld path element cards.

A very important remark is that Goldak's double ellipsoidal volume flux function exactly results in the requested heat power, only in case that the volume integration is done over an infinite volume. In Marc the integration volume is limited to an ellipsoid defined by the dimensions of the heat source. Therefore, a systematic deviation of 11.48% from the requested power input has been noticed

---

[4]diameter of $5\,\mathrm{mm}$ and penetration depth of $2.8\,\mathrm{mm}$

during simulations (fig. 3.4). The waviness of the calculated power input is due to approximations of numerical nature.
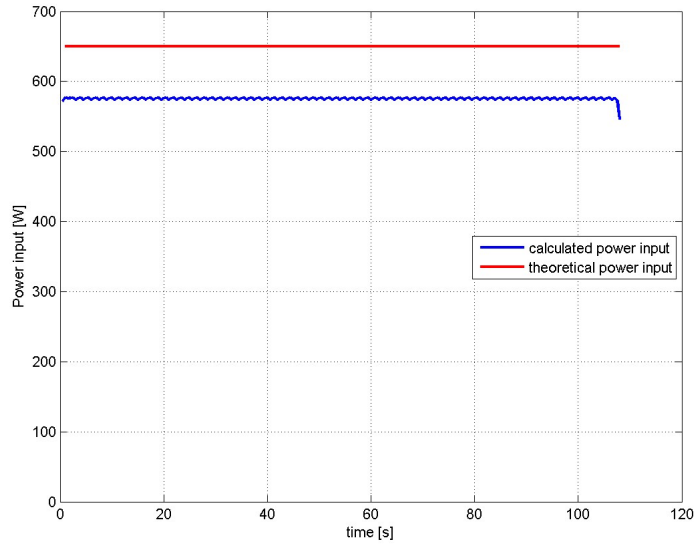
Figure 3.4: Difference between requested power input and effective power input calculated by Marc

Table 3.2: Dimensions of heat source

Width [mm]	5
Depth [mm]	2.8
Forward length [mm]	2.5
Rear length [mm]	2.5

Table 3.3: Example of power input used during the development of the model

requested power input	650 W
calculated power input	575.3620 W (mean value)
effective power in the model compared to the requested input	88.52%

3.3.3   Heat Transfer

A very important part of this work, is to define all thermal aspects of the materials and of the whole structures. Therefore, along with the implentation of the material's conductivity, dependent on temperature, and an estimation of the natural convection coefficient, contact conductance between materials can't be neglected. These thermal contact conductance coefficients play an important role during the transient of the welding process, affecting both temperature gradients and deformation.

These coefficients depend mainly on the contacting materials, their surface roughness, applied pressure and temperature. Very limited information has been found. The contact conductance coefficient between the aluminium plate and the steel clamps was estimated through the use of fig. 3.5. The data was transformed to S.I. units and with an applied pressure of 4.17 MPa, as previously reported in tab. 2.1, a contact conductance coefficient of $467.9 \frac{W}{m^2 K}$ was obtained. The materials used for testing do not correspond to the materials reported in fig. 3.5, but no better data was available.
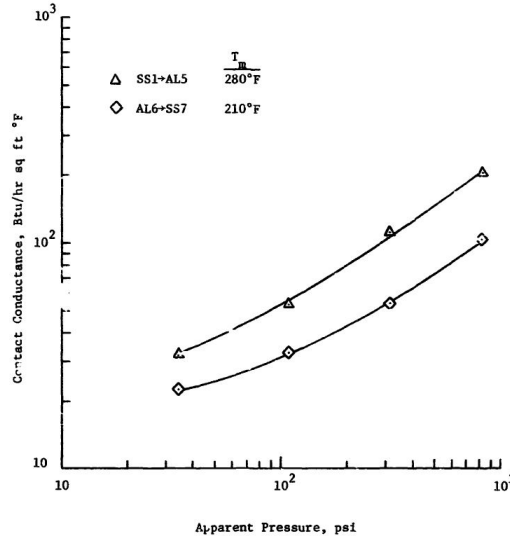
Figure 3.5: Contact conductance Vs. pressure for pure aluminium - stainless steel contact (SS1: stainless steel with smooth surface, SS7: stainless steel with rough surface, Al5 and Al6: pure aluminium with rough surface) [32]

Contact conductance coefficients at the Al2024-T3 - Ti-6Al-4V transition and at the Ti-6Al-4V - S235 tranisition remain unknown. A contact conductance coefficient of $150 \frac{W}{m^2 K}$ was initially set between the Al2024-T3 and the Ti-6Al-4V, based on preliminary simulation and correlation with results of the 1st test campaign. However, no coefficient was set for the tranisition between the interstitial Ti-plate and the steel backing, considering a perfect thermal contact (thermal contact resistance equal to 0).

3.4   Loadcases

In order to simulate correctly the process, 3 different loadcases are needed:

- loadcase weld: the heat source (and the shoulder) travel along the weld line. The two coupon's halves are joined together through the creation of the filler elements.

- loadcase cool: the heat source is deactivated and no contact between shoulder and workpiece is present. The workpiece is cooled for 120s (time to reach a uniform temperature distribution in the workpiece)

- loadcase release: all contacts between workpiece and surrounding structure are removed. in order to avoid a crashing of the analysis due to lability of the workpiece, this had to be constraint (fig. 3.6)

For each loadcase the contact conditions are changed. The different contact tables are presented in section 3.5.
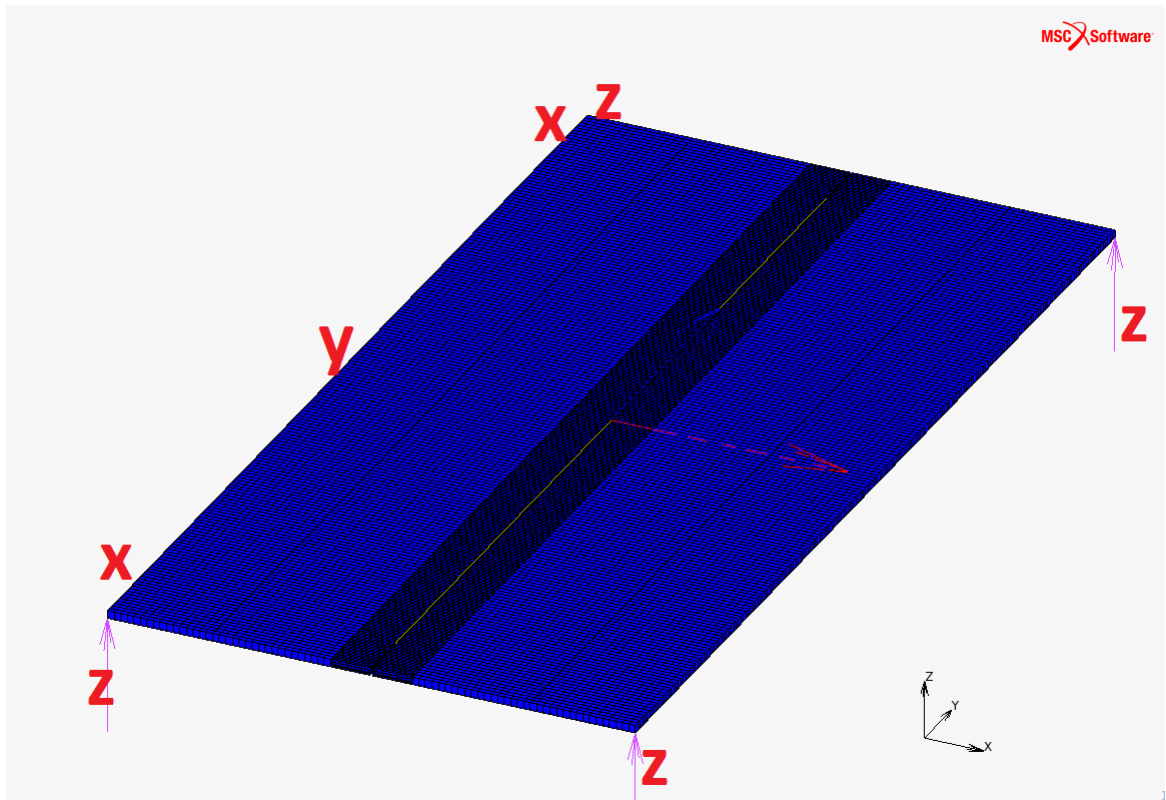
Figure 3.6: Schematization of constraints on workpiece for loadcase release

3.5 Contacts

For the definition of contacts in the model, the prior creation of contact bodies is required. This is nothing but the creation of a set of elements, grouped in a contact body. In this model, both definitions of deformable and rigid contact bodies were used.

The nodes on the contact bodies' external surfaces are treated as potential contact nodes: these are the nodes that might contact another body or itself. Another fundamental aspect of deformable bodies is defined by the faces of the solid elements. These are treated as potential contact segments [30]. Attention should be paid when defining contact bodies, because each node and element should be defined in only one contact body. Marc automatically recognizes nodes on the exterior surface, thus facilitating the user's work. Initially, contact bodies should not be penetrated, unless an interference fit calculation is intended.

In general, it is sufficient to define rigid bodies with their outer surfaces. However, if thermal aspects are to be considered, the use of heat transfer elements is essential. In this thermal/structural coupled analysis the shoulder has been modeled with rigid heat transfer elements.

In case of thermal or thermal/structural coupled analysis, rigid bodies can act as heat sources or heat sinks if defined through a curve or surface. Whenever an actual heat transfer through the rigid body needs to be studied, the rigid body should be defined with heat transfer elements. In this case Marc performs only a thermal analysis for the rigid elements. Obviously, the same results can be obtained through the definition of all deformable bodies, specifing a very high stiffness for the ideally rigid body. The disadvantage, compared to the definition of a rigid body with heat transfer elements, is in terms of higher computational costs.

When defining contacts, an absolute separation stress threshold helps to reduce the number of separations per increment and therefore the number of cycles per increment, thus the total calculation time. In this simulation a separation stress of 1 MPa has been applied to obtain a good compromise between realistic behaviour of the workpiece and calculation time.

Two types of contact definitions are available: contact touch and contact glue. The contact touch option essentially does not allow bodies to penetrate. The only constrain is non penetration, while separation and relative sliding are allowed. Contact glue, instead, couples the degrees of freedom of one contact body interface to the other contact body. Penetration, separation and relative sliding are all inhibited. Basically it is nothing but a contact touch with, ideally, infinite friction coefficient and separation threshold. A very high value for these two parameters is set, i.e. 10^{20}.

For thermal analysis a heat transfer contact coefficient between bodies can be defined; if not set, a perfect thermal contact is considered.

Distance tolerance, which is the maximum distance at which two parts are considered touching each other, for solid elements is automatically calculated by Marc as $\frac{1}{20}$ of the smallest element size in the model.

For the purpose of controlling rigid bodies, different options are available:

- prescribed position

- prescribed velocity

- prescribed load

- prescribed scaling

The position can be defined through a time-dependant table. If the velocity is given, the position is determined by an explicit forward integration of the velocities based upon the current time step.

Prescribed positions and velocity methods have less computational costs, than the prescribed loads method. The scaling option allows to reduce or amplify the size of the rigid body during simulation. If this condition is used, attention should be paid to the increment or reduction of size applied, because a too big change is likely to cause instabilities.
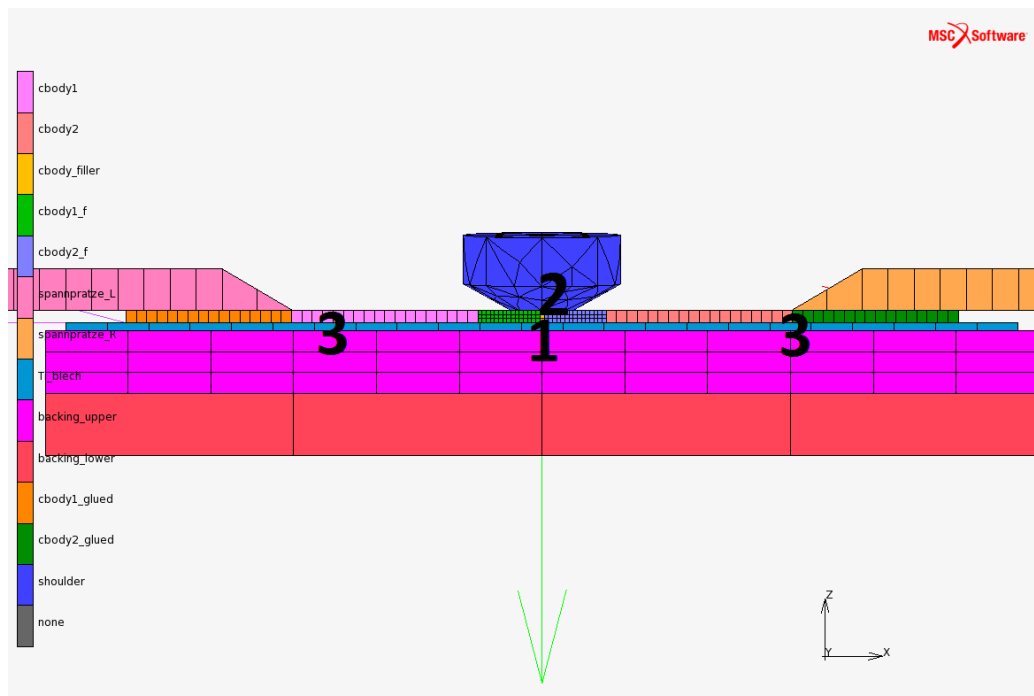
Figure 3.7: contact bodies of final model. The numbers represent the thermal contact conductance coefficients: 1-contact between fine mesh of workpiece and Ti-plate h_c=10000 $\frac{W}{m^2 K}$; 2-contact between workpiece and shoulder h_c=100000 $\frac{W}{m^2 K}$; 1-contact between coarse mesh of workpiece and Ti-plate or distanciation pieces h_c=1000 $\frac{W}{m^2 K}$;

First	#	Body Name	Body Type	1	2	3	4	5	6	7	8	9	10	11	12	13
							Second									
First	1	cbody1	deformable				G		G		T			G		
	2	cbody2	deformable					G		G	T				G	
	3	cbody_filler	deformable				G	G			T					T
	4	cbody1_f	deformable	G		G		T			T					T
	5	cbody2_f	deformable		G	G	T				T					T
	6	spannpratze_L	deformable	G										G		
	7	spannpratze_R	deformable		G										G	
	8	Ti_blech	deformable	T	T	T	T	T				G		G	G	
	9	backing_upper	deformable								G		G			
	10	backing_lower	deformable									G				
	11	cbody1_glued	deformable	G					G		G					
	12	cbody2_glued	deformable		G					G	G					
	13	shoulder	heat_rigid													

(a) contact table for loadcase weld

First	#	Body Name	Body Type	1	2	3	4	5	6	7	8	9	10	11	12	13
							Second									
First	1	cbody1	deformable				G		G		T			G		
	2	cbody2	deformable					G		G	T				G	
	3	cbody_filler	deformable				G	G			T					
	4	cbody1_f	deformable	G		G		T			T					
	5	cbody2_f	deformable		G	G	T				T					
	6	spannpratze_L	deformable	G										G		
	7	spannpratze_R	deformable		G										G	
	8	Ti_blech	deformable	T	T	T	T	T				G		G	G	
	9	backing_upper	deformable								G		G			
	10	backing_lower	deformable									G				
	11	cbody1_glued	deformable	G					G		G					
	12	cbody2_glued	deformable		G					G	G					
	13	shoulder	heat_rigid													

(b) contact table for loadcase cool

First	#	Body Name	Body Type	1	2	3	4	5	6	7	8	9	10	11	12	13
							Second									
First	1	cbody1	deformable				G							G		
	2	cbody2	deformable					G							G	
	3	cbody_filler	deformable				G	G								
	4	cbody1_f	deformable	G		G										
	5	cbody2_f	deformable		G	G										
	6	spannpratze_L	deformable													
	7	spannpratze_R	deformable													
	8	Ti_blech	deformable									G				
	9	backing_upper	deformable								G		G			
	10	backing_lower	deformable									G				
	11	cbody1_glued	deformable	G												
	12	cbody2_glued	deformable		G											
	13	shoulder	heat_rigid													

(c) contact table for loadcase release

Figure 3.8: contact tables of the final model

3.6 Material Properties

During the first simulations, constant (over temperature) properties for the workpiece were assumed. Constant material poperties were also assumed for the parts, introduced during the development of the model. Properties, such as thermal expansion coefficients, thermal conductivities, densities and the Young's moduli were taken from known sources [33, 34, 35].

In tab. 3.4 the used material properties are displayed. For the steel parts, no coefficient of thermal expansion (CTE) has been set, because the temperatures reached in the backing are very low compared to the rest. Therefore, the expansion can be considered null.

Table 3.4: Material properties of distanciation pieces, backing and Ti interstitial plate

Material	density$[\frac{kg}{m^3}]$	Poisson's coefficient	Young's Modulus [MPa]	conductivity $[\frac{W}{mK}]$	specific heat $[\frac{J}{kgK}]$	CTE $[\frac{m}{mK}]$
S235	7800	0.3	210000	50	500	none
Ti-6Al-4V	4430	0.342	113800	6.7	526.3	temp dependent
Al2024-T3	2780	0.33	72000	temp. dependent	temp. dependent	temp dependent

With the refinement of the model, it was necessary to better define the material properties for the workpiece. At the beginning, a simple yield stress temperature-dependancy has been introduced (fig. 3.9). This led to the definition of an elastic perfectly plastic model. Further material properties should've been obtained from an external work, commissioned to the Helmholtz-Zentrum Geesthach. Initially, it was planned to receive this information by December 2012, January 2013 at the latest. Unfortunately, the delivery time of the material properties shifted to approximately July 2013. Therefore it became necessary to retrieve the stress strain curves at different temperatures (20-450°C range) from literature.

Although it seems unreal that stress-strain curves of Al2024 were never obtained for high temperatures (20°C to 450°C), very poor data exists. In [36] ultimate tensile strength are plotted over temperatures, while stress strain curves are given only up to a strain of about 1%. Obviously, for this application, the information was too limited.

As explained by Pereira in 2007 [37] these curves were never measured (or published).

The only information found, for a certain range of strains, during the literature research is from Seidt et al [38]. They provided a good overview of stress strain curves at different temperatures (fig.3.10). However, due to the trend of

the curves and the yield stresses at the different temperatures, a constant doubt on the provided values persisted.

The curves were given in engineering stresses and strains. These needed to be converted to true stresses versus effective plastic strains for this analysis. In fact, Marc requires true stress-strain curves whenever the updated lagrangian procedure is used. With these new curves a complete elastic plastic material model was obtained.
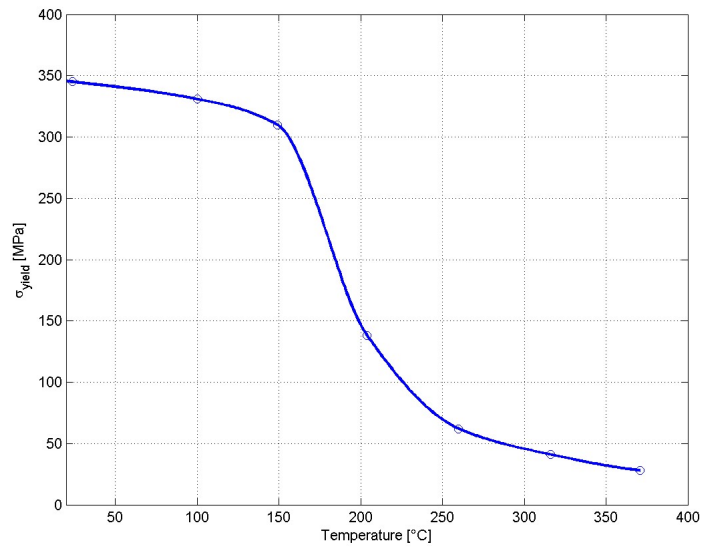
Figure 3.9: yield stress over temperature for Al2024-T3 [34]
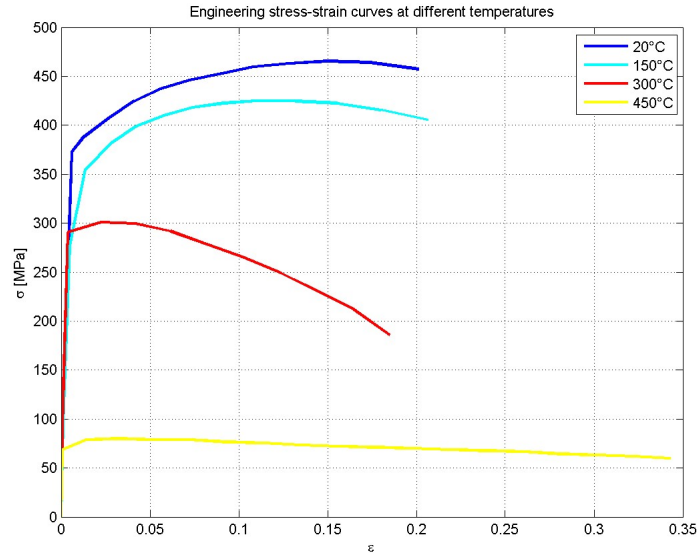
Figure 3.10: Engineering stress-strain curves at different temperatures [38]

Given the engineering stresses σ_{eng} and the engineering strains ε_{eng}, it results immediate to calculate the true stresses σ_{true} and logarithmic plastic strains ε_{ln}^{pl} as follows:

$$\sigma_{true} = \sigma_{eng}(1 + \varepsilon_{eng}) \tag{3.13}$$

$$\varepsilon_{ln}^{pl} = ln(1 + \varepsilon_{eng}) - \frac{\sigma_{true}}{E} \tag{3.14}$$

where E is the Young's modulus.

This results in obtaining the new curves plotted in fig. 3.11 . Fig 3.12 shows the same information plotted in three dimensions.
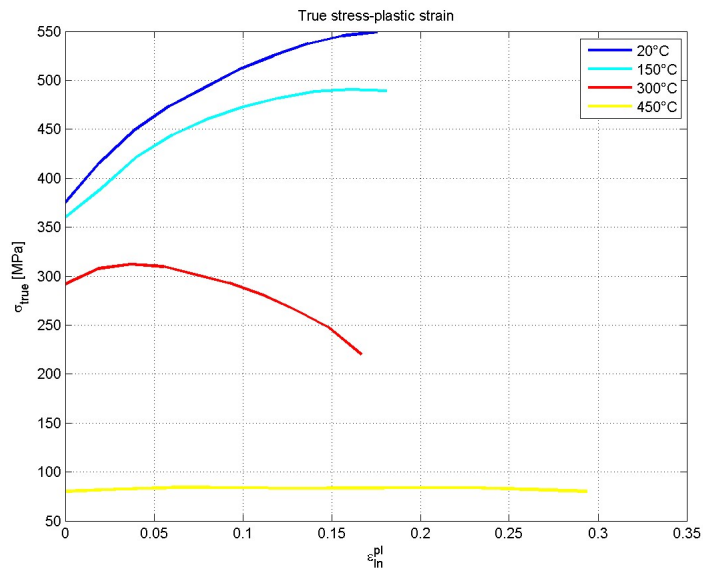
Figure 3.11: True stress-strain curves at different temperatures
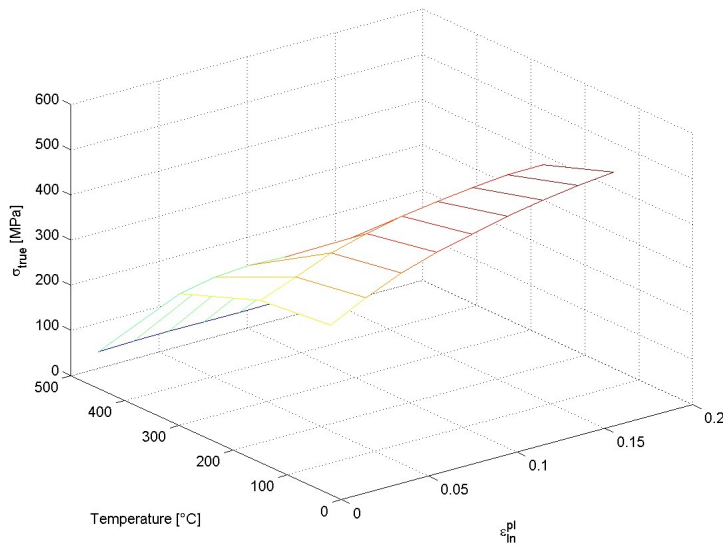
Figure 3.12: True stress 3D plot, over strain and temperature

Once the true stresses versus the effective plastic strain curves were obtained,

it was necessary to implement the values into Mentat. This was done through an external text file and the fields have been compiled as reported in Marc's manual [30].

Thermal conductivity's and specific heat's temperature dependency for Al2024-T3 were taken from the Military Handbook 5 [36]. Points were extracted from the provided graphs through a graph digitizing software tool and the units were converted to S.I. Units.

Plotting the physical properties over the temperature range, the following graphs were obtained:

(a) Thermal conductivity

(b) Coefficient of thermal expansion

(c) Specific heat
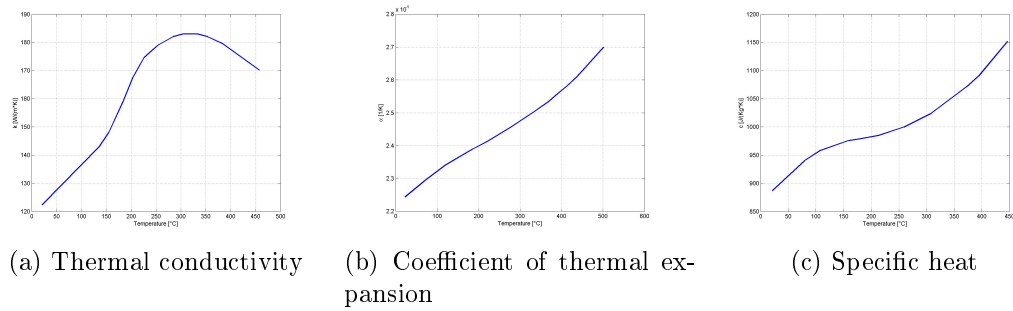
Figure 3.13: Physical properties of Al2024-T3 [36]

As previously mentioned, the stress-strain curves for the different zones will be provided around July 2013. In the meanwhile, dos Santos from the commissioned Research Institute (Helmholtz-Zentrum Geesthacht), provided a report[39] mandated by Airbus. In this research, two different materials (Al2024-T3 and Al6056-T4) were joined using *DeltaN* FSW and subsequently, the material properties were investigated for the different microstructural zones. The stress strain curves were provided for the base materials, the two thermo-mechanical affected zones and the nugget zone. Since in the nugget both alloys were stirred together, this stress-strain curve cannot be used. However, both curves for base material and TMAZ for the Al2024-T3 were introduced in the model. Those were quite different from the curves obtained by Seidt. It became clear that dos Santos' curves for the base material were "more reliable", by comparing the yield stresses over temperature with those reported in [36]. Therefore, dos Santos' curves were implemented into the model through an external text file, as done before.

For all these curves, the engineering stresses and strains, were converted

to true stresses and effective plastic strains through eq. (3.13) and (3.14), as reported in fig. 3.15 and 3.16.
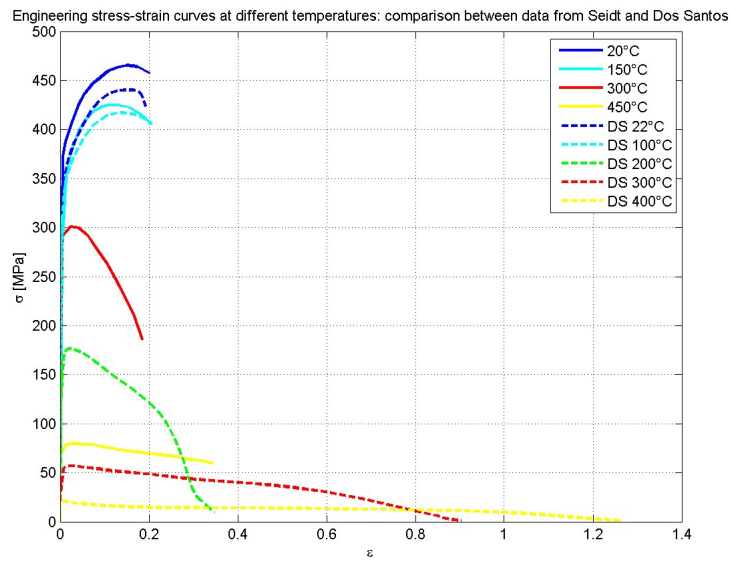
Figure 3.14: Comparison between stress strain curves obtained by Seidt (continuous lines) and by dos Santos(dashed lines; in the legend DS stands for dos Santos) for Al2024-T3 base material
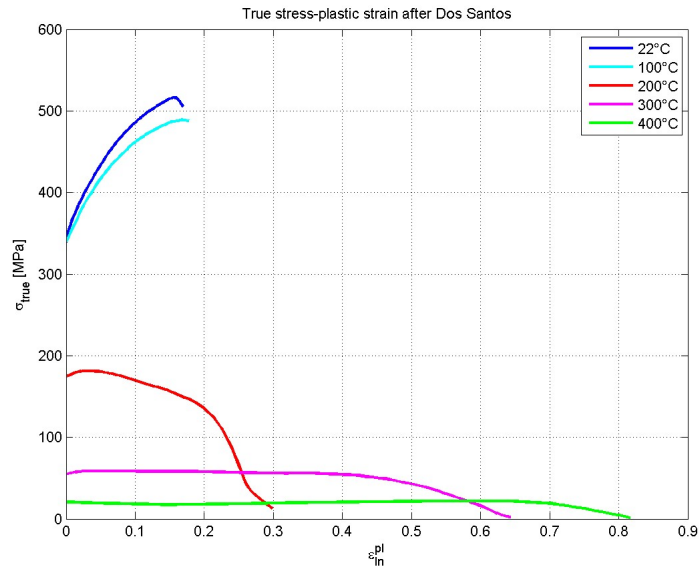
Figure 3.15: True stress-strain curves for Al2024-T3 base material [39]
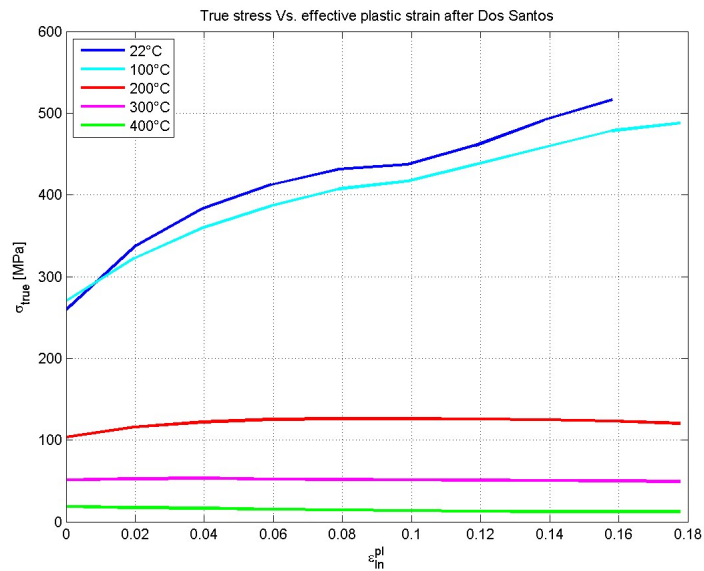
Figure 3.16: True stress-strain curves for Al2024-T3 TMAZ [39]

3.7   Energy Balance

In this section, an attempt to define the whole process is made. A stationary condition is considered, therefore the concepts of power and energies will be used interchangeably[5]. One of the main necessities was to understand (and later quantify) all the energies involved. Looking at fig. 3.17, it can be seen that the whole energy chain is quite complex, with lots of unknowns. In fact, at the beginning of this work, none of these energies were defined, and there was absolutely no idea on the thermal input to the workpiece.
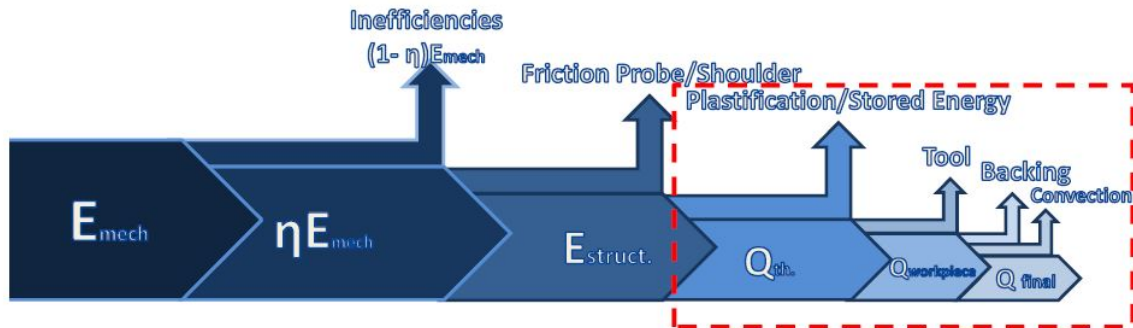
Figure 3.17: Energy chain of *DeltaN* FSW process

The energy chain displayed starts with the mechanical power provided by the robot's electrical motor, which can be calculated through eq. (3.16) once the amperage i and the voltage ΔV provided to the motor are measured and the motor's efficiency η_{motor} is known. The second block of this chain is constituted of the power available at the end of the transmission shaft. The corresponding energy is designated as ηE_{mech}. Further downward, in the 3rd block, the actual power provided to the workpiece is defined. This one differs from the previous, due to friction present between the probe and the shoulder. This should ideally not occur, however, friction is present in two ways:

- friction caused by the presence of material between probe and shoulder, which ascends the tool during the welding process

- friction between the probe and shoulder causd by the applied forces

---

[5]E and Q represent the energy and the heat, while P and $\dot{Q}$ represent the power and the heat rate

The latter has been noticed on an unhardened shoulder after a welding test. The probe rubbed against the shoulder, wiping the inner side of it (fig. 3.18).

A very difficult and hard to answer question is what happens inside the tool's shoulder, between the shoulder itself and the probe: during welding, a small part of the ductile material ascends the probe until it deposits itself between the shoulder and the probe. There, it causes friction. A certain torque is required to win the frictional resistance, therefore it should be accounted for as lost energy.

During the initial phase, while the probe is not yet submerged into the material to weld, the shoulder is appreciably heated by this friction. Although at the first stages it is not really clear in which direction the heat flows, it can be assumed without any doubt that almost immediately after the beginning of the welding process, the warmest zone is the weld pool.

Moving downwards, the total heat rate input $\dot{Q}_{th.}$ needs to be calculated. The corresponding energy is displayed as $Q_{th.}$ in the energy chain. At this point it was necessary to understand how much mechanical energy is converted to thermal energy during the stirring process. This was quite difficult, since, very poor information exists on $DeltaN$ FSW, and in this case a comparison with standard FSW is absolutely not reasonable. In literature [40, 41, 42, 43] a coefficient representing the ratio between power converted to heat and total power exists. This coefficient β defines the energy transformed to heat, while the rest is the so-called stored energy of cold work. Its value depends on the materials, the plastic strain and the plastic strain rate. Different papers present very different values for this coefficient, as reported in tab. 3.5.

Table 3.5: Ratio of mechanical energy converted into heat for Al2024 according to different authors

Author	β coefficient
Hodowany [40]	0.3÷1
Mason [41]	0.8÷0.9
Ravichandran [42]	0.4÷1

Macdougall [43] presents a good review of the existing papers, concluding that values of β=0.6÷0.8 are the most commonly used values.

Different papers on FSW numerical simulations report very different choices of the β coefficient. For example, Schmidt [4] used $\beta = 0.9$, while Chao [44] chose two different β coefficients (0.77 and 0.82) for two different simulations.

Although papers report a use of this coefficient for friction stir welding, it is not possible to adopt it, since it should be talked about stored energy of warm work. In this case the stored energy can be neglected [45]. Therefore, β is assumed to be 1: the whole mechanical energy is converted into heat for friction stir welding.

Further down the energy chain, the distribution in the different parts of the testing structure is displayed.

Eq. 3.15 allows to calculate the power $P_{struct.}$ requested during the process:

$$P_{struct.} = 2\pi \frac{\dot{\varphi}}{60} T \qquad (3.15)$$

where $\dot{\varphi}$ is the angular velocity in rotations per minute and T represents the torque expressed in Nm. The angular velocity $\dot{\varphi}$ is chosen by the operators of the robot, based on the "optimal" parameter window, while the torque needs to be measured during the process. Although the power input is a very simple calculation, it was quite difficult to measure the torque, as previously explained.

Since the power provided by the motor was not measured, it is not possible to start from the first block. This led to the use of an "inverse approach": the thermal energy provided to the workpiece is estimated through the correlation of temperatures between tests and simulations.

At the beginning of this work, before the 3rd test campaign, an inverse approach to the creation of this energy chain has been used, since the unknown power input did not allow to use the forward approach. Initially, through simulation a heat rate input of 650W into the workpiece has been estimated. This power allowed to correlate well the maximum temperature in the weld line and the peak temperatures in the different positions, where thermocouples have been applied.

Schmidt [46] states that, for a conventional friction stir welding tool, about 12% of the heat rate is lost into the tool. Due to the impossibility to perform this measurement during this work, the same coefficient has been assumed for $DeltaN$ tool. This knowledge brought to the definition of the first coefficient $\eta_{workpiece}^{global} = 0.88$.

By dividing $\dot{Q}_{th.}$ by β, the mechanical power delivered to the whole test assembly $P_{struct.}$ has been calculated. To further move back to the power source, it was necessary to understand how much power is lost to friction between probe and shoulder.

At this point, adding the lost power due to friction between probe and shoulder to $\dot{Q}_{struct.}$, the real mechanical power input is obtained. As previously ex-

plained, carrying out a measurement of the power lost to friction was not possible. This quantity, needs to be calculated once that the energies ηE_{mech} and $E_{struct.}$ are known.

Taking it a step further, the electrical power input to the motor can be calculated, knowing its voltage and amperage.

Thus the power of the electrical motor is given:

$$P_{motor} = \eta_{motor} \cdot \Delta V \cdot I \qquad (3.16)$$

The relation between E_{motor} and E is simply given by the transmission efficiency η_{trans}.

At this point a good overview of the energies involved in the process is obtained. Some more effort is required to define where $\dot{Q}_{workpiece}$ goes. Some of this heat rate is used to warm up the workpiece, some is transmitted to the backing plate and some of it flows into the clamping device. Finally a small amount of heat is lost to the ambient through convection.

As already seen, in order to define the energy required to simulate the process $(Q_{th.})$ a backward approach has been used. After the introduction of the shoulder and through correlation of temperatures between test results and simulation, a requested power input of 750 W has been chosen.

Assuming $\beta = 1$, for the reasons presented previously, the stored energy is neglected. Therefore, the mechanical energy that goes into the workpiece is defined. In order to validate this estimated value, the torque moments were acquired during the last testing campaign, but as already explained this did not work out well.

A good portion of the energy chain has been defined. In fact, the informations found, are enough to simulate correctly the welding process. However, to completely comprehend the whole ensamble, more investigation is required.

Figure 3.18: Effect of forces applied during FSW on an unhardened shoulder and pin used during testing

These reflections led to considering a combined forward and backward approach. The already presented backward approach allows to define the energy chain up to the input energy $E_{struct.}$, while the forward approach should define ηE_{mech} through the measurement of electrical quantities and estimation of motor and transmission efficiencies. Once these quantities are known, it is immediate to estimate the energy lost due to friction between probe and shoulder, while neglecting the energy converted to heat, which is considered aniway downstream along the energy chain.

3.8   Validation of Model

3.8.1   Investigation of Interpolation and Extrapolation by MSC Marc

Since it was unknwon how Marc interpolates the values for the 3-dimensional stress-strain curves, a very simple cantilever beam of dimensions 10x2x100mm has been modeled with the Al2024-T3 material properties [39] and a fixed displacement of 2 mm has been applied at one end, while the other end was perfectly clamped. This resulted in a strain $\epsilon = 0.02$. Different simulations were run, for the different temperatures evaluated (tab. 3.6), by simply setting the temperature as initial condition for the whole model. The expected stresses have been extracted from the provided curves, while for the temperatures of 100°C and 200°C a linear interpolation between the existing curves has been applied. For 600°C no estimation of expected stress could be made. It has been investigated which values Marc takes if the points are outside the defined range. In Marc's documentation [30] it is reported that the software extracts the values it needs through interpolation, but it is not explained which kind of interpolation is assumed. The documentation also reports that Marc either extrapolates or takes the last available value for the out of range points. Unfortunately, it is not specified which technique is applied in which case. This very simple example allowed to understand what Marc does.

Medium stresses were evaluated looking at the post file, with attention at looking at the stresses sufficiently far away from the constrains, to neglect the effects of boundary conditions.

Stresses at 100°C and 200°C were linearly interpolated, while the other expected stresses are all given to Marc through the stress-strain curves. For 600°C it was not clear whether Marc would extrapolate the value or take the last provided value, therefore no expected stress is here provided.

By evaluating the stresses at different temperatures, it became clear that MSC Marc linearly interpolates, whenever no data is defined, and it takes the last value whenever we get out of range of the provided data, as demonstrated in tab. 3.6.
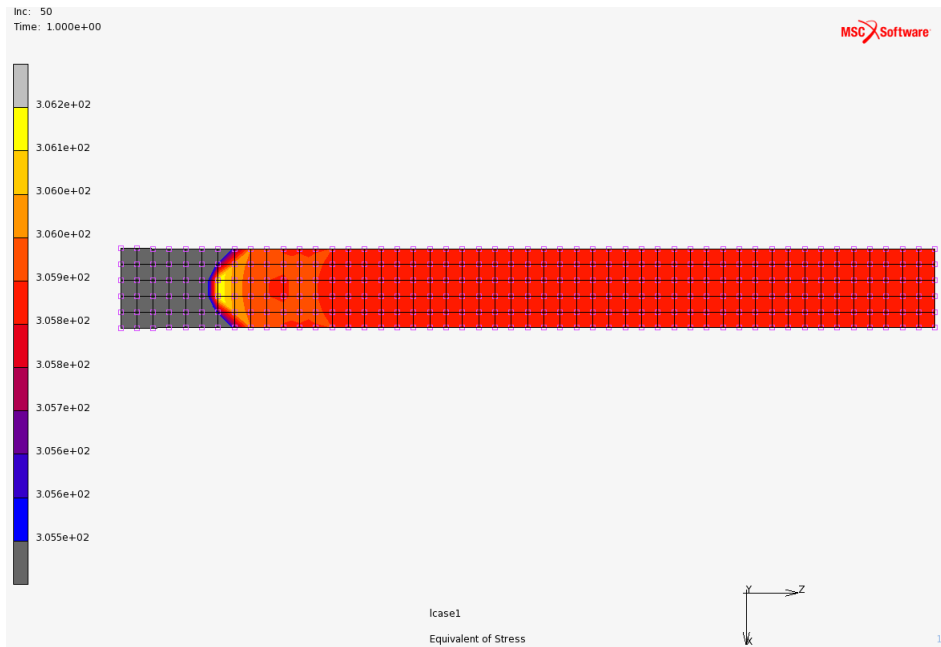
Figure 3.19: Cantilever beam at 300°C and under strain of $\epsilon = 0.02$

Table 3.6: Expected versus calculated stresses for a simple cantilever beam at different temperatures

Temperature [°C]	expected stress [MPa]	calculated stress [MPa]
100	391.3752	392
150	381	382
200	356.27	356
300	305.64	306
450	81.58	81
600	-	81

3.9 Correlation of Thermal Aspects - Temperature Distribution

To correlate the data retrieved from testing, with the simulated temperature distribution, the nodes corresponding to the thermocouple's locations need to be identified. Since the results of the numerical simulation are fully symmetrical,

only on one side have been considered. In the FE model, no node corresponds to the exact position of a thermocouple. For all 8 TC's positions, a linear interpolation between the nodes has been used to calculate the temperature. As explained in the previous chapter, the thermocouples are placed in a hole, at mid thickness of the work piece. Of course, the imprecision in the vertical positioning of the thermocouples could have a devastating effect on the correlation of results. However, due to the small thickness, this problem did not influence the results.

Since no nodes are available in the mid-thickness region of the workpiece, it could be thought that the regions should be remodelled for a better correlation. However, it has been investigated whether a refinement was really necessary, coming to the conclusion that it is not:

As can be seen in fig. 3.20, a strong temperature gradient over thickness is present only in the weld-pool zone, while for the regions immediately next to it, it becomes continuously smaller. The same conclusion has been found to be correct for the regions immediately behind the torch. Therefore, it seems legit to consider only the nodes on the surface.
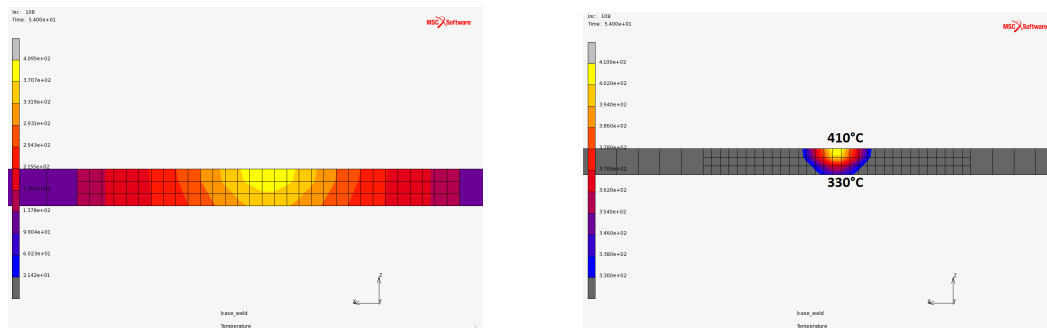
(a) Temperature distribution over thickness of center zone

(b) Detail of temperature gradient in the weld pool

Figure 3.20: Section of current torch position

(a) Temperature distribution over thickness of center zone

(b) Detail of temperature gradient along the weld path
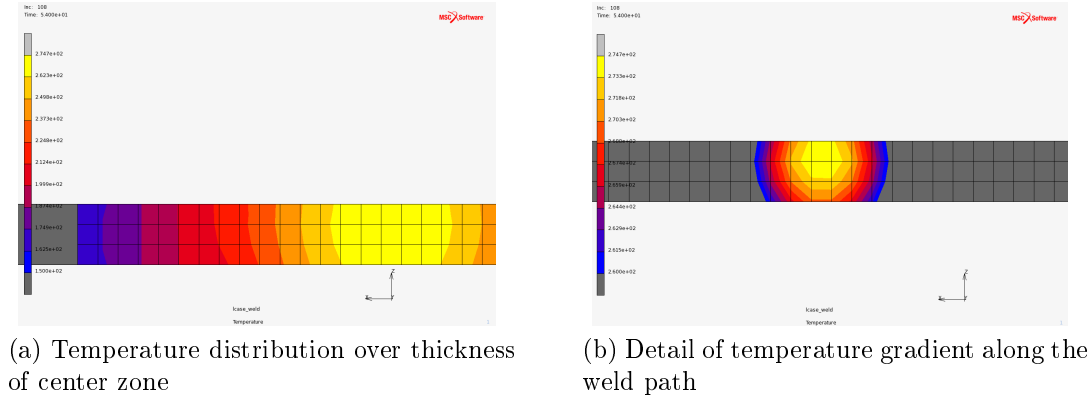
Figure 3.21: Section 5mm behind the current torch position

3.10 Energy Loss Investigation

Different simulations were performed to estimate the energy loss through convection and to see its importance on the energy balance. First, a simulation was run as reference, in which no convection was present. Three different simulations followed with different thermal convection coefficients. In all simulations, all free surfaces were supposed to be exposed to convection. The environment temperature is set to 20°C for all simulations. Simulations ran with face film coefficients of $5 \frac{W}{m^2 K}$, $3 \frac{W}{m^2 K}$ and $0.568 \frac{W}{m^2 K}$. The first represents the lowest value for a natural convection coefficient (in general $h_{c_{natural}} = 5 \div 20 \frac{W}{m^2 K}$ [47]). The second value represents an estimation of the insulated test structure as calculated in section 2.5.4. The last value of $0.568 \frac{W}{m^2 K}$ has been obtained through a simple calculation: it has been found that a polystyrene board presents a thermal resistance of $0.88 \frac{m^2 K}{W \cdot in}$ [48]. Since the board used during the 3rd campaign is 50mm thick (~ 2 in), the corresponding convection coefficient is obtained and amounts to $0.568 \frac{W}{m^2 K}$.
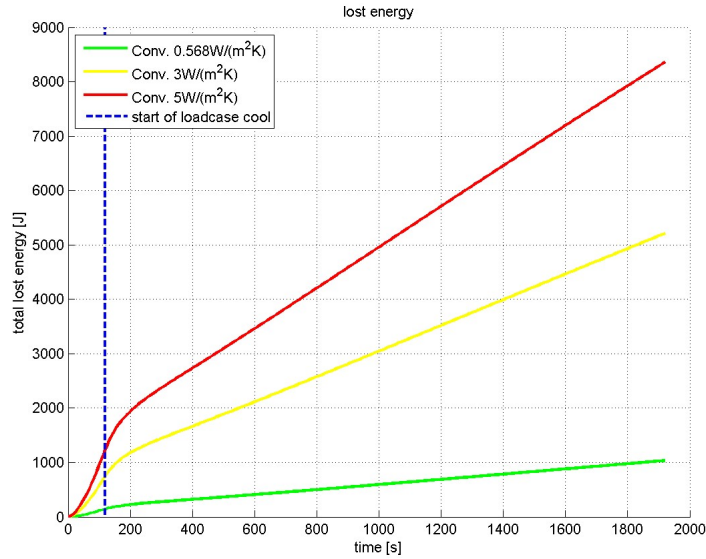
Figure 3.22: Thermal energy lost to convection

With a welding time of 120 s (400 mm of weld length) a total heat input of 51619 J was recorded. The cooling time was set to $1800\,\mathrm{s}(= 30\,\mathrm{min})$. Considering the thermal energy at the end of the cooling period, the following results can be displayed:

Table 3.7: Thermal convection coefficient and corresponding energy

h_c $[\frac{W}{m^2K}]$	Energy lost [W]	Energy lost in percentage of the total energy input [%]
0.568	1035	2
3	5212	10.1
5	8357	16.2

For a well insulated test structure, the convection could be considered approximately zero and therefore neglected during the estimation of the energy balance, however, for the insulation method used, and basing the results on the energy loss estimated through experimentaion, it becomes clear that this amount cannot be simply neglected.

Furthermore, it should be noticed that the energy loss estimatated through experimentation has been approximately reproduced in simulation with the co-

efficient of $3 \frac{W}{m^2 K}$: 4245 J for the tests compared to 5212 J from simulation. Based on the total heat input from simulation, an error of less than 2% is made.

3.11 Parametrical Investigation - Sensitivities

An important part of this thesis was to gain a certain knowledge on FSW and its parameters. Their influence on temperature distribution and therefore on distortions is being investigated.

A parametrical study was conducted, changing only one parameter (in some cases a few) for each new simulation run and trying to see its (their) influence on results. Parallel to this investigation, an evolution of the model occured.

Different simulations were run, changing the following characteristics:

- Only thermal analysis (α set to 0)

- No shoulder

- Flat shoulder

- reduced depth of heat source

- Thermal conductance study: heat contact conductance coefficients have been introduced and changed extensively

- Influence of different stress strain curves for different temperatures (Seidt and dos Santos - BM&TMAZ)

- Introduction of CTE for the Ti interstitial plate

- Change in power input and weld pool

- Change of mesh in Ti plate

- Changed conductivity of workpiece (raised the whole curve by 60 $\frac{W}{mK}$ which is about 50% more than the initial value of the conductivity at 20°C)

All the listed parameters influence results in a stronger or slighter way. The major problem is that two single parameters cannot be introduced to hope to obtain an overlaying effect of the results obtained during separate sensitivity study, since there is always a strong interaction between the parameters.

Different models were created. A list of the created models and the applied changes is displayed:

- Ref 1 : this first model simply consists of the first complete model

- Ref 1.2 : inserted new base material properties after dos Santos

- Ref 2: removed shoulder

- Ref 3: flat shoulder sliding across the coupon's surface

- Ref 4: reduced depth of heat source from the original 2.8mm to 0.5mm. With 0.1mm no heating was achieved; dt=0.25 has been used to prevent crash of analysis due inside out elements

- Ref 5: Heat contact conductance is set between workpiece and shoulder with a coefficient of $h_c = 600 \frac{W}{m^2 K}$

- Ref 5.2: Heat contact conductance coefficient is set to $h_c = 600 \frac{W}{m^2 K}$ between the inner contact bodies (filler&cbody_f) and the Ti plate

- Ref 6: Same as Ref 2, but only thermal analysis (set $\alpha = 0$)

For all following models, the weld length was set to 360 mm, reproducing the real weld length:

- Ref 7.2: dos Santos's base material properties were applied

- Ref 7.3: added dos Santos's TMAZ material properties for the inner zone (filler&cbody_f)

- Ref 8: set coefficient of thermal expansion, depending on temperature, for the Ti-plate

- Ref 9: raised power input to $1000W$, set $h_{c_{shoulder}} = 1000 \frac{W}{m^2 K}$, added new conductivity and specific heat for the shoulder (both depending on temperature)

For all following models, the new backing plate has been inserted; the shoulder's material properties inserted in the Ref 9 model were kept, as well as the true weld length:

- Ref 10: $P_{in} = 650W$, $h_{c_{shoulder}} = 5000 \frac{W}{m^2 K}$

- Ref 10.2: $h_{c_{inner-bodies}} = 3000 \frac{W}{m^2 K}$, $h_{c_{shoulder}} = 10000 \frac{W}{m^2 K}$, $h_{c_{rest}} = 300 \frac{W}{m^2 K}$

- Ref 10.3: $h_{c_{inner-bodies}} = 3000 \frac{W}{m^2 K}$, $h_{c_{shoulder}} = 10000 \frac{W}{m^2 K}$, $h_{c_{rest}} = 600 \frac{W}{m^2 K}$

- Ref 10.4: $h_{c_{inner-bodies}} = 10000 \frac{W}{m^2 K}$, $h_{c_{shoulder}} = 100000 \frac{W}{m^2 K}$, $h_{c_{clamps}} = 10 \frac{W}{m^2 K}$, $h_{c_{rest}} = 300 \frac{W}{m^2 K}$

- Ref 10.4 mod k: raised the whole work piece material's thermal conductivity curve by $60 \frac{W}{mK}$ ($+50\%$ on the value at room temperature)

- Ref 10.5: simulating the through-experimentation evaluated real power input: $P_{in} = 692W (= 612W/0.8825)$
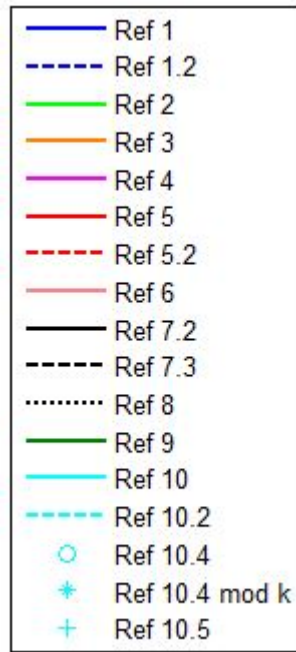
Figure 3.23: Legend for the following plots, containing a comparison between the different sensitivites' study

Results

This parametrical study led to a better understanding of the process, its parameters and their influence. For example, it has been experienced that an asymmetrical heat input (Ref. 4) or a much higher power input (Ref. 9) did not lead to a significant raise in terms of distortions.

During this parametrical study, it became clear that thermal results and distortions need to be treated separately. It was thought that a good correlation of temperature distribution would lead to a correct simulation of distortions. Although a good thermal correlation for some positions has been obtained, reasonable distortions were not found: in fact, all distortions are at least wrong by a factor of 10.

This investigation is primarily aimed at the study of the trends, caused by the change of important parameters, but the acquired knowledge and the evolution of this study helped to set the parameters for a good correlation of thermal results.

In the following graphs, the temperature curves have been considered at the different TC's positions for convenience.
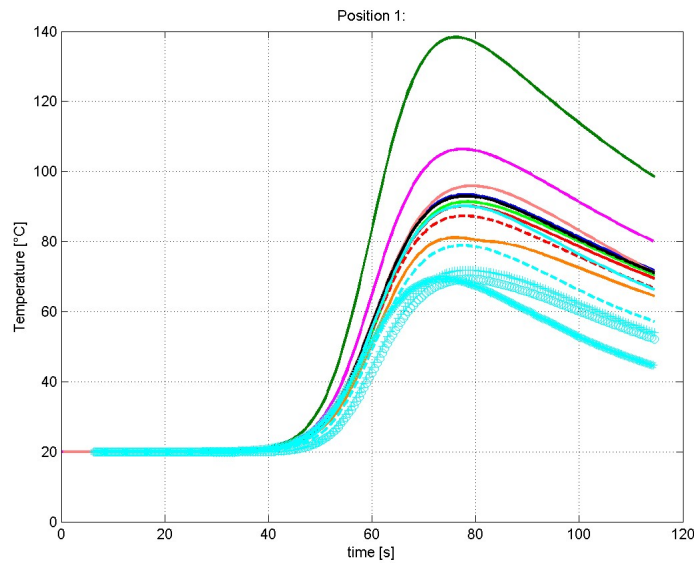
Figure 3.24: Temperatures over time for the different parametrical-models
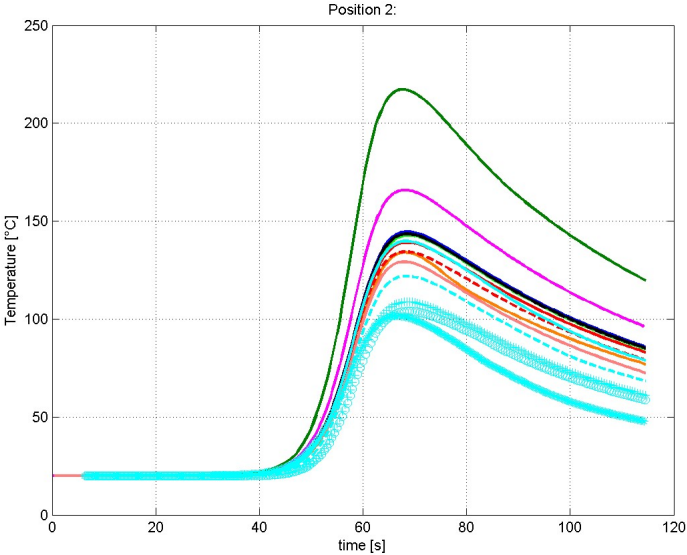
Figure 3.25: Temperatures over time for the different parametrical-models
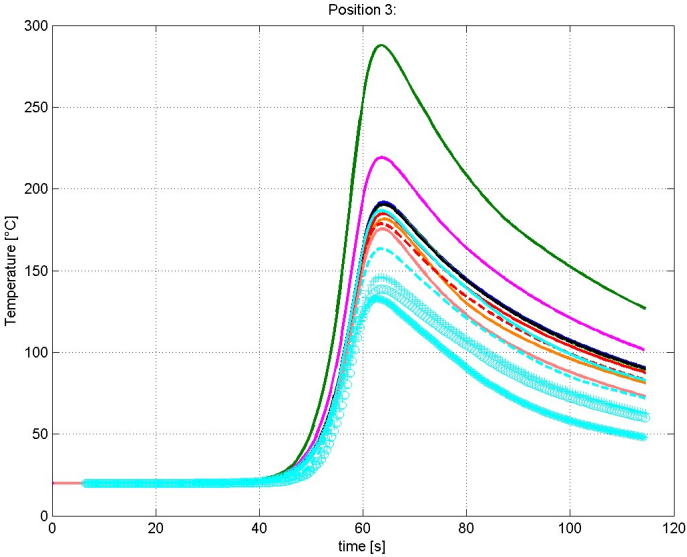
Figure 3.26: Temperatures over time for the different parametrical-models
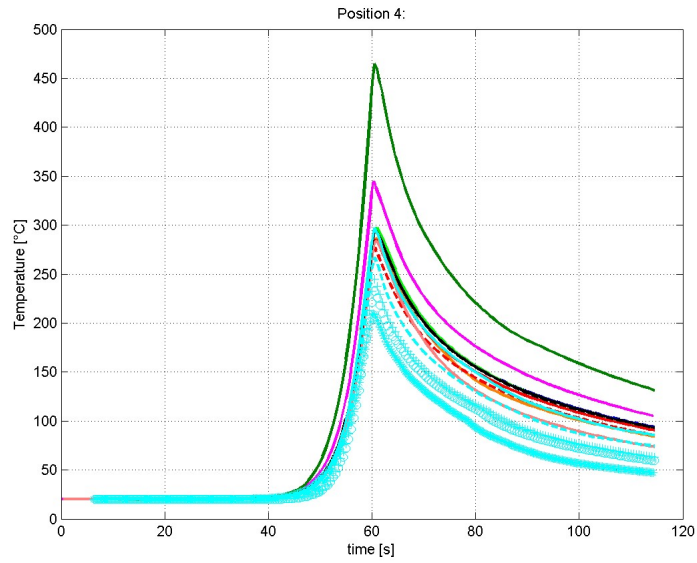
Figure 3.27: Temperatures over time for the different parametrical-models
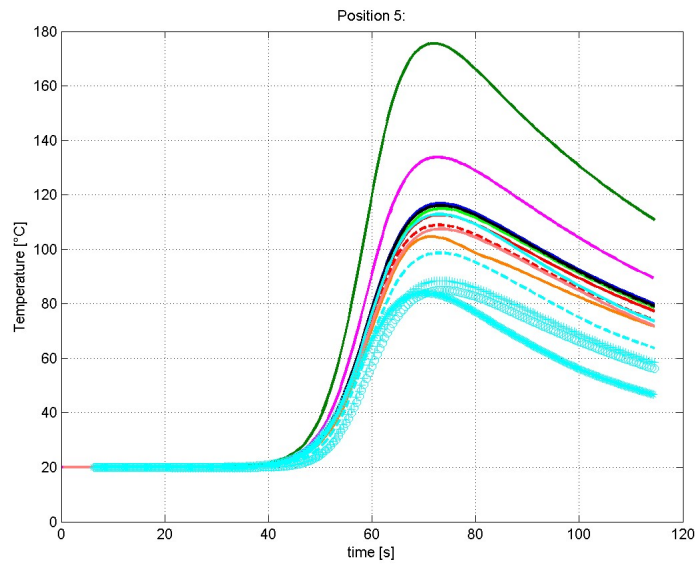
Figure 3.28: Temperatures over time for the different parametrical-models
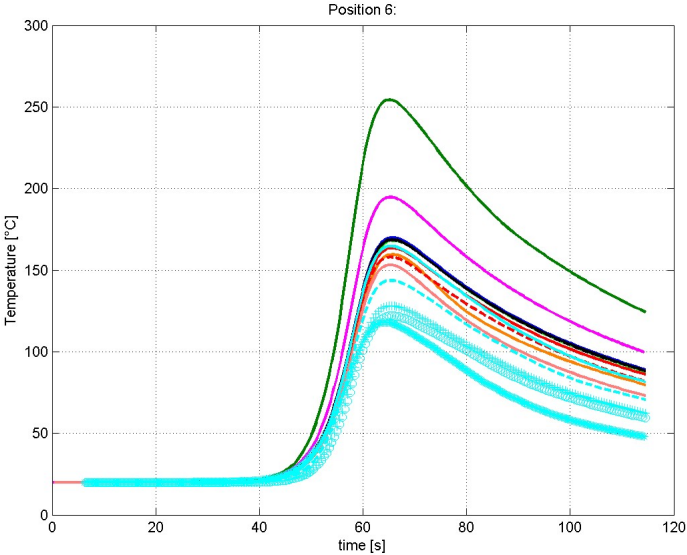
Figure 3.29: Temperatures over time for the different parametrical-models
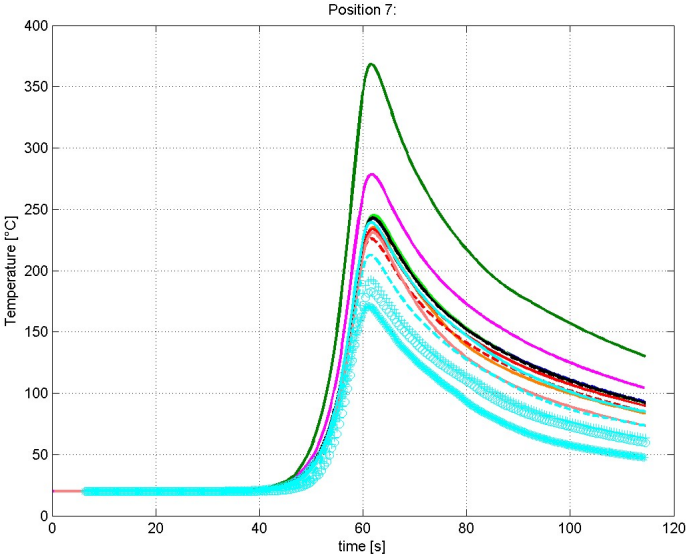
Figure 3.30: Temperatures over time for the different parametrical-models
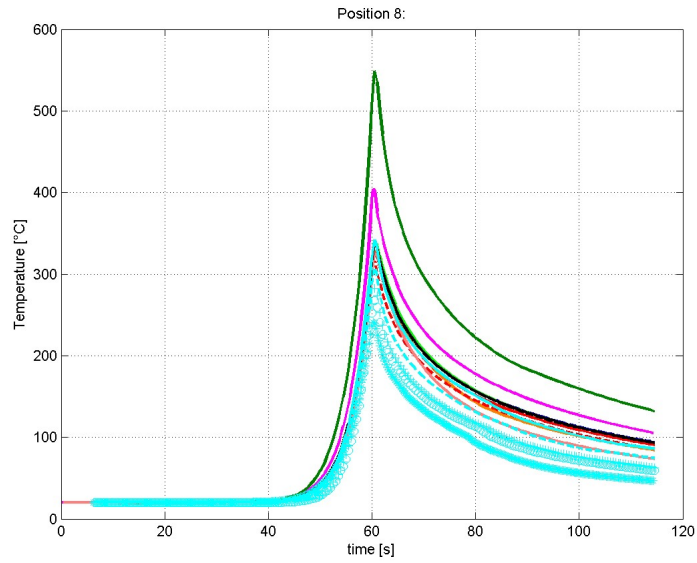
Figure 3.31: Temperatures over time for the different parametrical-models
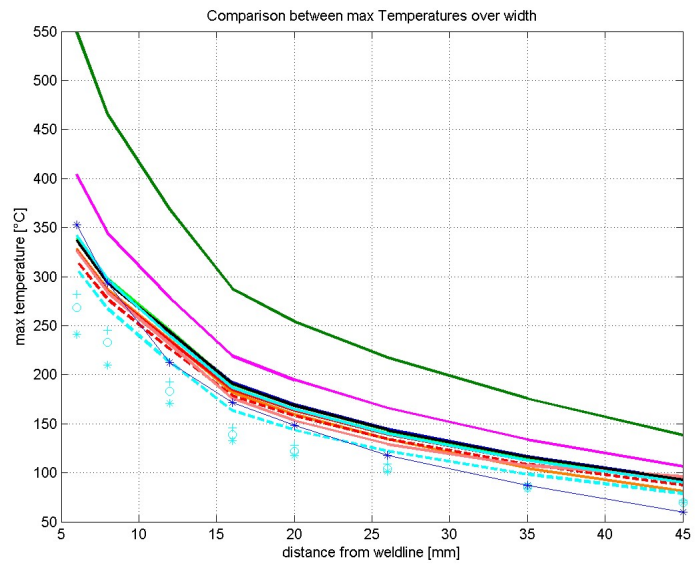
Figure 3.32: Temperatures over the coupon's half width
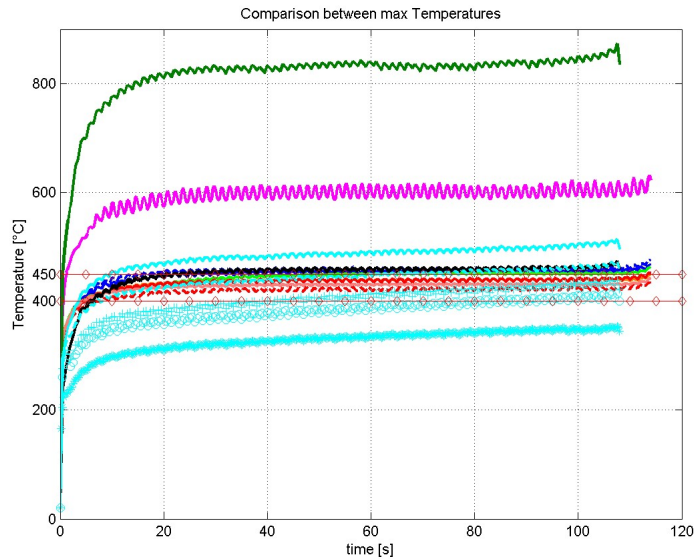
Figure 3.33: Maximum temperature registered in the model over time

Thermal Considerations

As expected, no difference in temperature distribution can be seen between models Ref 1, 1.2 and 2.

The use of a flat shoulder, sliding across the original surface of the workpiece, in general, reduces the max temperature and significantly accelerates the cooling curves: they result steeper.

By setting contact conductance coefficients and keeping the same power input (Ref 5 & 5.2), maximum reached temperatures are lowered and the distribution changed. In these two models, a decent correlation of results is obtained for the positions closest to the weld line (pos. 8, 4, 7, and 3), while still too high temperatures are obtained for the 4 outer positions. No apparent change has been obtained on the cooling curves steepness.

Models Ref 7.2, 7.3 and 8 present no difference to the temperature curves of model Ref 1.

Due to a higher power input in Ref 9, the maximum peaks were raised significantly. The cooling curves major steepness is attributed to the increase in temperature, due to the dissipation's inverse dependence on temperature. The increased thermal contact coefficient between workpiece and shoulder, is accounted only for a reduction of global temperature, while no influence on the

curves' trends can be directly attributed to it.

The models, in which the backing plate's size has been redimensioned (Ref 10), were thought to study the temperature distribution in the workpiece and in the shoulder. It has been noticed that Ref 10.2 allows to correlate well peak temperatures for the central positions (3, 4, 6 and 7). Results of model Ref 10.4 display a good maximum reached temperature value for the shoulder (210°C), however due to the heat flowing into the shoulder and due to the other high contact conductance coefficients, the maximum reached temperature in the weld pool results too low. This leads to thinking that the input power needs to be raised, to get correct maximum temperatures.

Since apparently not much has been achieved through the setting of different thermal contact conductance coefficients, a first thought was that the temperature gradient depends primarily on the material's thermal conductivity. Therefore, the whole thermal conductivity curve of Al2024-T3 was traslated upwards by $60\frac{W}{m^2K}$, which corresponds to a rise of about 50% of the conductivity at room temperature. For this case, the curves next to the welding line present only a reduced maximum peak, while those further away change shape. The maximum temperature is reached quicker for all positions. For the inner positions the shape of the curves and the peak values are unchanged. However, for the positions far from the weld line the cooling curves fall much quicker than the previous ones. This is actually a good discovery (although expected).

Considerations on Distortions   The distortion obtained from the simulations (after releasing the workpiece), do not correspond to reality. A simple look at the deformed test-coupons makes it obvious that simulated deformation is way too low. In fact, an out-of-plane displacement of 1 to 2 millimeters is clearly visible on the tested samples, while numerical results show out-of-plane displacements of the magnitude of 10^{-2} mm. A difference of two orders of magnitude is too high for a correlation of results. However, the shape of the deformations looks the same as the one from the tested samples (fig. 3.34).
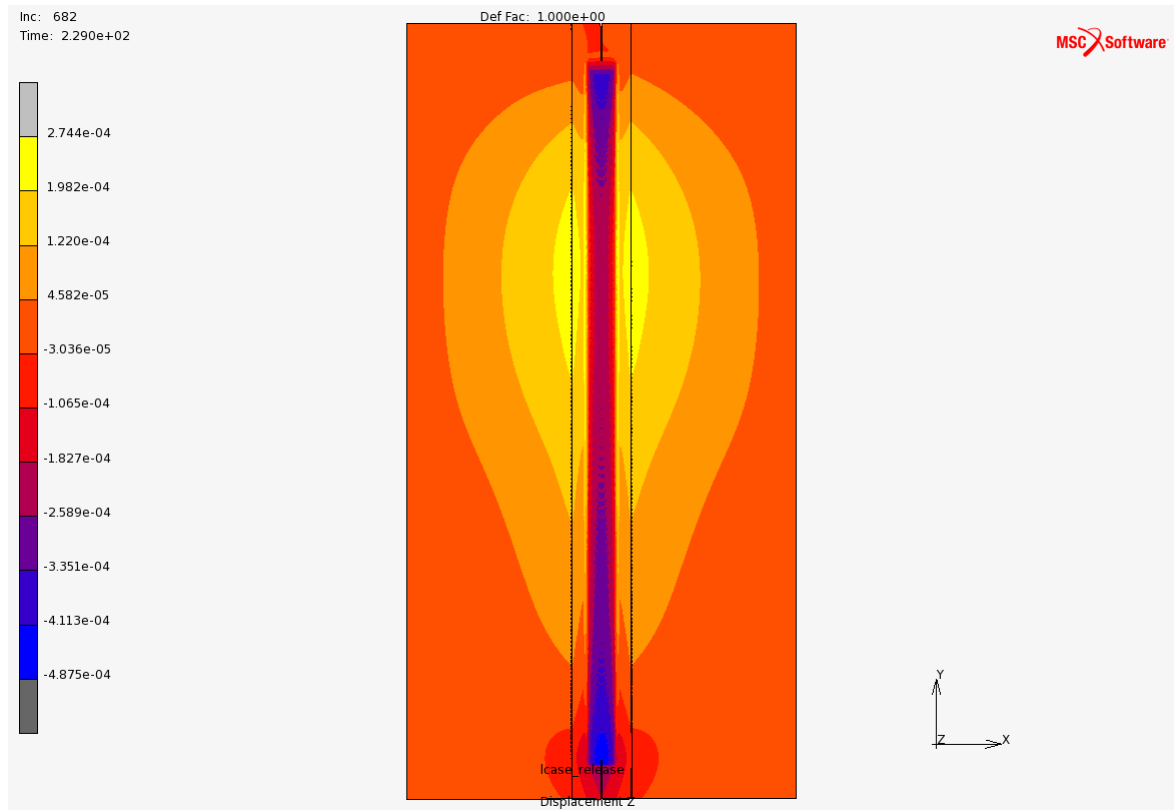
(a) top-view
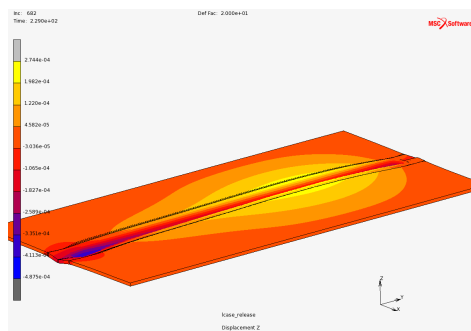
(b)
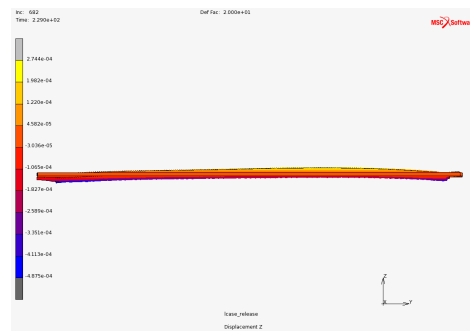
(c) right-side view

Figure 3.34: Out-of-plane (z) displacement of the workpiece at the end of load-case release

This helped to understand and define the parameters to set, in order to obtain

the "final" model which correlates well with test results and will be presented later.

Mesh of Ti-6Al-4V Interstitial Plate

One of the parametrical studies involved the dependance of the mesh on heat transfer between the work piece and the titanium plate. In order to check whether there is any influence of the mesh, two separate thermal analyses ($\alpha = 0$) were launched. The first, was simply the standard definition of the model (920 Hex8 of 10x10x2mm size), while in the second, the mesh of Ti-plate has been refined in the central zone (total of 24800 Hex8 elements of 10x10x2mm and 1x1x1mm size). Since the analyses were only thermal, the significant increase of elements in the model did not lead to excessive calculation time. As can be seen in the figures 3.36 and 3.35, no significant change was recorded. Therefore, the original mesh has been used for all models.
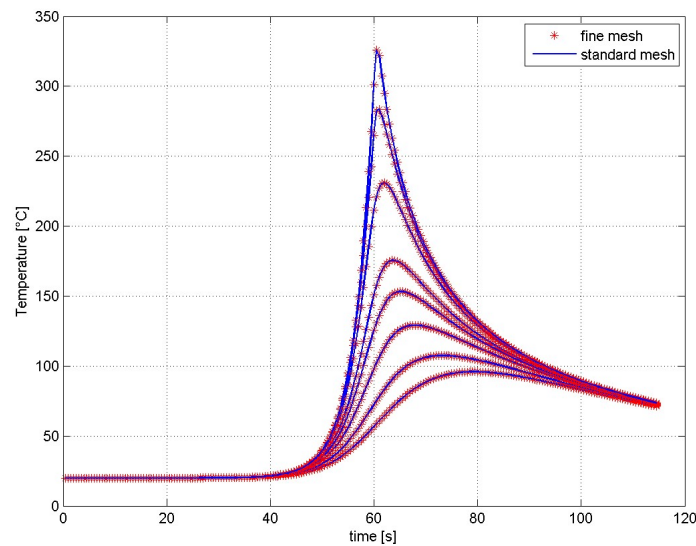
Figure 3.35: Temperatures over time for the different TC's positions for both configurations (standard and refined mesh)
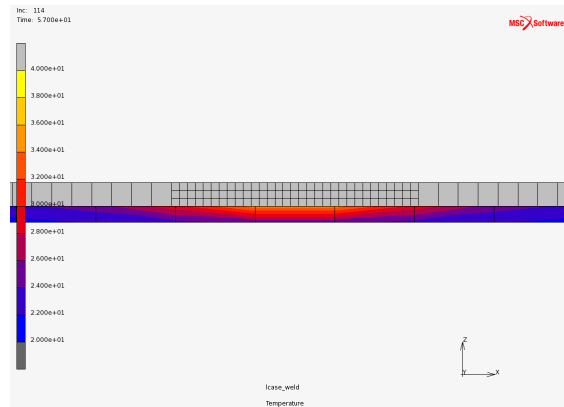
(a) Original mesh
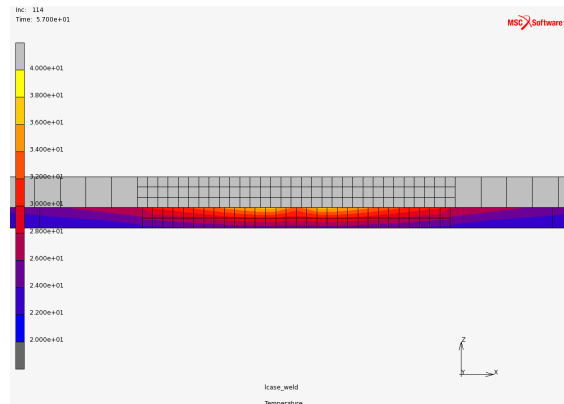
(b) Refined mesh

Figure 3.36: Detail of temperature distribution in the Ti-6Al-4V plate. The images represent the cross section ($y = 200mm$) of the coupons, cutting through the middle of the heat source.

3.12 Analysis Time

The reduction of calculation time (or wall time) was one of the main objectives, once it was clear how costly in terms of computation these simulations were. With the development of the model, in terms of mesh refinement, new contact bodies and new parts, the calculation time in terms of real time (or wall time) has risen continuosly, from the initial 20 minutes for an analysis with only the workpiece to over 1 week for the final model. This was clearly not acceptable, and therefore some measures have been taken. First of all, it has been tried

to reduce the number of elements, e.g. splitting the backing into two different meshes. Another big problem was that the huge amount of separations raised the number of cycles, costing a remarkable amount of calculation time. This led to a significant reduction of time, by simply limiting the number of separations for each increment. A good value of allowed separations per increment is 6 [49]. Time was reduced by almost 50% due to the reductions of cycles per increment. Another important parameter for the contacts is the contact stress threshold. By setting it to 1 MPa, the number of separations was again reduced.

Further improvement of analysis time can be reached through multi-domain processing: it consists of splitting the model in various parts and calculating the different parts separately and then join them on the interfaces. This technique can be very useful, if the interfaces are chosen in a good manner and the contacting parts between domains are not too many. Unfortunately, a specific licence is required for this kind of analysis and therefore it has not been thought, if the multi-domain processing would bring any benefits for this model.

A good way too further reduce the wall time was to use the multi-threading technique. With this set-up it was possible to exploit the server's 2 CPUs, having 4 cores each, to cut down wall time significantly, as reported in tab. 3.8.

Table 3.8: Total simulation time for the final model

total wall time [s]	229899.44 (approx. 2 days 16 h)
total CPU time [s]	633578.18 (approx. 7 days 8 h)

4 Correlation

4.1 Temperatures

For the correlation of results, the experience acquired during this work was of fundamental importance and in particular the performed sensitivity study, allowed to get a feeling about the most important quantities. For the purpose of correlating the results, the peak temperatures, as well as the shape of the curves and the temperature in the shoulder were evaluated. It has been also verified, that the maximum temperature in the model during the welding phase was approximately between 80% and 90% of the material's solidus temperature, which is the range of temperature during friction stir welding, as previously reported. In fact, a slightly higher maximum temperature has been recorded, with the highest ever reached at 470°C. The results are still considered acceptable, since the temperature does not deviate too much from estimations and the solidus temperature of 502°C has never been reached (fig. 4.10).

For a better explanation all curves are considered to be divided in 3 parts: the heating phase, the maximum temperature reached and the cooling phase. It has been noticed that the heating phase correlates well for most of the analyses and for most positions. A substantial difference in terms of maximum reached temperature has been found for the different positions and for the different simulations. In fact, for a single simulation, it could occur that some peaks correlate well, while others completely deviate from the measured values. So, the major goal was to correlate the peaks for all TC's positions.

For the purpose of correlation of results, two different models are here presented: Ref. 10.2 and Ref 10.4.3.

Ref. 10.2 presents decent results in terms of peak temperatures for each position, as reported in tab. 4.1. The only values outside of the minimum and maximum recorded temperature curves are for two positions furthest from the weld line (pos. 5 and pos. 1).

Table 4.1: correlation of temperature peaks

position	distance from weld line [mm]	$T_{Ref.10.2}$ [°C]	$T_{Ref.10.4.3}$ [°C]	T_{max} [°C]	T_{avg} [°C]	T_{min} [°C]
8	6	373	373	374	353	336
4	8	272	267	310	294	271
7	12	221	215	226	213	195
3	16	166	157	193	172	159
6	20	149	141	155	148	141
2	26	123	114	129	118	107
5	35	102	95	100	87	83
1	45	79	73	71	60	50

Cooling curves, instead, do not correlate well at all, since the cooling for simulation seems to be too slow, compared with test results. The only execption is for position 8, where the initial part of the cooling curve is much steeper than the curves from tests. This is attributed to the very high thermal contact conductance coefficient set between shoulder and workpiece. The main reasons for the lack of steepness in curves are the material's conductivity and the thermal contact conductance coefficients. The problem is that both quantities are related to the temperature in the workpiece and to the power input. This results in a very complicated interaction of the different parameters. As seen in the sensitivity study, a rise in conductivity allows to obtain steeper cooling curves, with the disadvantage of shallower heating curves, which would not correspond to reality. By changing the contact conductances, the thermal energy flowing from the workpiece to its adjacent fixture is changed, causing an increase or decrease of temperature and therefore a change in the temperature distribution.

Ref 10.4 instead, did not correlate well at all at first. The maximum temperatures were too low, for each position. However, the need of reaching a high temperature on the shoulder's outer surface (as recorded in the experimental part of this thesis), made it unavoidable to pursue this path. It has been noticed that the thermal contact coefficient between workpiece and distanciation pieces cannot be as low as chosen for Ref. 10.4. Therefore it has been set to $h_{c_{clamps}} = 1000 \frac{W}{m^2 K}$. The thermal contact conductance coefficient between the outer contact bodies of the workpiece and the Ti-plate has also been raised to $1000 \frac{W}{m^2 K}$. A film coefficient of $20 \frac{W}{m^2 K}$ has also been set to reproduce natural convection with an ambient temperature of 20°C. Different simulations were run, raising the power input from the initial 650W. After a careful evaluation of the different power inputs, it has been decided that a power input of 750W (Ref. 10.4.3) seems best suited to obtain a good temperature correlation. Although the discussion made for Ref 10.2 regarding the cooling curves is still correct, the

peak temperatures, as well as the maximum temperatures in the model are all in the expected range, except for position 1. For this position an excess of 2°C, compared to the maximum temperature reached in the same position during tests, has been recorded (unsignificant deviation).

The temperature reached in the shoulder (fig. 4.11) is well approximated to the temperature recorded during testing. The temperature at the end of the loadcase cool is considered, because during the welding loadcase a very strong temperature gradient is present in the shoulder and the instant where the temperature is the highest on the upper part of the shoulder is at the end of the simulation.

Furthermore, the input power of 750W is quite near the estimated requested power input of 692W[6], which further confirms both numerical and experimental results.

Fig. 4.9 shows the maximum registered temperatures for each thermocouple's position over the coupon's width. From the graph it can be apprehended that the registered temperature are in the bandwidth of experimentally measured temperatures. However, it is showing the difference in steepness of cooling between tests and simulation. The major difference can be seen at a distance up to 7.5 mm from the weld line, which corresponds to the shoulder's outer boarder. The very high steepness of the simulation is due to the very high thermal contact conductance coefficient set between workpiece and shoulder and necessary to heat the latter up to the measured temperature range. The difference in steepnesses for the rest of the curve, also not correlating well, is also attributed to the contact conductance coefficients used. However, the difficulty in finding a good balance between power input, contact conductance coefficients for the different parts of the model, and material properties (e.g. conductivity), led to the decision to consider this model as good enough for the purpose of thermal correlation.

---

[6]This value has been calculated from the value obtained from experimentation, as explained in paragraph Total Thermal Energy
: 612.5W were estimated to be required. Considering Marc's efficiency of 88.52%, this results in a power input required for simulating the process of 692W
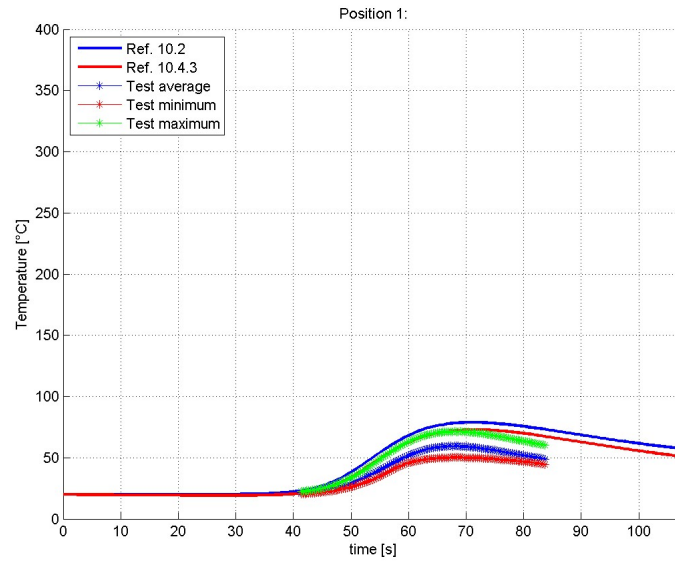
Figure 4.1: Correlation between numerical and test results - Position 1
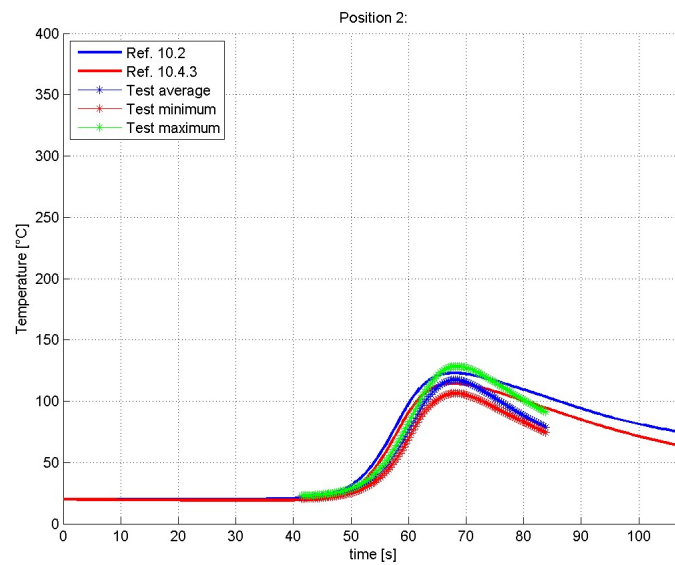
Figure 4.2: Correlation between numerical and test results - Position 2
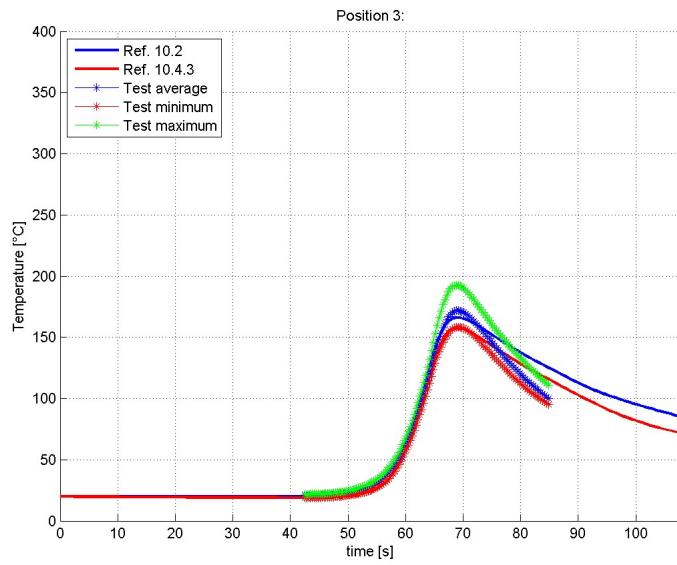
Figure 4.3: Correlation between numerical and test results - Position 3
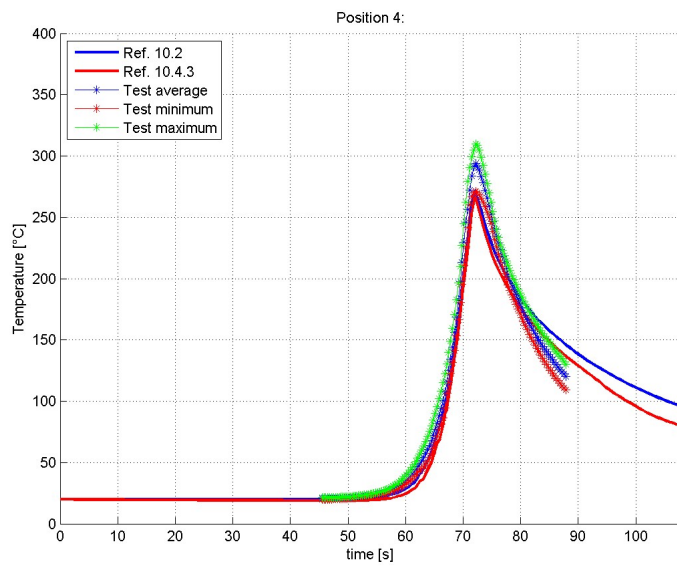
Figure 4.4: Correlation between numerical and test results - Position 4
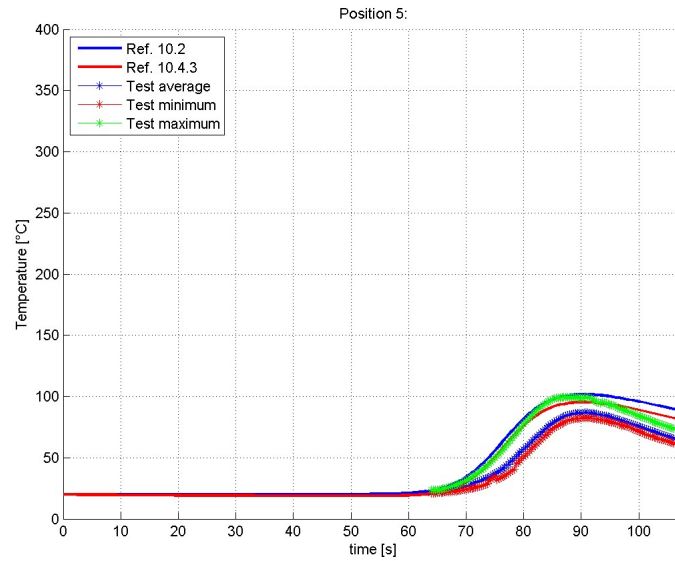
Figure 4.5: Correlation between numerical and test results - Position 5
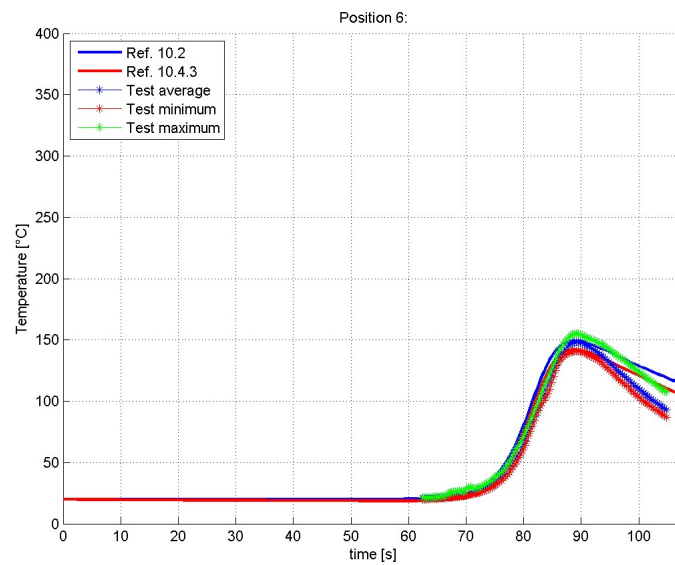
Figure 4.6: Correlation between numerical and test results - Position 6
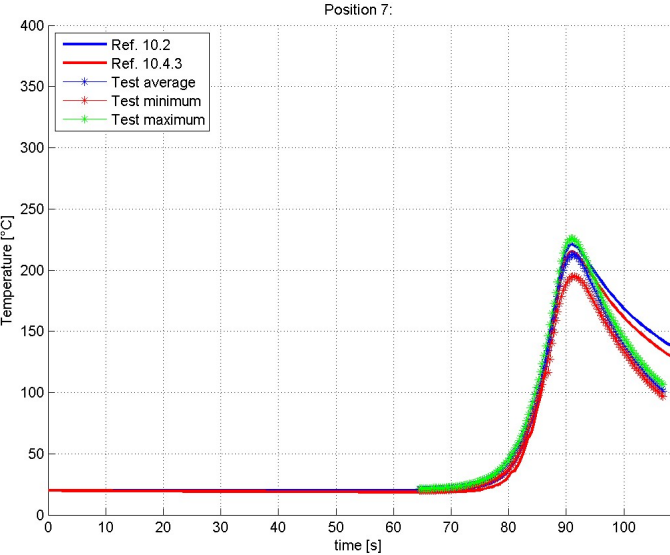
Figure 4.7: Correlation between numerical and test results - Position 7
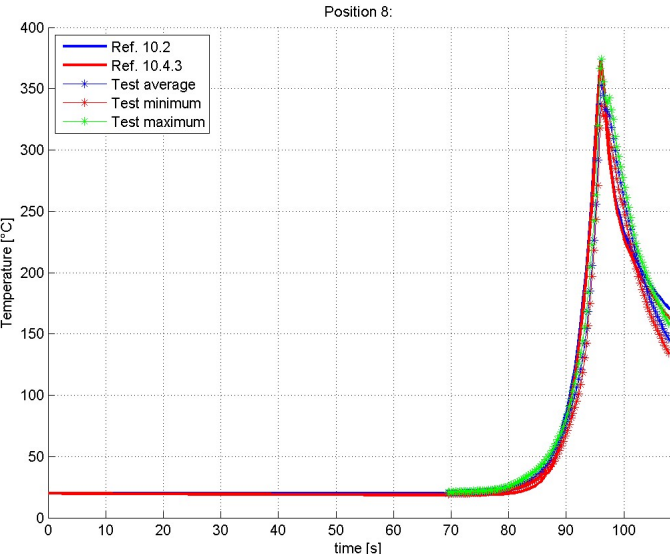
Figure 4.8: Correlation between numerical and test results - Position 8
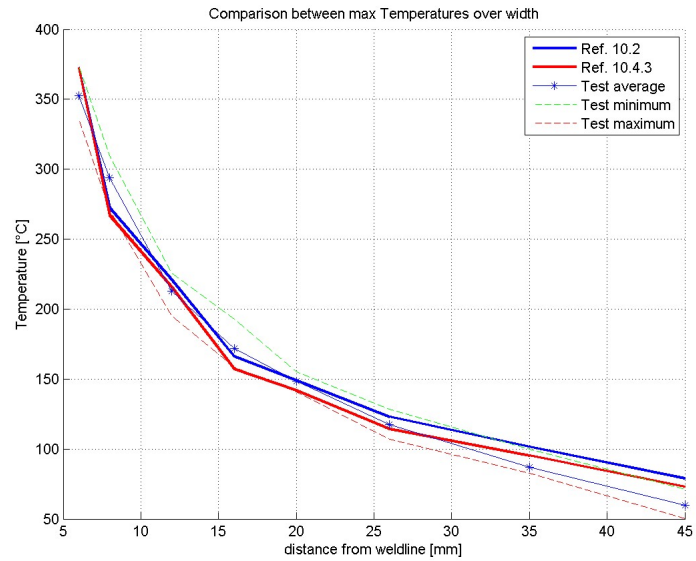
Figure 4.9: Temperatures over the coupon's half width
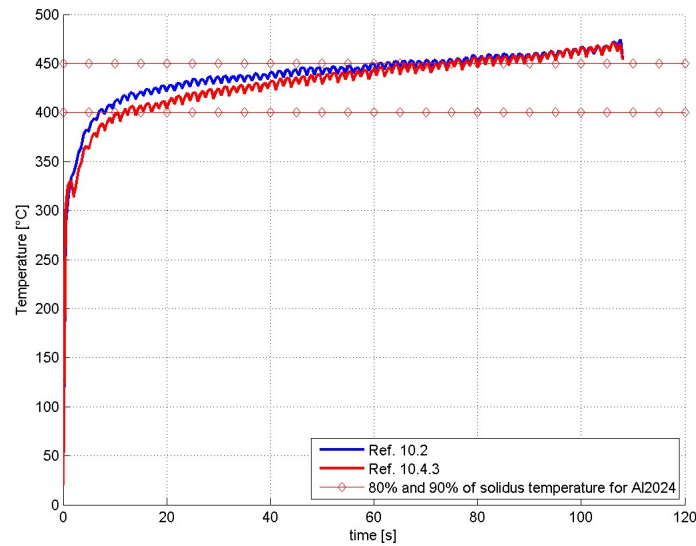
Figure 4.10: Maximum temperatures in the model
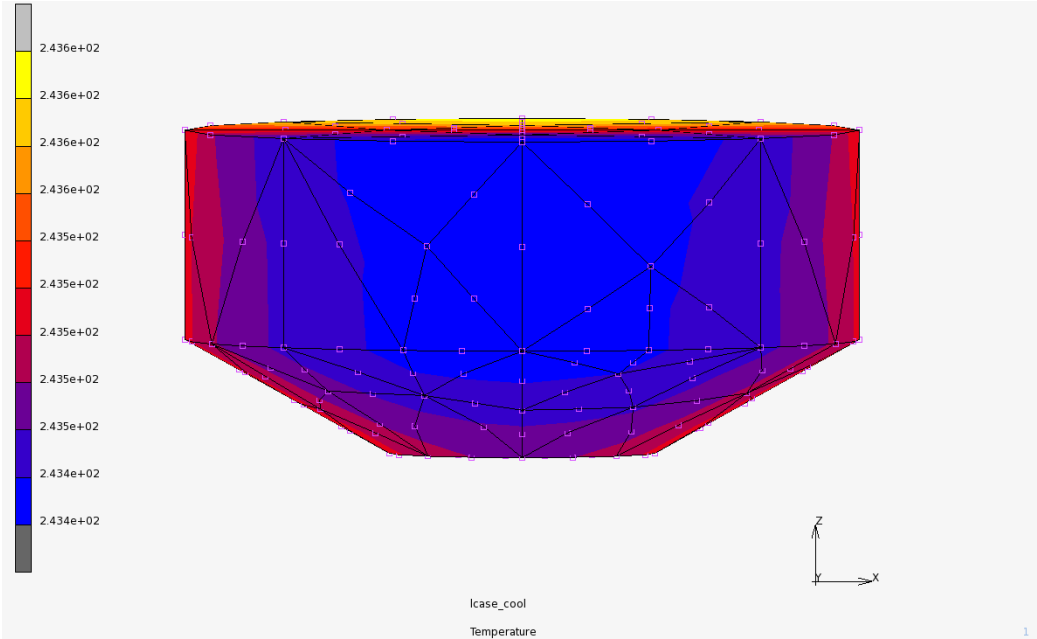
Figure 4.11: Temperature in the shoulder at the end of load case cool

4.2   Residual Stresses

Fig. 4.12 through 4.19 refer to the model Ref. 10.4, in which the traverse stresses σ_{xx} can be seen at different increments. The stresses have been evaluated in the workpiece along a line parallel to the weld path at x=50mm (which is exactly in the middle of the left coupon half).

These plots are presented, because they could be used to investigate the clamping forces required during the whole process.

It can be seen that compressive stresses are travelling with the heat source, while during cooling tensile stresses are present. As soon as the workpiece is released, the residual stresses are approximately zero and they are equilibrated.
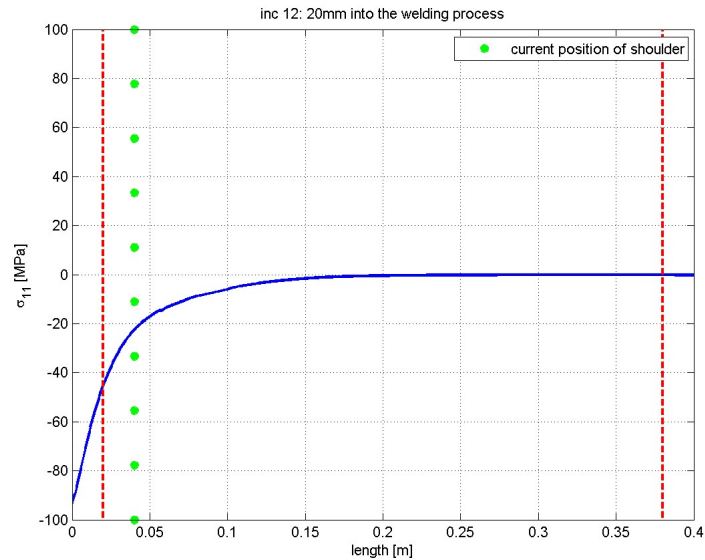
Figure 4.12: 20 mm of performed weld
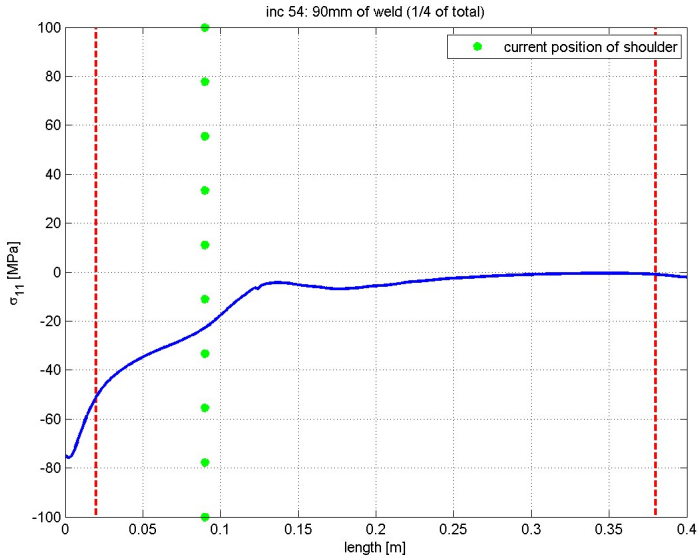
Figure 4.13: 90 mm of performed weld
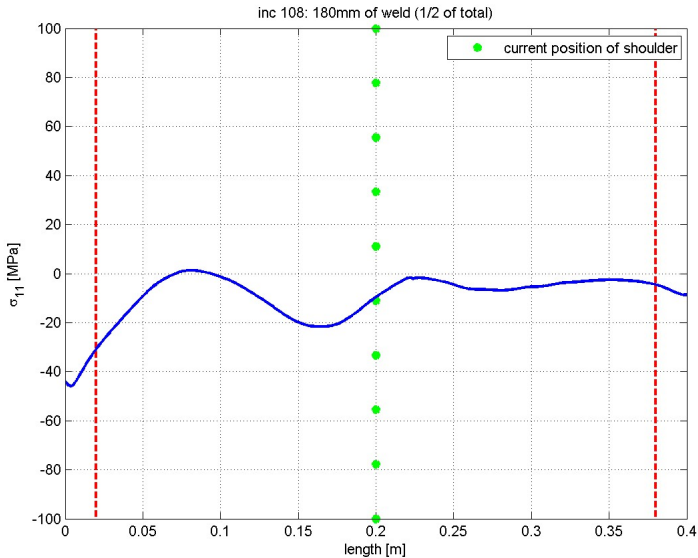
Figure 4.14: 180 mm of performed weld
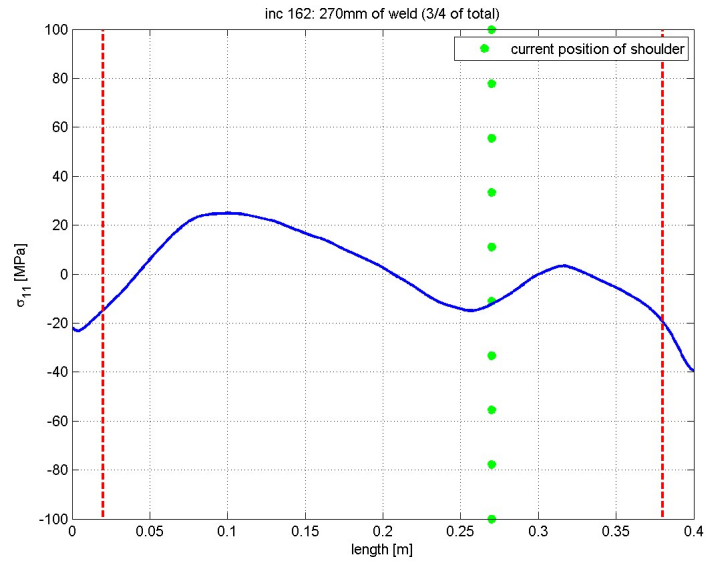
Figure 4.15: 270 mm of performed weld
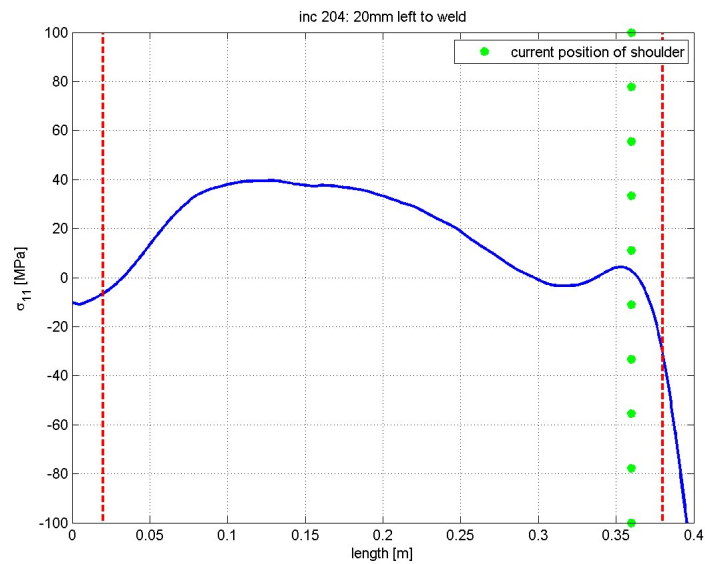
Figure 4.16: 340 mm of performed weld
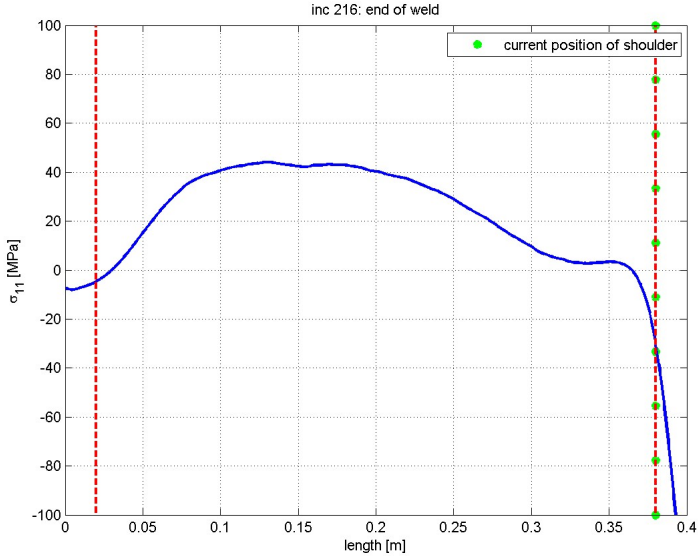
Figure 4.17: 360 mm of performed weld
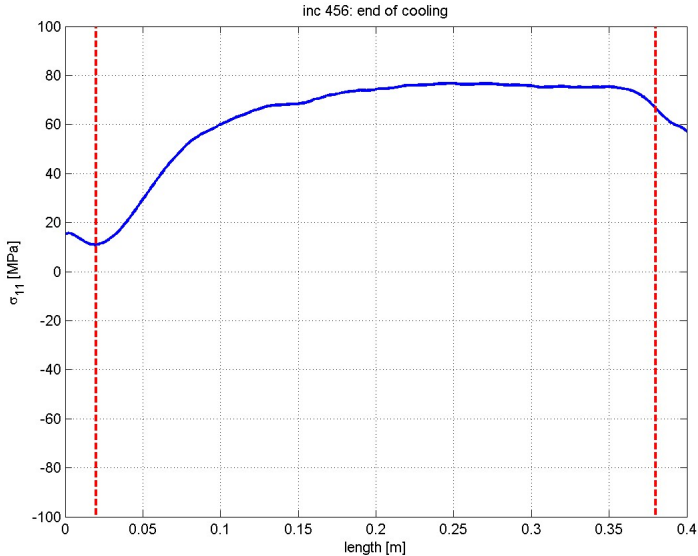
Figure 4.18: after cooling load case

inc 466: workpiece released
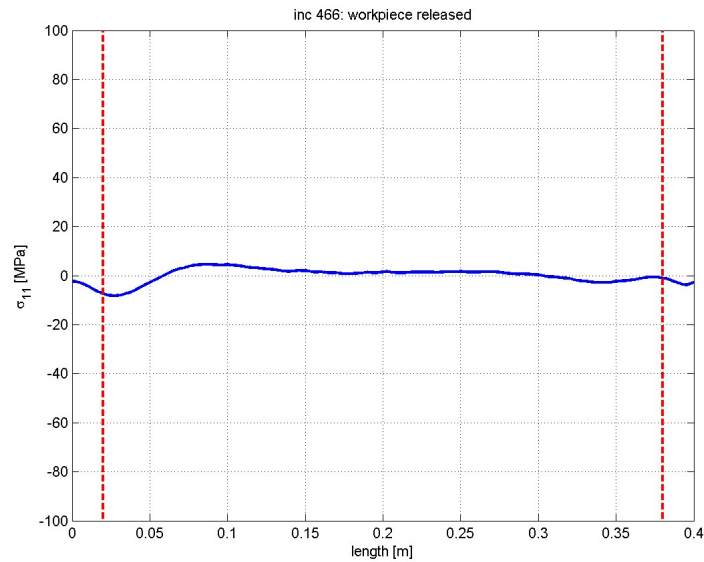
Figure 4.19: workpiece released

Fig. 4.20 shows the trend of transverse and longitudinal stresses across the weld line at the mid-length section. The longitudinal stresses obtained are perfectly in accordance with the theory. As explained in the introduction, residual stresses in friction stir welded workpieces, present an "M-like" trend. The maximum longitudinal stresses are between 20% and 50% of the materials yield stress. This condition is respected: the maximum residual stresses are about 180 MPa, which corresponds to about 50% of the yield stress of Al2024. The peaks in correspondance of the dashed black lines represent a numerical error, which results from the transition between different contact bodies' elements. A transition between filler elements and the contact bodies next to them, is expected be also visible. However, it has been checked that no fluctuation is present. This could

be attributed to the fact that the elements of both contacting bodies have the same mesh size and the same contacting condition with the other bodies (both have touch contacts with the Ti-plate and the shoulder). The biggest "jump" is at the transition between different sized elements (at -0.015 and 0.015m in fig. 4.20). The two highest (and equal valued) peaks are at the outer boarder of the shoulder. It should ne noted that the residual stresses in the workpiece are in balance for the longitudinal direction. This has been verified: the area underlying the positiv part of the curve is equal to the negative area. For the transverse stresses, instead, a quick look at the graph, makes it clear that it is not in balance. This is perfectly fine, since a balance of transverse stresses can only be obtained for a longitudinal cut of the workpiece (as can be seen in fig. 4.19).
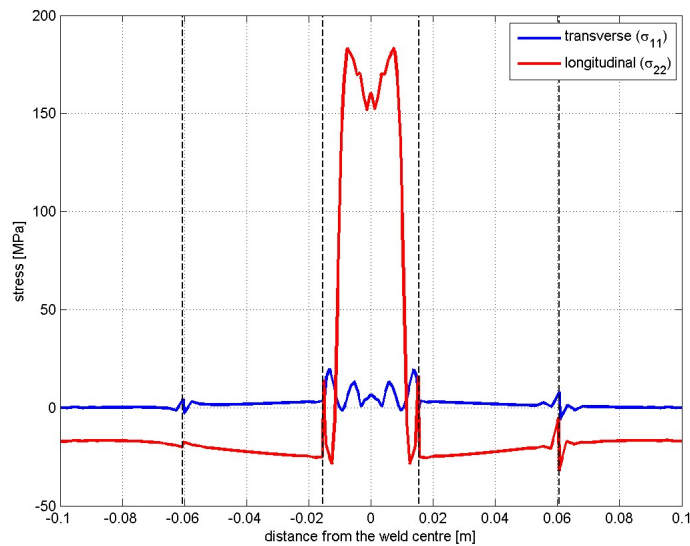
Figure 4.20: σ_{xx} and σ_{yy} over width at the mid-length section (y=0.2m) after the workpiece has been released

4.3 Distortions

In order to correlate the real deformation of the workpiece to the numerical results, the results of photogrammetry were needed. Unfortunately, due to the delay in receiving the report, no details on deformation were available. Therefore simple considerations, based on visual inspection of the workpieces, were made: the coupons in the as-welded condition, present two major deformation in both longituadinal and traverse direction with maximum displacements of a couple millimeters in the out-of-plane direction.

Once the thermal results were correlated, correlation of distortions was expected as well. Unfortunately, this did not occur and efforts were made to investigate its primary causes: for example it has been discovered that the contact definition of type glue between the different contact bodies, did not perfectly transmit the displacement between the nodes on the same location and therefore unreal stresses along these nodes were obtained. By simply inverting the contact body definition between workpiece and Ti-plate one transition has been eliminated. To do this, the Ti-plate has been split up into 3 contact bodies: two outer bodies underneath the distanciation pieces having their same length and a contact glue and one inner body with the touching condition (fig. 4.21). This led to a significant increase (about 1 order of magnitude) of the final deformation in terms of the out of plane displacement. Once this has been noticed, further effort has been made to develop a workpiece with the least contact bodies. In order to do this, only two types of meshes can be considered for the workpiece:

- a uniform mesh of cubic 1x1x1mm Hex8 elements

- a non uniform mesh, with a transition zone between the finer and the more coarse mesh

Due to the too many elements required for the first options, and the consequent increase of computational costs, the latter has been chosen (fig. 4.23).

For the inner zone, up to 15 mm from the weldline 1x1x1mm Hex8 elements were used, in accordance with the previous simulations. For the outer zone, from 100mm up to 25mm from the weldline, bigger Hex8 elements have been used (2.5x2x3). In between, Tet4 elements represent the transition between these two meshes , since no Hex8 elements could be used (fig. 4.22).

All this investigation required to change several contact body definitions (and the corresponding contact tables). Due to lack of time, the simulation with the model having the new contact bodies definition has not been run.
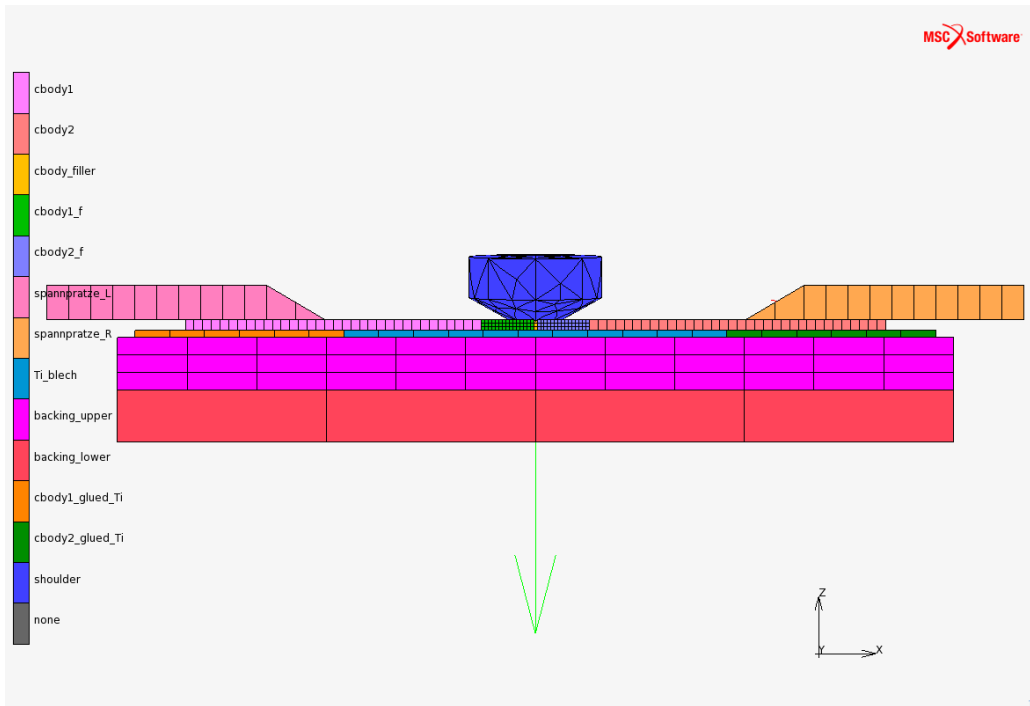
Figure 4.21: Model with one contact body less for each coupon's half
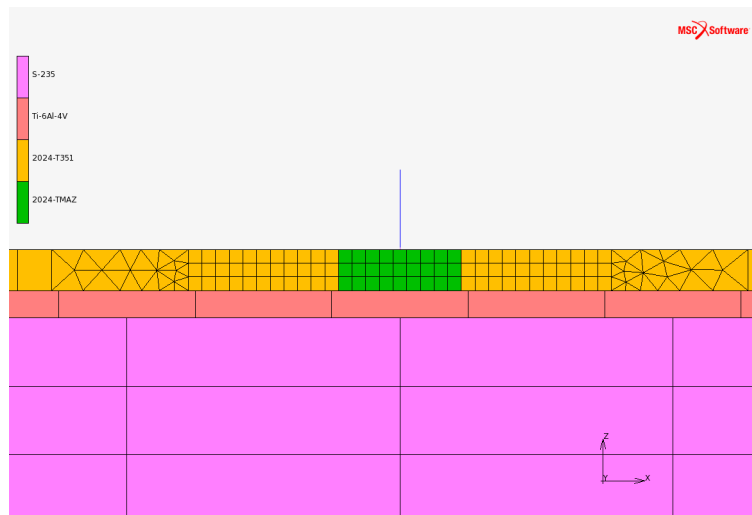
Figure 4.22: Detail of different materials around weld line and transition between different sized meshes in workpiece
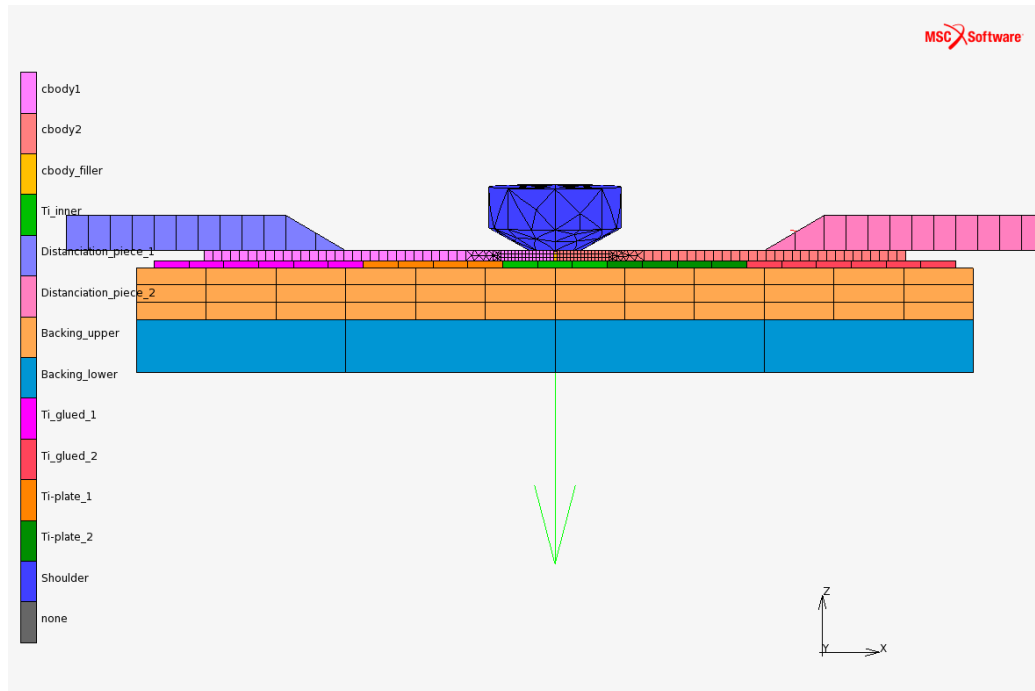
Figure 4.23: New contact bodies definition

Conclusions and Outlook:

During these six months, a good understanding of the *DeltaN* friction stir welding process, as well as the parameters involved, has been gained. The parameters and their influence on temperature distribution have been thoroughly investigated through the use of numerical simulation. The energies involved in the process have been identified and the most important ones also quantified. As seen, this led to a good correlation of the numerical temperature distribution with the experimentally acquired values. A correlation of distortions is desired, but unfortunately the available time was not enough to perform this investigation as well. Also, the reports on distortions, measured through photogrammetry during the first test campaign in September 2012, were not available by the end of the author's contract with RUAG (end of March 2013).

For the continuation of this research project, the author strongly recommends to use the developed model, with the settings presented in this work. A first major change for obtaining the correct distortions, is to insert the correct material properties for the different microstructural zones. The prepared model with only one contact body for each coupon's half could be used. This would probably lead to higher values of the out of plane deformation. This assertion is based on the experience made with the elimination of one contact body for each coupon's half.

A further improvement of the model, could be to create a dynamic material behaviour: the material properties for the different microstructural zones would be assigned based on the moving shoulder's position.

In order to correlate the results, it would be necessary to define one or more parameters for the quality of the simulation, e.g. the out of plane displacement (z-direction) for different nodes.

Once, this has been done, and with the understanding gained through this thesis, the simulation can be extended to more complicated workpieces, e.g. the joining line for section 19.1 of the A-320's airplane family, which should actually begin in the second half of 2014.

5 Appendix

5.1 Positioning of Thermocouples

5.1.1 Titanium backing plate
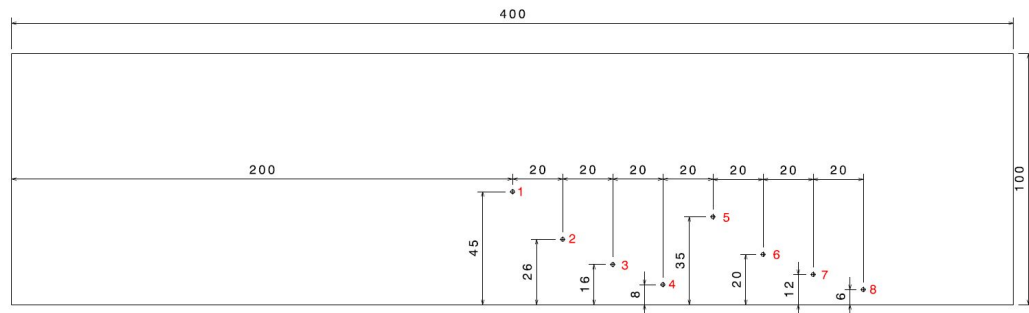
(a) One sided tests
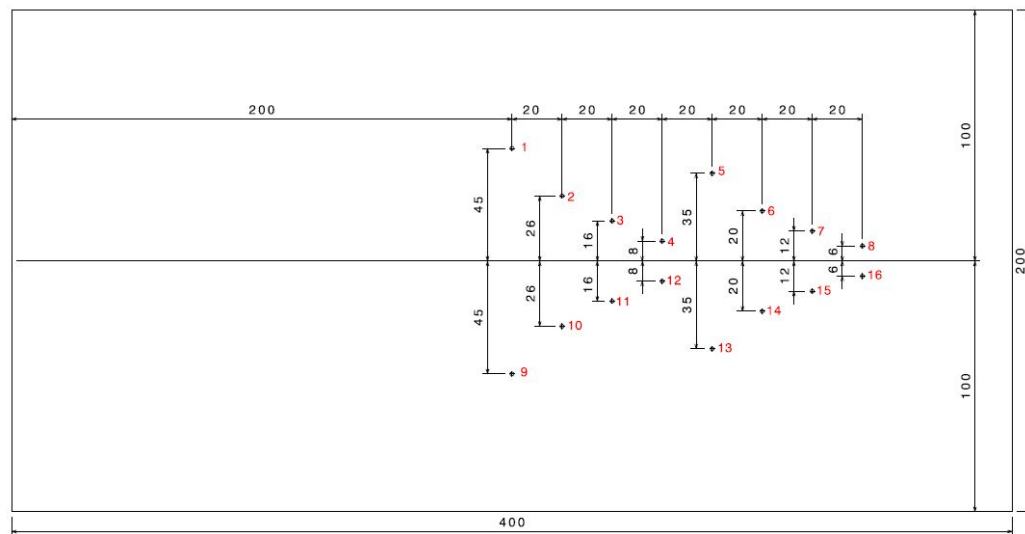
(b) Symmetrical tests

Figure 5.1: Thermocouple application positions for Ti-6Al-4V

5.1.2 Friction material backing
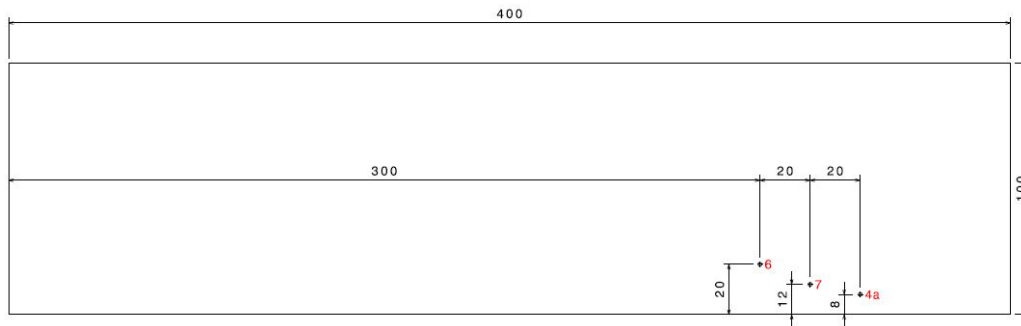
Figure 5.2: Thermocouple positions for F-3049

5.2 TESTS

All the tests were performed with the same tool. The specific parameters are reported in tab. 5.1.

Table 5.1: Parameters of tool

Tilt angle [°]	2
Shoulder's diameter [mm]	12
Probe's diameter [mm]	5
Probe's length [mm]	3.4
Probe protruding form shoulder [mm]	2.8

Table 5.2: Overview of tests performed in the 1st campaign: RP = reference probe to set up the weld path; SK = clamping force reduction; SA = variation of clamping distance from weld line ; VG = changing velocities, both rotational and traverse; SP = gap distance variation

Nr. [-]	Name [-]	Width [mm]	Length [mm]	Thick. [mm]	Force [kN]	Forw.Vel. [mm/min]	Rot.Vel. [U/min]	Gap [mm]	Tight.Torque [Nm]	Clamping dist. [mm]	Int. Plate [-]	T-Meas. [-]	Weld surf. [-]	Comment [-]
1	RP1	200	400	3	6	200	1200	0,2	30	25	Ti6Al4V	Yes	OK	Zug-/Biegeproben
2	RP2	200	400	3	6	200	1200	0,2	30	25	Ti6Al4V	No	OK	Zug-/Biegeproben
3	RP3	200	400	3	6	200	1200	0,2	30	25	Ti6Al4V	No	OK	none
4	RP4	200	400	2,5	6	200	1200	0,2	30	25	Steel	No	OK	none
5	RP5	200	400	2,5	6	200	1200	0,2	30	25	Steel	No	OK	none
6	RP6	200	400	2,5	6	200	1200	0,2	30	25	Steel	No	OK	none
7	RP7	200	400	2,5	N/A	N/A	N/A	N/A	N/A	N/A	N/A	N/A	N/A	none
8	RP8	200	400	2,5	6	200	1200	0,2	30	25	FRIMA	No	bad	none
9	RP9	200	400	2,5	N/A	N/A	N/A	N/A	N/A	N/A	N/A	N/A	N/A	none
10	SK1	200	400	3	6	200	1200	0,2	25	25	Ti6Al4V	No	OK	Traction Reference Test
11	SK2	200	400	3	6	200	1200	0,2	25	25	Ti6Al4V	No	OK	Traction & Bending Test
12	SK3	200	400	3	6	200	1200	0,2	25	25	Ti6Al4V	No	OK	Traction & Bending Test
13	SK4	200	400	3	6	200	1200	0,2	20	25	Ti6Al4V	No	OK	Traction & Bending Test
14	SK5	200	400	3	6	200	1200	0,2	20	25	Ti6Al4V	No	OK	Traction & Bending Test
15	SK6	200	400	3	6	200	1200	0,2	20	25	Ti6Al4V	No	OK	Zugreferenzprobe
16	SK7	200	400	3	6	200	1200	0,2	15	25	Ti6Al4V	No	OK	Zugreferenzprobe
17	SK8	200	400	3	6	200	1200	0,2	15	25	Ti6Al4V	No	OK	Traction & Bending Test
18	SK9	200	400	3	6	200	1200	0,2	15	25	Ti6Al4V	No	OK	Traction & Bending Test
19	SA1	200	400	3	6	200	1200	0,2	30	40	Ti6Al4V	Yes	OK	none
20	SA2	200	400	3	6	200	1200	0,2	30	40	Ti6Al4V	No	OK	Traction & Bending Test
21	SA3	200	400	3	6	200	1200	0,2	30	40	Ti6Al4V	No	OK	Traction & Bending Test
22	SA4	200	400	3	6	200	1200	0,2	30	60	Ti6Al4V	Yes	OK	none
23	SA5	200	400	3	6	200	1200	0,2	30	60	Ti6Al4V	No	OK	Traction & Bending Test
24	SA6	200	400	3	6	200	1200	0,2	30	60	Ti6Al4V	No	OK	Traction & Bending Test
25	SA7	200	400	3	6	200	1200	0,2	30	80	Ti6Al4V	Yes	OK	Traction & Bending Test
26	SA8	200	400	3	6	200	1200	0,2	30	80	Ti6Al4V	No	OK	Traction & Bending Test
27	SA9	200	400	3	6	200	1200	0,2	30	80	Ti6Al4V	No	OK	none
28	VG1	200	400	3	6	100	1000	0,2	30	25	Ti6Al4V	Yes	OK	none
29	VG2	200	400	3	6	100	1000	0,2	30	25	Ti6Al4V	No	OK	Traction & Bending Test
30	VG3	200	400	3	6	100	1000	0,2	30	25	Ti6Al4V	No	OK	Traction & Bending Test
31	VG4	200	400	3	6	150	1600	0,2	30	25	Ti6Al4V	Yes	OK	none
32	VG5	200	400	3	6	150	1600	0,2	30	25	Ti6Al4V	No	OK	Traction & Bending Test
33	VG6	200	400	3	6	150	1600	0,2	30	25	Ti6Al4V	No	OK	Traction & Bending Test
34	VG7	200	400	3	6	300	2200	0,2	30	25	Ti6Al4V	Yes	bad	Zug-/Biegeproben
35	VG8	200	400	3	6	300	2200	0,2	30	25	Ti6Al4V	No	bad	none
36	VG9	200	400	3	6	300	2200	0,2	30	25	Ti6Al4V	No	bad	Traction & Bending Test
37	SP1	200	400	3	6	200	1200	0,0	30	25	Ti6Al4V	Yes	OK	Traction & Bending Test
38	SP2	200	400	3	6	200	1200	0,0	30	25	Ti6Al4V	N/A	OK	none
39	SP3	200	400	3	6	200	1200	0,0	30	25	Ti6Al4V	N/A	OK	Traction & Bending Test
40	SP4	200	400	3	6	200	1200	0,3	30	25	Ti6Al4V	Yes	OK	Traction & Bending Test
41	SP5	200	400	3	6	200	1200	0,3	30	25	Ti6Al4V	No	OK	Zug-/Biegeproben
42	SP6	200	400	3	6	200	1200	0,3	30	25	Ti6Al4V	No	OK	none
43	SP7	200	400	3	6	200	1200	0,6	30	25	Ti6Al4V	Yes	bad	Traction & Bending Test
44	SP8	200	400	3	6	200	1200	0,6	30	25	Ti6Al4V	No	bad	Traction & Bending Test
45	SP9	200	400	3	6	200	1200	0,6	30	25	Ti6Al4V	No	bad	none
46	CGP1	400	500	2,5	N/A	N/A	N/A	N/A	N/A	N/A	N/A	N/A	N/A	Crack Propagation Test
47	CGP2	400	500	2,5	6	200	1200	0,2	30	25	Ti6Al4V	No	OK	Crack Propagation Test
48	CGP3	400	500	2,5	6	200	1200	0,2	30	25	Ti6Al4V	No	OK	Crack Propagation Test

Table 5.3: Overview of tests performed during the second test campaign

Nr.	Name	Width	Length	Thick.	Force	Forw.Vel.	Rot.Vel.	Gap	Tight.Torque	Clamping dist.	Int. Plate	T-Meas.	Weld surf.	Comment
[-]	[-]	[mm]	[mm]	[mm]	[kN]	[mm/min]	[U/min]	[mm]	[Nm]	[mm]	[-]	[-]	[-]	[-]
Ref.	Ref.	200	400	3,175	6	200	1200	0,2	30	25	Ti6Al4V			
1	TEST1	200	400	3,175	6	200	1200	0,2	30	25	Ti6Al4V	No	OK	Path set-up
2	TEST2	200	400	3,175	6	200	1200	0,2	30	25	Ti6Al4V	No	OK	
3	SK10	200	400	3,175	6	200	1200	0,2	10	25	Ti6Al4V	No	OK	Reduction of clamping forces until lateral forces are insufficient
4	SK11	200	400	3,175	6	200	1200	0,2	5	25	Ti6Al4V	No	OK	
5	SK12	200	400	3,175	6	200	1200	0,2	2,5	25	Ti6Al4V	No	bad	
6	PK1	200	400	3,175	5	200	1200	0,2	30	25	Ti6Al4V	No	OK	Reduction of process downward forces until insufficient
7	PK2	200	400	3,175	4	200	1200	0,2	30	25	Ti6Al4V	No	bad	
8	PK3	200	400	3,175	4	200	1200	0	30	25	Ti6Al4V	No	bad	
9	TM1	200	400	3,175	6	200	1200	0,2	30	60	Ti6Al4V	Yes	OK	Temperature measurements
10	TM2	200	400	3,175	6	200	1200	0,2	30	60	Ti6Al4V	Yes	OK	
11	TM3	200	400	3,175	6	200	1200	0,2	30	60	Ti6Al4V	Yes	OK	
12	TM4	200	400	3,175	6	200	1200	0,2	30	60	Ti6Al4V	Yes	OK	
13	TM5	200	400	3,175	6	200	1200	0,2	30	60	Ti6Al4V	Yes	OK	
14	TM6	200	400	3,175	6	200	1200	0,2	30	60	Ti6Al4V	Yes	OK	
15	RB1	200	400	3,175	6	200	800	0,2	30	25	FRIMA	No	OK	Definititon of process parameters (traverse and rotational speed) for FRIMA
16	RB2	200	400	3,175	6	200	600	0,2	30	25	FRIMA	No	bad	
17	RB3	200	400	3,175	6	200	700	0,2	30	25	FRIMA	No	OK	
18	RB4	200	400	3,175	6			0,2	30	25	FRIMA	No		
19	RB5	200	400	3,175	6			0,2	30	25	FRIMA	No		
20	RB6	200	400	3,175	6	200	700	0,2	5	25	FRIMA	Yes	bad	Reduction of clamping forces until lateral forces are insufficient (with FRIMA)
21	RB7	200	400	3,175	6	200	700	0,2	4	25	FRIMA	Yes	bad	
22	RB8	200	400	3,175	6	200	1200	0,2	30	25	FRIMA	Yes	OK	
23	RB9	200	400	3,175	6	200	1200	0,2	5	25	FRIMA	No	OK	
24	RB10	200	400	3,175	6	200	1200	0,2	7,5	25	FRIMA	No	OK	
25	TM7	200	400	3,175	6	200	1200	N/A	30	25	Ti6Al4V	Yes	OK	Temperature measurements in the weld seam
26	TM8	200	400	3,175	6	200	1200	N/A	30	25	Ti6Al4V	Yes		
27	TM9	200	400	3,175	6	200	1200	N/A	30	25	Ti6Al4V	Yes		

Table 5.4: Overview of tests performed during the second test campaign

Nr. [-]	Name [-]	Width [mm]	Length [mm]	Thick. [mm]	Force [kN]	Forw.Vel. [mm/min]	Rot.Vel. [U/min]	Gap [mm]	Tight.Torque [Nm]	Clamping dist. [mm]	Int. Plate [-]	T-Meas. [-]	Weld surf. [-]	Comment [-]	Measurements
Ref.	Ref.	200	400	3,175	6	200	1200	0,0	10	30	Ti6Al4V				
1	TEST1	200	400	3,175	6	200	1200	0,0	10	30	Ti6Al4V	No	OK	Path set-up. After tests, cooling through compressed air until reference temperature	none
2	TEST2	200	400	3,175	6	200	1200	0,0	10	30	Ti6Al4V	No	OK		Test: Forces + Temp
3	EB1	200	400	3,175	6	200	1200	0,0	10	30	Ti6Al4V	Yes	OK	Temperature measurement in the backing plate-->Energy estimation	only Temp
4	EB2	200	400	3,175	6	200	1200	0,0	10	30	Ti6Al4V	Yes	OK	Parallel measurement of forces and torque aborted due to interference	only Temp
	EB3	200	400	3,175	6	200	1200	0,0	10	30	Ti6Al4V	Yes	OK		only Temp
5	DM1	200	400	3,175	6	200	1200	0,0	10	30	Ti6Al4V	No	OK		only Forces
6	DM2	200	400	3,175	6	200	1200	0,0	10	30	Ti6Al4V	No	OK		only Forces
7	DM3	200	400	3,175	6	200	1200	0,0	10	30	Ti6Al4V	No	OK	Measurement of forces/ torque	only Forces
8	DM4	200	400	3,175	6	200	1200	0,0	10	30	Ti6Al4V	No	OK		only Forces
9	DM5	200	400	3,175	6	200	1200	0,0	10	30	Ti6Al4V	No	bad		only Forces
10	FS1	200	400	3,175	6	200	1200	0,0	10	30	Ti6Al4V	No	bad	Formfit fixation through clamps and end stops	none
11	SS1	200	400	3,175	6	200	1200	0,0	10	30	Ti6Al4V	No	OK	Adhesive bond through superglue	none

Traction and bending tests: In order to evaluate the quality of the welds, both traction and bending tests were performed. The evaluation of results, did not lead to a clear definition of the best parameters to use, since the data is very scattered[50]. All comparisons presented, are related to standard Al2024-T3, here referenced to as base material. In general, for the traction tests (fig. 5.3 and tab. 5.5), a significant reduction of yield strength in between 10.97% and 16.88%, compared to the base material, is observable. For the ultimate tensile strength, the data results much more scattered: reductions in ultimate tensile strength compared to the value for the base material go from 5.46% up to 24.08%.
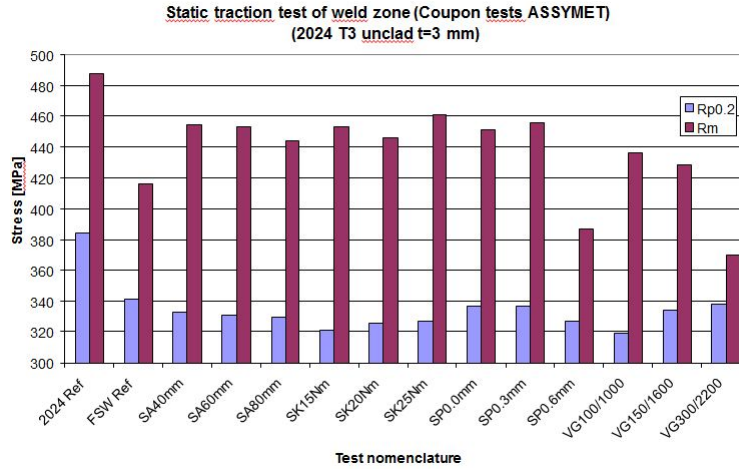
Figure 5.3: Results of tension test on weld seam

Table 5.5: Tensioning tests results

test	Rp 0.2	Rm	E	ΔRp 0.2	ΔRm	force	velocity	n	gap	tightening torque	clamping distance
	[MPa]	[MPa]	[MPa]	[%]	[%]	[kN]	[$\frac{mm}{min}$]	[rpm]	[mm]	[Nm]	[mm]
2024 Ref	383.88	487.53		0.00	0.00	N/A	N/A	N/A	N/A	N/A	N/A
FSW Ref	341.76	415.98		-10.97	-14.68	6	200	1200	0.2	30	25
SA40mm	333.14	454.78		-13.22	-6.72	6	200	1200	0.2	30	40
SA60mm	331.09	453.25		-13.75	-7.03	6	200	1200	0.2	30	60
SA80mm	329.28	443.52		-1422	-9.03	6	200	1200	0.2	30	80
SK15Nm	321.56	453.13		-16.23	-7.06	6	200	1200	0.2	15	25
SK20Nm	325.73	446.07		-15.15	-8.51	6	200	1200	0.2	20	25
SK25Nm	327.16	460.89		-14.78	-5.46	6	200	1200	0.2	25	25
SP0.0mm	337.09	451.37		-12.19	-7.42	6	200	1200	0.0	30	25
SP0.3mm	336.66	455.59		-12.30	-6.55	6	200	1200	0.3	30	25
SP0.6mm	326.82	386.39		-14.86	-20.75	6	200	1200	0.6	30	25
VG100/1000	319.08	436.1		-16.88	-10.55	6	100	1000	0.2	30	25
VG150/1600	333.94	428.25		-13.01	-12.16	6	150	1600	0.2	30	25
VG300/2200	337.75	370.12		-12.02	-24.08	6	300	2200	0.2	30	25

Bending tests were performed according to AITM1-0064 (Root Bending Test) Standard. The testing device is visible in fig. 5.4.

Figure 5.4: Bending test device

The results of the bending tests are reported in the following pages.

Test	Number	Force [kN]	Speed [mm/min]	n [rpm]	gap [mm]	torque [Nm]	distance [mm]	Breakage	Crack	without findings
RP1	01	6	200	1200	0,2	30	25	x		
	02	6	200	1200	0,2	30	25	x		
	03	6	200	1200	0,2	30	25	x		
RP2	01	6	200	1200	0,2	30	25	x		
	02	6	200	1200	0,2	30	25	x		
	03	6	200	1200	0,2	30	25	x		
SK2	01	6	200	1200	0,2	25	25			x
	02	6	200	1200	0,2	25	25		x	
	03	6	200	1200	0,2	25	25			x
SK3	01	6	200	1200	0,2	25	25		x	
	02	6	200	1200	0,2	25	25		x	
	03	6	200	1200	0,2	25	25	N/A	N/A	N/A
SK4	01	6	200	1200	0,2	20	25		x	
	02	6	200	1200	0,2	20	25		x	
	03	6	200	1200	0,2	20	25		x	
SK5	01	6	200	1200	0,2	20	25		x	
	02	6	200	1200	0,2	20	25	x		
	03	6	200	1200	0,2	20	25	x		
SK8	01	6	200	1200	0,2	15	25		x	
	02	6	200	1200	0,2	15	25			x
	03	6	200	1200	0,2	15	25	x		
SK9	01	6	200	1200	0,2	15	25			x
	02	6	200	1200	0,2	15	25		x	
	03	6	200	1200	0,2	15	25		x	
SA2	01	6	200	1200	0,2	30	40			x
	02	6	200	1200	0,2	30	40			x
	03	6	200	1200	0,2	30	40			x
SA3	01	6	200	1200	0,2	30	40			x
	02	6	200	1200	0,2	30	40			x
	03	6	200	1200	0,2	30	40			x
SA5	01	6	200	1200	0,2	30	60			x
	02	6	200	1200	0,2	30	60		x	
	03	6	200	1200	0,2	30	60			x
SA6	01	6	200	1200	0,2	30	60		x	
	02	6	200	1200	0,2	30	60	N/A	N/A	N/A
	03	6	200	1200	0,2	30	60	N/A	N/A	N/A
SA7	01	6	200	1200	0,2	30	80		x	
	02	6	200	1200	0,2	30	80	x		
	03	6	200	1200	0,2	30	80	x		
SA8	01	6	200	1200	0,2	30	80	x		
	02	6	200	1200	0,2	30	80	x		
	03	6	200	1200	0,2	30	80	x		
VG2	01	6	100	1000	0,2	30	25			x
	02	6	100	1000	0,2	30	25		x	
	03	6	100	1000	0,2	30	25		x	
VG3	01	6	100	1000	0,2	30	25	x		
	02	6	100	1000	0,2	30	25		x	
	03	6	100	1000	0,2	30	25	x		
VG5	01	6	150	1600	0,2	30	25			x
	02	6	150	1600	0,2	30	25			x
	03	6	150	1600	0,2	30	25	x		
VG6	01	6	150	1600	0,2	30	25			x
	02	6	150	1600	0,2	30	25	x		

	03	6	150	1600	0,2	30	25	x		
	01	6	300	2200	0,2	30	25	x		
VG7	02	6	300	2200	0,2	30	25		x	
	03	6	300	2200	0,2	30	25	x		
	01	6	300	2200	0,2	30	25			x
VG9	02	6	300	2200	0,2	30	25		x	
	03	6	300	2200	0,2	30	25		x	
	01	6	200	1200	0,0	30	25			x
SP1	02	6	200	1200	0,0	30	25	x		
	03	6	200	1200	0,0	30	25	x		
	01	6	200	1200	0,0	30	25		x	
SP3	02	6	200	1200	0,0	30	25	x		
	03	6	200	1200	0,0	30	25	x		
	01	6	200	1200	0,3	30	25		x	
SP4	02	6	200	1200	0,3	30	25		x	
	03	6	200	1200	0,3	30	25		x	
	01	6	200	1200	0,3	30	25		x	
SP5	02	6	200	1200	0,3	30	25		x	
	03	6	200	1200	0,3	30	25			x
	01	6	200	1200	0,6	30	25	x		
SP7	02	6	200	1200	0,6	30	25			x
	03	6	200	1200	0,6	30	25	x		
	01	6	200	1200	0,6	30	25	x		
SP8	02	6	200	1200	0,6	30	25			x
	03	6	200	1200	0,6	30	25			x

In general, the results do not present a clear trend. Only for the tests on the gap size and for the ones with different clamping distance, it can be said that with an increase of the varied paramter a reduction in weld quality has been noticed. This is proved by the breaking of the test samples.

For the other performed welds, no clear trend has been identified. For further information see [28].

References

[1] W. M. Thomas, E. D. Nicholas, J. C. Needham, M. G. Murch, P. Temple-Smith, and C. J. Dawes, Friction stir butt welding. International Patent Application PCT/GB92/02203, 1991.

[2] W. Tang, X. Guo, J. C. McClure, L. E. Numes, Heat input and temperature distribution in friction stir welding, J. Mater. Process. Manuf. Sci. 7:2 pp.163–172, 1998

[3] P. Colegrove, M. Painter, D. Graham, T. Miller, 3 dimensional flow and thermal modeling of the friction stir welding process, 2nd International Symposium on Friction Stir Welding, Gothenburg, Sweden, 2000

[4] H. Schmidt, Modelling the Thermomechanical Conditions in Friction Stir Welding, PhD Thesis, Technical University of Denmark, 2004

[5] M. J. Russel, H. R. Shercliff, Analytical Modeling of Microstructure Development in Friction Stir Welding, 1st International Symposium on Friction Stir Welding, Thousand Oaks, Cal , 1999

[6] P. Colegrove, M. Painter, D. Graham, and T.Miller, 3 Dimensional Flow and Thermal Modeling of the Friction Stir Welding Process, 2nd International Symposium on Friction Stir Welding Process, Gothenburg, Sweden, 2000

[7] The Welding Institute, Friction stir welding of aluminum alloys, International Materials Reviews, vol.54 no.2 March 2009, pp.49-93

[8] R. S. Mishra, Z. Y. Ma, Friction stir welding and processing, Materials Science and Engineering, 2005, pp. 1-78

[9] Elements of Metallurgy and Engineering alloys. Edited by F.C.Campbell ASM International 1st printing 2008

[10] H. J. Liu, H. Fujii, M. Maeda and K. Nogi: Mater. Sci. Technol., 2004, Vol. 20, pp. 103-105

[11] R.Talwar, D.Bolser, R.Lederich, J.Baumann, Friction Stir Welding of Airframe Structures, 2nd International Symposium on Friction Stir Welding, June 2000, Gothenburg Sweden, TWI

[12] J. Silvanus, COINS WP-6 Innovationen zum Rührreibschweißen, Presentation held at FSW Workshop Helmholtz-Zentrum Geesthacht, Germany, April 2009

[13] Cost effective Integral metallic Structure Report, June 2010, rev. January 2011 available at cordis.europe.eu

[14] Collection of presentations held at the 6th Friction Stir Welding-Workshop at Helmholtz-Zentrum Geesthacht, Germany, February 2013

[15] M. Pacchione, J. Telgkamp, Challenges of the Metallic Fuselage, 25th International Congress of the Aeronautical Sciences, Hamburg, Germany, 2006

[16] C. B. Fuller, Friction stir welding and processing, ASM International, Materials Park, OH, 2007, pp. 7-35

[17] L. Dubourg and P. Dacheux: Proc. 6th Int. Symp. on 'Friction stir welding', Saint-Sauveur, Mont., Canada, October 2006, TMS

[18] P. L. Threadgill and A. J. Leonard: 'Macro and microstructural features of friction stir welds in various materials', TWI members report no. 693/1999, TWI, Abington, UK, 1999.0.

[19] C. Dalle Donne, E. Lima, J. Wegener, A. Pyzalla, T. Buslaps, Investigations on Residual Stresses in Friction Stir Welds, 3rd International Symposium on Friction Stir Welding, Kobe, Japan, 2001

[20] M. James, M. Mahoney, Proceedings of the First International Symposium on Friction Stir Welding, Thousand Oaks, CA, USA, 1999.

[21] M. J. Russell, P. L. Threadgill, M. J. Thomas and B.P. Wynne, Static shoulder friction stir welding of Ti-6Al-4V; process and evaluation, 11th World Conference on titanium (Ti-2007), Kyoto, Japan, 2007

[22] C.A. Widener, J.E. Talia, B.M. Tweedy and D.A. Burford, High-rotational speed friction stir welding with a fixed shoulder, 6th International Symposium on Friction Stir Welding Saint-Sauveur, Canada, October 2006

[23] P.L. Threadgill, M.M.Z. Ahmed, J.P. Martin, J.G. Perrett and B.P.Wynne, The use of bobbin tool in FSW of aluminium alloys, Thermec 2009, Berlin, Germany, 25 - 29 August 2009

[24] C. Auracher, Innovatives Fertigungskonzept einer Rumpfstruktur unter Verwendung der Reibrührschweiß-Technologie, Diploma-Thesis, Hochschule München, Munich, Germany, 2012

[25] M. Scervini, Thermoelectric materials for thermocouples, Website of Cambridge University of Cambridge, Department of Materials Science and Metallurgy, consulted in November 2012

[26] T.G. Beckwith, N.L. Buck, R.D. Marangoni, Mechanical Measurements, Addison-Wesley Pub. Co, USA, 1982

[27] Omega Engineering, OMB-DAQ-2416 Multi-function I/O USB Data Acquisition Module User's Guide

[28] S. Kraus, Fertigungs- und Montagekonzept zur Verwendung des FSW Verfahrens am Beispiel einer dünnwandingen Schalenstruktur, Diploma-Thesis, Hochschule München, Munich, Germany, 2013

[29] Bosche, Transmitter WTB Manual

[30] MSC Marc Documentation, MSC Software, California, USA

[31] J. Goldak, A. Chakravarti and M. Bibby, A New Finite Element Model for Welding Heat Sources, Metallurgical Transactions B, June 1984, Vol. 15B, pp. 299-305

[32] L.S. Fletcher and D.A. Gyorog, Heat transfer between surfaces in contact: an analytical and experimental study of thermal contact resistance of metallic interfaces, NASA Research Report, USA, 1971

[33] http://www.matweb.com consulted in October 2012 - March 2013

[34] J.R. Davis, ASM Specialty Handbook: Aluminum and Aluminum Alloys, ASM International, 1993

[35] J.E. Hatch, Aluminum: properties and physical metallurgy, ASM International, 1984

[36] MIL-HDBK-5J, Department of Defense Handbook: Metallic Materials and Elements for Aerospace Vehicle Structures, USA, January 2003

[37] J.M. Pereira, Materials Database Development for Ballistic Impact Modeling, FAP Annual Meeting, October 2007, NASA Glenn Research Renter, USA

[38] J.D. Seidt, Characterization of 2024-T351 Aluminum for Dynamic Loading Applications, Proceedings of the 11th International Congress and Exposition, June 2008 , Florida USA

[39] J. dos Santos, Friction Stir Welding Modelling Thermal Characteristics, Helmholtz-Zentrum Geesthacht Internal Report commissioned by EADS, 2002

[40] J. Hodowany, G. Ravichandran, A. J. Rosakis and P. Rosakis, Partition of Plastic Work into Heat and Stored Energy in Metals, Experimental Mechanics, June 2000, Vol. 40, No. 2, pp. 113-123

[41] R. Kapoor, S. Nemat-Nasser, Determination of temperature rise during high strain rate deformation, Mechanics of Materials, 1998, Vol. 27, pp. 1-12

[42] G. Ravichandran, A.J. Rosakis, J. Hodowany and P. Rosakis, On the conversion of plastic work into heat during high-strain-rate deformation, Shock Compression of Condensed Matter, 2001, pp. 557-562

[43] D.Macdougall, Determination of the Plastic Work Converted to Heat Using Radiometry, Experimental Mechanics, September 2000, Vol. 40, No. 3, pp. 298-306

[44] Y.J. Chao, X.Qi and W. Tang, Heat Transfer in Friction Stir Welding - Experimental and Numerical Studies, Journal of Manufacturing Science and Engineering, February 2003, Vol. 125, pp. 138-145

[45] Conversation with J. dos Santos and J.Hilgert at Helmholtz-Zentrum Geesthacht during 6th FSW workshop, February 2013

[46] H.B. Schmidt and J.H. Hattel, Thermal modelling of friction stir welding, Scripta Materialia 2008, Vol.58, pp. 332–337

[47] C. P. Kothandaraman, Fundamentals Of Heat and Mass Transfer, New Age International, 2006

[48] R.A. Ristinen and J.J. Kraushaar, Energy and the Environment, 2nd ed. Hoboken, John Wiley&Sons, NJ, 2006

[49] MSC Software Support, October 2012-March 2013

[50] E. Yip, RUAG Internal Test Report, RUAG Aerospace Structures, Oberpfaffenhofen, Germany, February 2013